UNIVERSITA' DEGLI STUDI DI MILANO-BICOCCA

Scuola di Dottorato di Scienze
Corso di Dottorato di Ricerca in Fisica e Astronomia

THE XMM MEDIUM DEEP SURVEY: OPTICAL OBSCURATION VS X-RAY ABSORPTION IN ACTIVE GALACTIC NUCLEI

Supervisor: Dr. Ginevra TRINCHIERI
Director of PhD School: Prof. Claudio DESTRI

Tesi di Dottorato di:
Marzia TAJER
matricola R00299

Anno Accademico 2005-2006

Contents

I Introduction **1**

1 Introduction **3**
1.1 The Spectral Energy Distribution of AGN 3
1.1.1 Radio/submillimiter 5
1.1.2 Infrared 7
1.1.3 Optical/UV 8
1.1.4 X-rays 9
1.2 Obscured AGN and the AGN unification model 11
1.3 X-ray surveys and the X-ray background 17
1.4 Properties of the X-ray sources found in deep extragalactic surveys 21
1.5 Population synthesis models 24
1.6 Aims and structure of the Thesis 27

2 The XMM Medium Deep Survey **29**
2.1 Description of the XMM Medium Deep Survey 29
2.2 Associated multi-wavelength surveys 31
2.2.1 Optical data 31
2.2.2 Infrared data 32
2.2.3 Radio data 33
2.2.4 UV data 33
2.3 The XMM – LSS Database 34

3 The *XMM – Newton* satellite **37**
3.1 The EPIC Cameras 40
3.1.1 The *XMM – Newton* Point-Spread Function (PSF) . . . 41
3.1.2 The *XMM – Newton* filters 45
3.1.3 EPIC background 45
3.1.4 Event reconstruction 47

II Data reduction **51**

4 The X-ray analysis **53**
4.1 Preliminary data preparation and cleaning 53
4.2 Source detection and characterization 55
4.2.1 Data preparation 55
4.2.2 Source detection 55
4.2.3 Source characterization 56

5 The identification procedure **61**

III Results **69**

6 The logN-logS relationship **71**
6.1 Flux limit computation 72
6.2 The cumulative and differential logN-logS 73
6.3 Comparison with the literature 77

7 The 3 σ hard sample **81**
7.1 Sample composition 81
7.2 X-ray to optical ratio 83
7.3 Optical magnitude and colors 85
7.4 X-ray to infrared ratios 88

8 Photometric redshifts and Spectral Energy Distributions **93**
8.1 Template fitting and photometric redshift technique 93
8.2 Spectral Energy Distributions and classification 101

9 X-ray spectral properties **107**
9.1 Individual sources 107
9.2 X-ray absorption 113
9.3 Stacking analysis 119

10 Properties of the sample: optical obscuration vs X-ray absorption **123**
10.1 Optical obscuration and X-ray absorption 124
10.2 Comparison with the literature 127
10.3 Objects with discrepant absorption properties 129

11 Properties of the sample: surface density **133**
11.1 Optically obscured and unobscured AGN 133
11.2 Type 2 QSO candidates 135

12 Conclusions **139**

Bibliography **145**

A Properties of the 3 σ hard sample **159**

B Results of spectral fits **165**

Acknowledgments **171**

Part I

Introduction

Chapter 1

Introduction

Deep X-ray surveys have shown that active galactic nuclei (AGN) are the most important contributors to the X-ray background (XRB), and they are extremely effective in detecting AGN. While the observation of individual objects allows us to study the physics of AGN, extragalactic X-ray surveys offer the potential to contribute substantially to our understanding of the evolution of the AGN population. Obviously, the results coming from these two different approaches should be explained in a coherent scenario.

Here we present a description of the basic features and understanding of AGN and the AGN unification model. Then we review the history of the X-ray surveys, with a description of different kinds of sources found in deep and medium deep surveys, and the XRB population synthesis models. Finally, we present the aims and the structure of this Thesis.

1.1 The Spectral Energy Distribution of AGN

All sources shine over the whole electromagnetic spectrum, from the radio to the gamma rays. In almost all of this huge energy range, AGN are the brightest sources in the sky, except for the relatively narrow ($\sim$ 3 decades) range from the infrared (IR) to the ultraviolet (UV). As a result, obtaining a complete picture of an AGN is a challenging prospect requiring observations with a wide variety of telescopes. Over the past two decades, the multiwavelength view of quasars and AGN has expanded significantly thanks to the continuing increases in sensitivity (Sanders et al. 1989; Elvis et al. 1994; Haas et al. 1998; Polletta et al. 2000; Haas et al. 2003). The variety of the resulting Spectral Energy Distributions (SEDs) grows and, while the contributing emission and absorption mechanisms are well accepted, their relative importance, particularly as a function of AGN

class, remains a subject of debate.

Historically, the most common technique for AGN selection has been the UV - blue excess in the AGN continuum. For example, the best studied quasar sample, the Bright Quasar Survey sample, part of the Palomar - Green Survey (Schmidt & Green 1983), hereafter referred as "PG quasars", is defined through a magnitude limit ($B < 16.2, M_V < -23$) and a color limit ($U - B < -0.4$). Detailed studies of this sample revealed a remarkable homogeneity in their continua (Sanders et al. 1989; Elvis et al. 1994) and line properties from the IR to the X-rays (Laor et al. 1997), with the exception of a small fraction ($\sim 10\%$) of Broad Absorption Line (BAL) objects with quite different continua and line properties. Subsequent AGN samples have been obtained with deeper surveys but similar selection criteria. However, the blue selection method is in no way complete and can provide only a partial view of the general AGN SED. The color selection criterion cited above was chosen for efficiency (selecting objects that are AGN) and not for completeness (selecting all AGN, see Fig. 6.1 in Risaliti & Elvis 2004).

Observations at other wavelengths (e.g. radio, IR or X-rays) can efficiently find AGN, however surveys in different energy bands provide different views of the AGN population, always selecting the brightest sources in a particular waveband. It can be argued that some wavebands provide a less biased view than others (e.g. X-rays are less affected by absorption, far - IR is independent of orientation), however it is only by combining surveys in different wavelength regions that we can gain a view of the intrinsic population.

One property which, perhaps surprisingly, has not yet been shown to be related to the SED is evolution. With the central black hole as driver of the energy source, the black hole is expected to grow as material is accreted and so the observable properties of the AGN are expected to change as the source ages. Although observations of high redshift AGN are still limited, there is currently no convincing evidence for a change in SEDs with redshift (Silverman et al. 2002; Mathur et al. 2002; Brandt et al. 2002; Vignali et al. 2003a).

The standard reference for optically unobscured (i.e. type 1) AGN SEDs is the atlas of Elvis et al. (1994), who collected observations of bright quasars,[1]

[1]Historically, the term quasar has been used widely to refer to AGN of high luminosity whose emission completely overwhelmed that of the host galaxy (thus, these sources appeared as point sources in optical observations). Low luminosity AGN were (and still are) referred as Seyfert galaxies. However, evidence for any basic physical difference between these types of active objects has diminished through the years, essentially to the vanishing point. For this reason, in this Section, the term quasar is used as synonymous with type 1 AGN.

Band	Range (λ)	Range (ν)	Range (E)	F/F_{tot}
Radio	$3\text{m} - 0.1$ mm	$10^8 - 3 \times 10^{11}$ Hz	$4 \times 10^{-7} - 1.2 \times 10^{-3}$ eV	0%
Sub - mm	$1000 - 150\mu$m	$3 - 20 \times 10^{11}$ Hz	$1.2 - 8.3 \times 10^{-3}$ eV	0.2%
Far - IR	$150 - 40\mu$m	$2 - 7.5 \times 10^{12}$ Hz	$8.3 - 31 \times 10^{-3}$ eV	4.9%
Mid - IR	$40 - 10\mu$m	$7.5 - 30 \times 10^{12}$ Hz	$3.1 - 12 \times 10^{-2}$ eV	13.9%
Mid - IR	$10 - 3\mu$m	$3 - 10 \times 10^{13}$ Hz	$0.12 - 0.41$ eV	11.9%
Near - IR	$3 - 1\mu$m	$1 - 3 \times 10^{13}$ Hz	$0.41 - 1.25$ eV	7.0%
Optical	$1\mu\text{m} - 3000$ Å	$3 - 10 \times 10^{14}$ Hz	$1.25 - 4.16$ eV	12.2%
UV	$3000 - 1200$ Å	$1 - 2.5 \times 10^{15}$ Hz	$4.16 - 10.4$ eV	16.5%
EUV[a]	$1200 - 12.5$ Å	$2.5 - 240 \times 10^{15}$ Hz	10.4eV $-$ 1.0 keV	29.1%
X-ray	$12.5 - 0.125$ Å	$2.4 - 240 \times 10^{17}$ Hz	$1 - 100$ keV	4.2%

[a]: Based on high redshift quasars (Telfer et al. 2002).

Table 1.1: Average contribution of the different spectral bands to the bolometric emission of local unobscured AGN, from Risaliti & Elvis (2004).

from radio to hard X-ray wavelengths. The mean SED from this work is often cited as the "standard" quasar SED, and the main properties of this SED are in good agreement with the SEDs of optically selected AGN. However, even within this homogeneous sample, the 90% range of SEDs spans factors of ~ 10 or more at most frequencies.

Risaliti & Elvis (2004) present an updated version of the average SED of optically selected type 1 AGN, using results from the *Infrared Space Observatory* (*ISO*) in the IR (from Haas et al. 2003), the 2dF (from Croom et al. 2002) and the *Sloan Digital Sky Survey* (from Vanden Berk et al. 2001) in the optical, the *Hubble Space Telescope* in the optical/UV (from Telfer et al. 2002), and *ROSAT*, *BeppoSAX* and *ASCA* data (from Laor et al. 1997; Mineo et al. 2000; George et al. 2000) in the X-rays. For a recent review of AGN SEDs, see Risaliti & Elvis (2004) and Wilkes (2004).

In the following, the main spectral properties, from radio to X-ray bands, of local unobscured AGN will be described. Fig. 1.1 shows an example of SEDs for a radio loud and a radio quiet quasar from the Elvis et al. (1994) sample. The average contribution of the different spectral bands to the bolometric emission of local unobscured AGN is shown in Table 1.1.

1.1.1 Radio/submillimiter

The radio emission of quasars is significantly different for radio loud (RL) and radio quiet (RQ) sources. However, in all cases, the radio emission provides a negligible fraction of the bolometric luminosity (see Fig. 1.1 and Table 1.1).

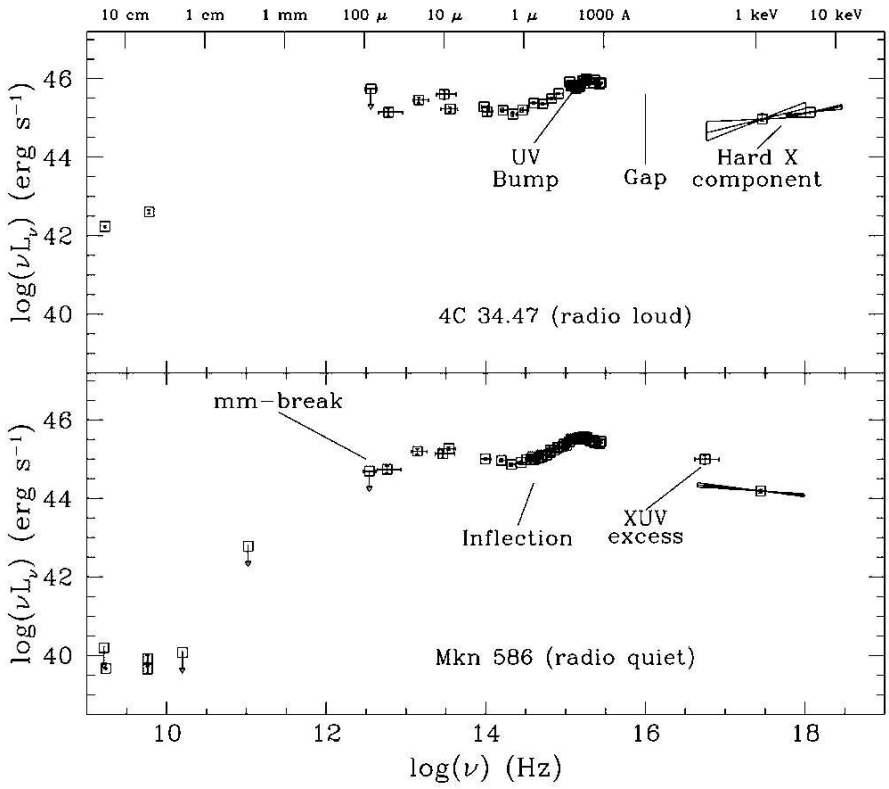

Figure 1.1: Radio to X-ray spectral energy distribution of a radio loud (upper) and a radio quiet (lower) quasar. Figure adapted from Elvis et al. (1994).

RL quasars fall into two distinct groups generally believed to be distinguished by the orientation of the source to our line of sight. Core dominated RL objects are those in which relativistically beamed, synchrotron emission is pointed directly along the line of sight. In these sources, the radio - IR SED tends to be smooth, suggesting that the IR is a higher energy extension of the synchrotron emission in the radio. Lobe dominated RL quasars are dominated by extended emission on either side of the central AGN, powered by the relativistic jets which, in these sources, are not close to the line of sight.

In RQ quasars the SED turns over sharply in the far IR, with a slope $\alpha > 2.5$ ($f_\nu \propto \nu^\alpha$) indicative of dust, and the radio emission is $\sim 100-1000$ times weaker than in RL objects.

1.1.2 Infrared

The basic characteristics of the IR emission of AGN as deduced from *IRAS* and *ISO* observations are the following:

- The integrated IR emission ($2 - 200\mu$m) is, on average, $\sim 30\%$ of the bolometric luminosity (see Table 1.1), with values in individual objects ranging from $\sim 15\%$ to $\sim 50\%$. The spectral shape is characterized by:

  1. A minimum at $\sim 1-2\mu$m, corresponding to the sublimation temperature of the most refractary dust (between 1000 and 2000 K, Sanders et al. 1989);
  2. an "IR bump", typically at $10-30\mu$m (but there are examples of flat spectra, or peaks anywhere between 2 and 100 μm), due to thermal emission of dust, with a temperature range between 50 and 1000 K;
  3. a steep decline ($f_\nu \propto \nu^\alpha, \alpha > 3$), at large wavelengths, typical of the low energy spectrum of gray emitter (Chini et al. 1989).

- The spectral shape of most of the sources is better reproduced, according to Haas et al. (2003), by reprocessing of the AGN primary emission, with the contribution of a starburst being negligible. However, this is still a controversial point, since the IR continuum expected from an AGN or a starburst is strongly dependent on the geometric and physical properties of the reprocessing medium, and the same observed continuum can often be successfully explained with more than one model (Elitzur et al. 2004).

- In RL AGN the spectrum between the IR bump and the sub - mm range is well reproduced by a power law with a spectral index close to $\alpha = 2.5$, as expected from self-synchrotron absorption. The main mechanism here is not reprocessing by dust, but synchrotron emission by relativistic electrons.

1.1.3 Optical/UV

The optical to UV emission of AGN is characterized by the "big blue bump" (Shields 1978; Malkan & Sargent 1982; Elvis 1985), where the peak of quasar luminosity is usually found. This component represents the emission of the optically thick regions of the accretion disk surrounding the black hole. The peak energy is around the Lyman edge ($\lambda = 1216$ Å) and the spectrum can be well approximated with a power law both at lower and higher frequencies. The relative strengths of the IR and big blue bump varies but they are generally comparable.

The main results of *HST* and SDSS studies are the following:

- The $300 - 5000$ Å continuum can be modeled with two power laws with slopes $\alpha_1 = -1.76$ between 300 Å and ~ 1200 Å and $\alpha_2 = -0.44$ between 1200 Å and 5000 Å. At longer wavelengths the spectrum appears to flatten significantly, but this effect is probably due to the contribution of galactic emission in the AGN spectra.

- No correlation between optical continuum properties and redshift or luminosity has been found.

- Strong emission lines are present in AGN spectra. The line width is thought to be associated with the virial velocity around the black hole, decreasing with increasing distance. Permitted emission lines are "broad" (corresponding to velocities of the emitting gas of $2000 - 15000$ km/s), while forbidden lines are "narrow" (a few hundred km/s). In addition to these lines, another major feature is the "small blue bump" (Wills et al. 1985; Elvis 1985) between ~ 2200 Å and ~ 4000 Å. This is not a true continuum feature but is due to a forest of emission lines from the ion Fe II and the Balmer recombination continuum.

- A minority ($\sim 10 - 20\%$) of AGN show broad absorption lines, often saturated, with widths and blueshifts of several thousands km/s and peaks of $20000 - 30000$ km/s.

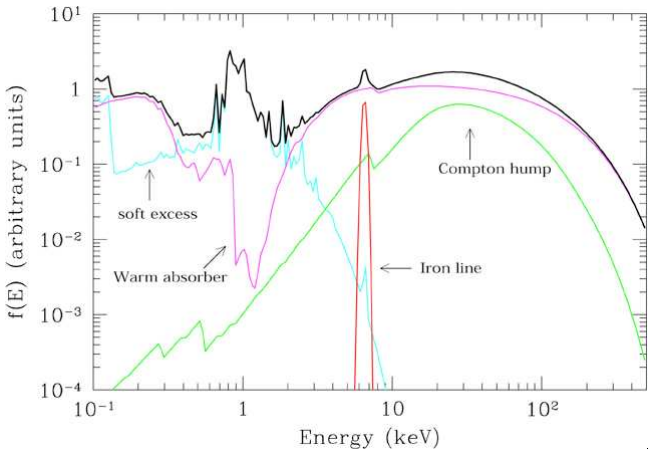

Figure 1.2: Average total spectrum (thick black line) and main components (thin colored lines) in the X-ray spectrum of an AGN. The main primary continuum component is a power law with an high energy cut-off at E $\sim 100 - 300$ keV, absorbed at soft energies by warm gas with $N_H \sim 10^{21} - 10^{23}$ cm^{-2}. A cold reflection component is also shown. The most relevant narrow feature is the iron Kα emission line at 6.4 keV. Finally, a "soft excess" is shown, due to thermal emission of a Compton thin plasma with temperature $kT \sim 0.1 - 1$ keV. Figure adapted from Risaliti & Elvis (2004).

- $\sim 50\%$ of bright Seyfert 1 galaxies observed in the UV show evidence of narrow absorption lines, with widths of $\sim$ 1000 km/s in the profiles of high ionization emission lines (OVI, CIV, Lyα). The presence of such features is strongly correlated with the presence of warm absorbers in the soft X-rays.

1.1.4 X-rays

In the X-ray band, an AGN is conventionally defined as having X-ray luminosity $L_X > 10^{42}$ erg s^{-1} and X-ray to optical ratio $X/O > 0.1$, while sources with lower luminosities and X-ray to optical ratios are starburst or normal galaxies. AGN with $10^{42} < L_X < 10^{44}$ erg s^{-1} are classified as Seyferts, while objects having $L_X > 10^{44}$ erg s^{-1} are called QSOs. However, extensive studies of nearby galactic nuclei established that many nearby galaxies harbor low luminosity AGN (LLAGN, see e.g. Ho et al. 1997a,b). In the X-ray regime, their luminosities are typically $\sim 10^{41}$ erg s^{-1}.

The X-ray emission from AGN extends from the galactic absorption cut-off at ~ 0.1 keV up to ~ 300 keV. The main features of the X-ray spectra of AGN are shown in Fig. 1.2.

The intrinsic continuum X-ray emission of AGN is to first order a power law,

extending from $\sim$ 1 keV to over 100 keV. However, as higher resolution and better signal to noise spectra have become available, emission and absorption features have been found that mask a direct view of this "power law" over virtually the whole X-ray band. The typical spectral index is between $\alpha = -0.8$ and -1,[2] both for low luminosity Seyfert galaxies and high luminosity quasars. It is still debated whether the spectral index is redshift or luminosity dependent (Zamorani et al. 1981; Avni & Tananbaum 1982, 1986; Bechtold et al. 2003; Vignali et al. 2003b).

There is increasing evidence, mostly from *BeppoSAX*, for a roughly exponential cut-off to the power law at energies $\sim 80 - 300$ keV. This is presumably due to the cut-off in the energy distribution of the electrons responsible for the X-ray emission.

In addition to the main power law continuum component, a soft emission component is often observed in AGN, with characteristic temperature $kT \sim 0.1 - 1$ keV. The physical origin of this component is not clear: warm emitting gas could be located in the accretion disk or in the broad line region or in a region farther from the center. Alternatively, this "soft excess" could be an extension of the big blue bump to higher energies (Czerny & Elvis 1987).

The primary emission of AGN can be "reflected", i.e. Thomson scattered by ionized gas. The main features of this reflection component are a continuum due to electron scattering with a peak at $\sim$ 30 keV, and a cut-off at $4-5$ keV due to photoelectric absorption of the lower energy incident radiation. The reflection efficiency is typically a few percent of the direct emission in the $2-10$ keV energy range because of photoelectric absorption, rising to $\sim 30\%$ at the 30 keV peak for a Compton thick reflector (i.e. having a column density $\mathrm{N}_H > 1.5 \times 10^{24}$ cm^{-2}) covering a significant fraction of the solid angle (Ghisellini et al. 1994). The efficiency drops if the reflecting medium is Compton thin (column density $\mathrm{N}_H < 1.5 \times 10^{24}$ cm^{-2}), in this case part of the incident radiation escapes without interactions. The reflected emission has the same spectral shape as the incident continuum.

The most prominent narrow feature in the $2 - 10$ keV X-ray spectra of AGN is an iron emission line at energy 6.4 keV, corresponding to the Fe-K $n = 2 - 1$ transition of "cold" (i.e. $\leq$ FeXVII) iron. The line is usually ascribed to emission due to fluorescence in the inner part of the accretion disk. The typical EW of the line is $100 - 200$ eV in X-ray unabsorbed and Compton thin

[2]X-ray astronomers tend to use however the "photon index" Γ, where $N(E) \propto E^{-\Gamma}$ and $\alpha = -(\Gamma - 1)$.

sources, while in Compton thick objects it is $\sim 1 - 3$ keV.

Many AGN exhibit important X-ray absorption features caused by the presence of highly ionized gas located on the line of sight of the central continuum; such a material is called warm absorber. The first observations of warm absorber gas in AGN were reported by Halpern (1984) in the *Einstein* spectrum of MR 2251−178, a quasar displaying a large absorption feature around 1 keV; this feature has been attributed to the O VII (739 eV) and O VIII (871 eV) photoelectric absorption edges (George et al. 1995) and is consistent with the presence of gas photoionized by the hard X-rays produced near the central engine of the AGN. Warm absorber features are present in the soft X-ray spectra of half of the bright Seyfert 1 galaxies observed with *ASCA*; evidence for a warm absorber was also found in Seyfert 2s, narrow line Seyfert 1s, BAL QSOs and even some BL Lacs. High resolution soft X-ray spectra, obtained with the grating instruments on board *Chandra* and *XMM - Newton*, have shown that the absorbing material is outflowing.

1.2 Obscured AGN and the AGN unification model

The picture described in the previous Section is far from exhaustive. It is becoming clear that in a significant fraction of AGN the nuclear emission is partially hidden by dust and gas. Locally, optically obscured AGN outnumber unobscured AGN by a factor of ~ 4 (Maiolino & Rieke 1995). Absorption introduces a spread in the emission properties of AGN, since the observed SEDs depend both on the intrinsic emission (which has a large dispersion) and on the amount, composition and geometry of the absorber. In general, the main absorption mechanisms in AGN are the following:

- line absorption due to atomic transitions;
- continuum absorption in the IR to UV due to dust;
- continuum absorption (or scattering) in the X-rays due to photoelectric absorption by dust and gas.

The physical state (temperature, density), column density and metallicity of the gas, the chemical composition of the dust, the dust to gas ratio, and the composition of the dust grains are all elements that affect the observed SED.

To explain the variety of features observed in AGN, it was suggested that all AGN have the same intrinsic properties and that the different SEDs and

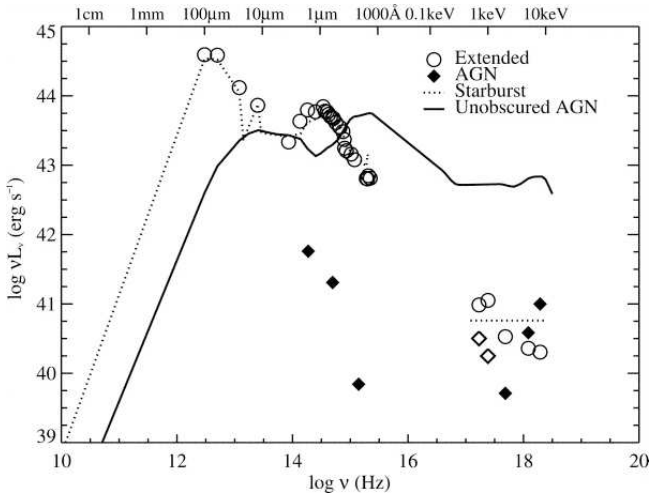

Figure 1.3: Spectral energy distribution of NGC 5135, showing large-scale emission (circles) and the spatially isolated AGN contributions (filled diamonds). In general, the galaxy appears very similar to dusty starburst galaxies (dotted line). For comparison, the average radio-quiet quasar spectrum (Elvis et al. 1994) scaled to the intrinsic bolometric luminosity of NGC 5135 is shown (solid line). Figure adapted from Levenson et al. (2004).

spectra observed are the result of different orientations of AGN with respect to the observer. In the unified AGN model, first proposed by Antonucci (1993), all AGN are postulated to harbor a central, accreting massive black hole surrounded by a system of clouds of gas, photoionized by the central source, called Broad Line Region (BLR). Further out a system of gas and dust clouds, the Narrow Line Region (NLR), emits highly excited narrow lines that are ionized by the central source. The AGN is also proposed to be surrounded by dusty obscuring material, optically and geometrically thick, often modeled as a (clumpy) torus, that anisotropically absorbs or shadows emission from the nuclear region. Type 1 AGN in this scheme are AGN where the line of sight to the nucleus does not intercept the torus and both broad and narrow emission lines are observed in their optical spectra. In type 2 systems the line of sight is blocked by the obscuring torus, and only the NLR is directly visible. The broad emission lines are therefore absent in objects classified as pure type 2 AGN. Less obscured AGN are classified as type 1.9 and type 1.8 and show broad components in, respectively, the Hα line and both the Hα and Hβ lines.

The optical/UV continuum in type 2 AGNs is heavily absorbed by dust and thermally reradiated at longer wavelengths. The observed continuum is dominated by the stellar contribution of the host galaxy and/or scattered emission.

This latter component can be disentangled through observations in polarized light. Galaxy light peaks in the wavelength region between the IR and the optical/UV bumps in AGNs, so the strength of this inflection depends on the relative luminosity of the AGN and its host. Thus the near IR is the best region in which to study the host galaxy (McLeod & Rieke 1995). As an example, we show in Fig. 1.3 the SED of NGC 5135, an highly obscured AGN where the nuclear contribution only emerges in the hard X-rays, while in the optical-IR and in the soft X-rays the emission is dominated by a strong starburst component from the host galaxy.

The torus postulated in the unified model is a useful working hypothesis, however the "true" distribution of dust around the nucleus is different in different objects and is still matter of debate. The variety of SEDs observed in AGN can be used to model the dust distribution, as shown in Fig. 1.4 (see also Haas et al. 2003).

The torus is assumed to contain both dust, which absorbs the optical light, and gas, which absorbs the X-ray emission, at least in the soft ($0.5 - 2$ keV) band, while the hard X-ray emission ($2 - 10$ keV) can pierce through the torus. In this scenario, X-ray absorption should be observed in type 2 AGN.[3] For a galactic dust composition (from Schultz & Wiemer 1975) and dust to gas ratio (Bohlin et al. 1978; Kent et al. 1991), the relation between optical extinction and X-ray absorption is

$$\mathrm{A_V} \sim 5.3 \times 10^{-22} \mathrm{N}_H. \tag{1.1}$$

Therefore, one would expect objects where optical broad lines are visible to have X-ray column densities not higher than 10^{22} cm^{-2} (Risaliti & Elvis 2004). This is indeed what was found in many local AGN.

Obscuration in the X-rays is due to the photoelectric absorption (dominant below ~ 3 keV) and Compton scattering (dominant from ~ 7 to ~ 30 keV). The observed X-ray spectral properties of X-ray absorbed AGN depend on the amount of obscuring column density: column densities below 1.5×10^{24} cm^{-2} produce a photoelectric cut-off at energies between 1 and 10 keV (in this case, the source is "Compton thin"); column densities between $\sim 10^{24}$ and $\sim 10^{25}$ cm^{-2} ("Compton thick" sources) absorb the X-ray primary emission up to several tens of keV; even higher column densities completely obscure the

[3]Conventionally, a source is defined X-ray absorbed if its intrinsic column density N_H is $> 10^{22}$ cm^{-2}, and unabsorbed if $\mathrm{N}_H < 10^{22}$ cm^{-2}.

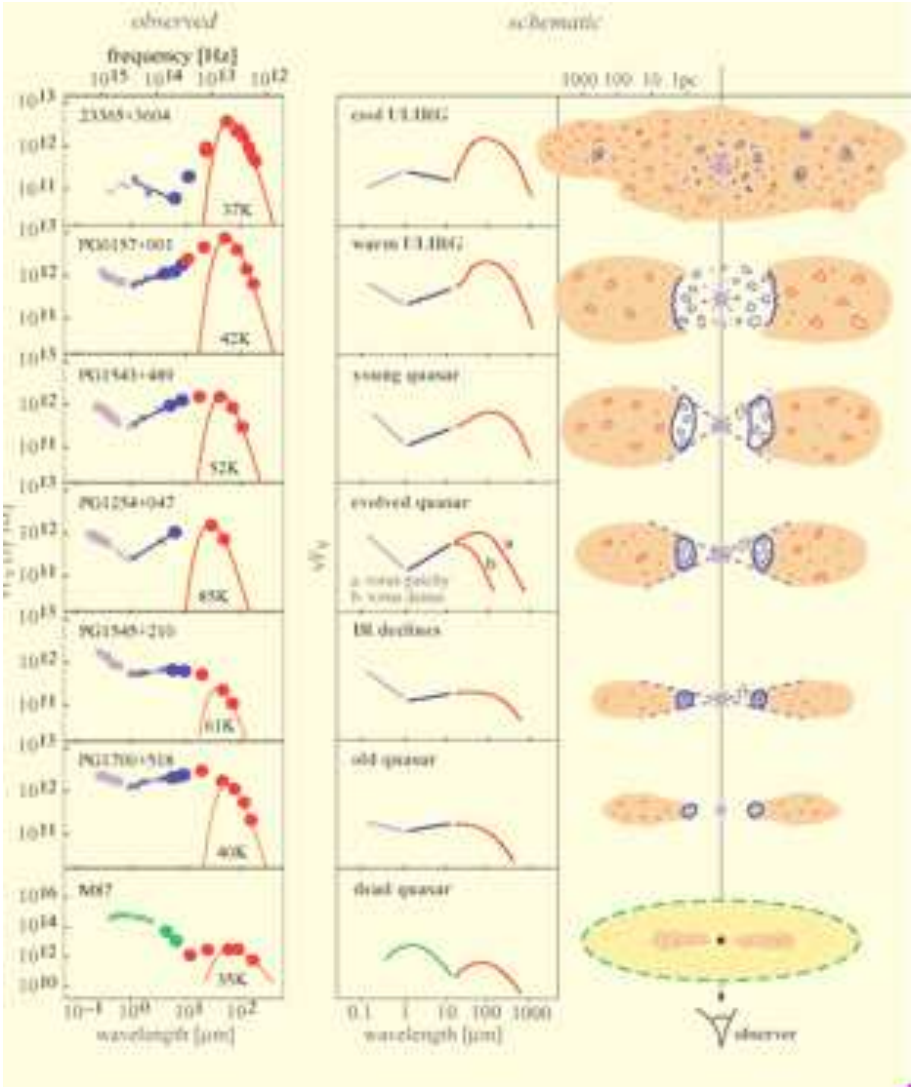

Figure 1.4: Observed AGN SEDs and scheme of dust distribution surrounding the AGN. Figure adapted from Haas (2004).

central source in the X-rays. The $2-100$ keV spectra of four representative X-ray absorbed AGN are shown in Fig. 1.5.

Some inconsistencies with the AGN model have however emerged. There are a number of objects that show opposite X-ray and optical properties, such as X-ray absorbed type 1 AGN (e.g. Maiolino et al. 2001; Comastri et al. 2001; Brusa et al. 2003; Akiyama et al. 2003) or X-ray unabsorbed type 2 AGN (e.g. Panessa & Bassani 2002; Wolter et al. 2005). For absorbed type 1 AGN a possible explanation is that the dust/gas ratio of the absorber is much lower than in the galactic interstellar medium, probably due to dust sublimation. Another possibility is that the optical and X-ray absorbers cover different regions: the nucleus for the X-ray absorber, a larger region for the optical one (see Matt 2002, and references therein).

Concerning X-ray unabsorbed type 2 AGN, Panessa & Bassani (2002) find that in a sample of optically selected Seyfert 2, a fraction of the order of $10-20\%$ have column density $< 10^{22}$ cm^{-2}. They propose the following explanations: either the BLRs are covered by a dusty obscuring material (dust patches, dust lanes, HII regions) or the BLRs are absent, weak or faded away. This interpretation seems to hold for low luminosity nuclei ($L_X \sim 10^{41} - 10^{42}$ erg s^{-1}). In the QSO regime ($L_X > 10^{44}$ erg s^{-1}), Wolter et al. (2005) find three optically classified type 2 objects, with high X-ray luminosity, that do not show any sign of obscuration in their X-ray spectra. A possible explanation is that the gas is completely ionized, and therefore transparent to the X-ray radiation, while the dust in the torus absorbs the optical BLR.

There are also X-ray loud sources (luminosities of $\sim 10^{41} - 10^{43}$ erg s^{-1}), with X-ray to optical ratios suggesting some type of moderate strength nuclear activity, that do not appear as AGN in the optical, where AGN emission lines and non - stellar continua are not apparent. Their redshifts are in the range $\sim 0.05 - 1$. Some also have hard X-ray spectral shapes suggesting the presence of X-ray absorption (e.g. Severgnini et al. 2003). Such population of X-ray bright, optically normal galaxies (XBONGs, Comastri et al. 2002) has emerged at fluxes of $\sim 10^{-14}$ erg cm^{-2} s^{-1}. Their nature remains somewhat mysterious. Many may just be Seyfert 2 galaxies where dilution by the host galaxy light hinders optical detection of the AGN (e.g. Moran et al. 2002; Severgnini et al. 2003), but some have high quality follow - up observations and appear to be truly remarkable objects (e.g. Comastri et al. 2002). These "true" XBONGs may be AGN with inner radiatively inefficient accretion flows (Yuan & Narayan 2004), or AGN that suffer from heavy obscuration covering a large solid angle

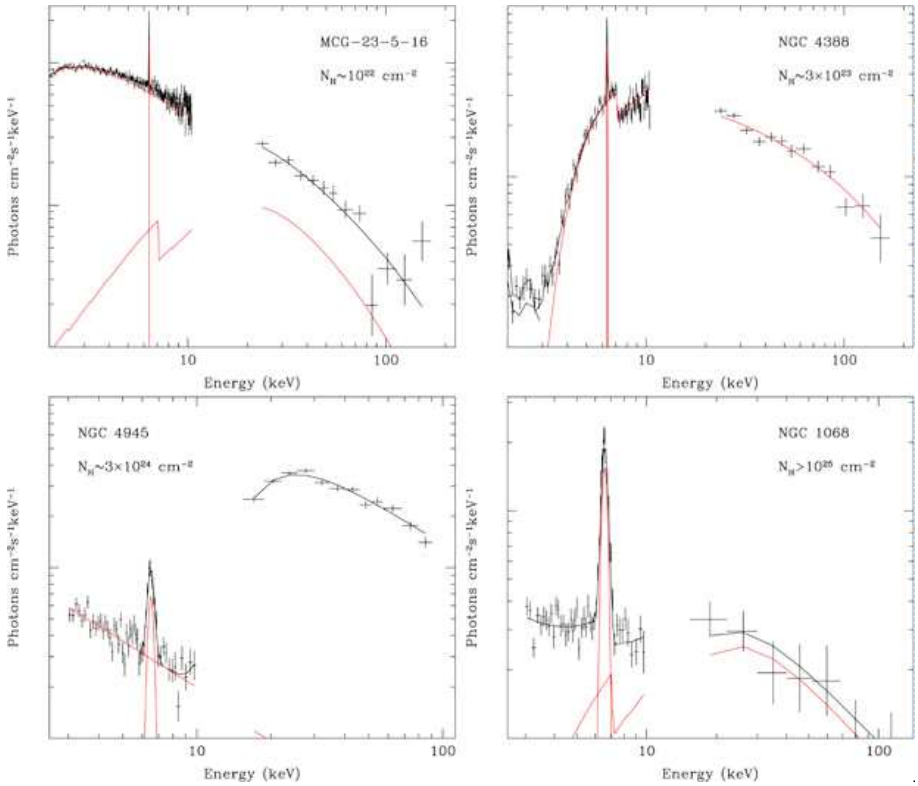

Figure 1.5: Four $2-100$ keV *BeppoSAX* best fit X-ray spectra of Seyfert 2 galaxies. Main components of the best fit models are also shown in red. MCG-5-23-16 and NGC 4388 (Risaliti 2002) are "Compton thin", i.e., they are dominated by the primary emission down to a few keV. In MCG-5-23-16, a cold reflection component also gives a measurable contribution. The continuum in the Compton-thick source NGC 4945 (Guainazzi et al. 2000) is due to a warm reflection component in the $2-10$ keV range, while at higher energies the intrinsic component emerges. Note the high ratio between the $10-100$ keV and the $2-10$ keV emission, as compared with the Compton-thin sources. NGC 1068, also Compton-thick (Matt et al. 1997), shows a cold reflection and a warm reflection component. Figure adapted from Risaliti & Elvis (2004).

($\sim 4\pi$), so that optical emission - line and ionizing photons cannot escape the nuclear region (Matt 2002).

1.3 X-ray surveys and the X-ray background

The Cosmic X-ray Background (XRB) was the first cosmic background discovered. The data collected during a rocket flight, originally designed to detect X-ray emission from the Moon, showed a strong galactic X-ray source (Sco X-1) and a diffuse emission of approximately constant intensity from all directions (Giacconi et al. 1962). The first X-ray surveys in the 1970's with *Uhuru* and *Ariel V* revealed a high degree of isotropy, leading researchers to conclude that the XRB must be mainly extragalactic, at least at energies greater than 2 keV.

The first wide band measure of the XRB, performed by *HEAO1*, demonstrated that, in the $3-50$ keV band, the shape of the XRB spectrum could be well fitted by a thermal bremsstrahlung model emitting at $kT \sim 40$ keV (Marshall et al. 1980; Rothschild et al. 1983). This lead to the idea that the universe might be permeated by a hot intergalactic medium. On the other hand, the discovery of many classes of extragalactic X-ray emitters (e.g. Seyfert galaxies and quasars, BL Lac objects, normal galaxies, clusters of galaxies...) suggested the possibility that the summed contributions of unresolved discrete sources may give rise to the XRB. Since galaxy clusters are mostly thermal emitters with typical temperatures of $5-10$ keV, they cannot contribute significantly to the peak of the XRB around 30 keV. Therefore, the only discrete sources which can give a substantial contribution to the XRB emission are AGN, whose X-ray radiation is due to the conversion of gravitational energy of gaseous matter accreting onto a supermassive black hole (Rees 1984). Already in 1979, deep *Einstein* observations have resolved $\sim 25\%$ on the $1-3$ keV XRB at fluxes down to $\sim 3 \times 10^{-14}$ erg cm^{-2} s^{-1} into discrete sources, a large fraction of which were identified as AGN (Giacconi et al. 1979). The diffuse emission hypothesis for the origin of the XRB was definitively ruled out by the results obtained with instruments aboard *COBE* on the spectrum of the cosmic microwave background (Mather et al. 1990, 1994). In fact, the presence of a hot gas should give rise to distorsions in the spectrum of the cosmic microwave background through inverse Compton scatering. Such distorsions were not observed by *COBE* and the contribution of hot gas ($T \gtrsim 10^8$ K) to the XRB was quantified in less than 0.01% (Wright et al. 1994).

Deep surveys with *ROSAT* to limiting fluxes of $\sim 10^{-15}$ erg cm^{-2} s^{-1} in the

$0.5 - 2$ keV band were for the first time able to resolve the majority ($\sim 75\%$) of the soft XRB into discrete sources (e.g. Hasinger et al. 1993, 1998), and extensive optical follow up spectroscopy identified the bulk of these sources as AGN (e.g. McHardy et al. 1998; Schmidt et al. 1998; Zamorani et al. 1999; Lehmann et al. 2001). The AGN sky density detected by *ROSAT* ($\sim 780 - 870$ deg^{-2}) was larger than those found at any other wavelength.

The sources observed by *Einstein* and *ROSAT* have been found to be mostly bright broad line AGN (type 1 Seyferts and QSOs) at an average redshift of ~ 1.5, with a small fraction of more local type 2 Seyferts (Bower et al. 1996; Schmidt et al. 1998; Zamorani et al. 1999). The mean slope of the spectra of bright AGN is $\Gamma \sim 1.7 - 1.9$ (Turner & Pounds 1989; Nandra & Pounds 1994; Nandra et al. 1997) and is clearly different from that of the XRB spectrum ($\Gamma \sim 1.4$, Gendreau et al. 1995; Chen et al. 1997; Vecchi et al. 1999), giving rise to a problem for the discrete source origin of the XRB, the so - called "spectral paradox". Setti & Woltjer (1989) proposed a solution to this paradox extending to the X-ray band the unified model of AGN (Antonucci & Miller 1985; Antonucci 1993). They explained the XRB as an appropriate mixture of absorbed and unabsorbed AGN, supposing that the same obscuring torus which hides the broad line region in Seyfert 2 galaxies is optically thick also at X-ray wavelengths (see Section 1.2). Thus, varying the viewing angle means to vary the column density of the absorbing matter and consequently the fraction of primary radiation visible to the observer. Following their suggestions, the contribution of different classes of sources to the hard XRB has been evaluated through population - synthesis models (e.g. Madau et al. 1994; Comastri et al. 1995; Gilli et al. 2001). Confirmation of the model predictions required however observations at higher energies, less biased against absorbed AGN.

Deep surveys above $2 - 3$ keV had to wait considerably longer than those at lower energies owing to technological challenges. Some medium - to - deep sky surveys performed by *ASCA* (Georgantopoulos et al. 1997; Ueda et al. 1998; Cagnoni et al. 1998; Ishisaki et al. 2001) and the analysis of the spatial fluctuations in deep *ASCA* observations probed the $2 - 10$ keV source counts down to a flux limit of 2×10^{-14} erg cm^{-2} s^{-1}, resolving $\sim 35\%$ of the XRB into discrete sources (Gendreau et al. 1998). The first surveys in the $5 - 10$ keV band were achieved using *Beppo - SAX*, whose observations resolved $20 - 30\%$ of the $5 - 10$ keV XRB (Comastri et al. 2001).

According to the population - synthesis models, most of the AGN spectra are heavily absorbed, and about 85% of the radiation produced by supermassive

black hole accretion is obscured by dust and gas (e.g. Fabian & Iwasawa 1999). A number of heavily obscured AGN were found in the *ASCA* and *Beppo - SAX* surveys. On the other hand high luminosity, obscured X-ray sources such as type 2 quasars, that should give a substantial contribution to the XRB according to the models, at that time had only scarcely been detected.

X-ray surveys have dramatically advanced over the past six years, due to the superb capabilities of *Chandra* and *XMM – Newton* in terms of imaging, positional accuracy and spectral resolution. Deep X-ray surveys such as the 2 Ms *Chandra* Deep Field North (Alexander et al. 2003), the 1 Ms *Chandra* Deep Field South (Giacconi et al. 2002) and the *XMM – Newton* Lockman Hole (Hasinger 2004), reaching a depth of $\sim 2 \times 10^{-17}$ erg cm^{-2} s^{-1} in the $0.5-2$ keV band, $\sim 2 \times 10^{-16}$ erg cm^{-2} s^{-1} in the $2-8$ keV band and $\sim 1.2 \times 10^{-15}$ erg cm^{-2} s^{-1} in the $5-10$ keV band, have now resolved more than 90% of the XRB in the $0.5-2$ keV band, $80-90\%$ in the $2-8$ keV band and $50-70\%$ between 6 and 10 keV. At the flux levels reached in the *Chandra* Deep Fields (CDFs) moderate luminosity AGN (similar to Seyfert galaxies in the local universe) could be detected to redshift $z \geq 10$. There are other deep surveys, generally performed in regions of sky where extensive coverage already exists at one or several wavelengths and/or some interesting object is present; see Brandt & Hasinger (2005) and Brandt et al. (2004) for a review.

In addition to deep surveys, many shallower, wider X-ray surveys are in progress. They typically involve investigation of X-ray sources in several X-ray observations of moderate exposure (usually $20-60$ ks, but sometimes as short as 5 ks). They bridge the observational gap between the deepest *Chandra* observations and the observations made by previous X-ray missions. They effectively target the intermediate $0.5-8$ keV flux range ($10^{-15}-10^{-13}$ erg cm^{-2} s^{-1}), which contribute most significantly to the XRB. They also provide a broad census of the X-ray source population, allowing the discovery of both intrinsically rare source types as well as low redshift examples of sources found in the deep X-ray surveys. The flux limit and the solid angle covered by some deep and medium deep surveys performed by *Chandra* and *XMM - Newton*, together with earlier missions by *ROSAT* and *Einstein*, are shown in Fig. 1.6.

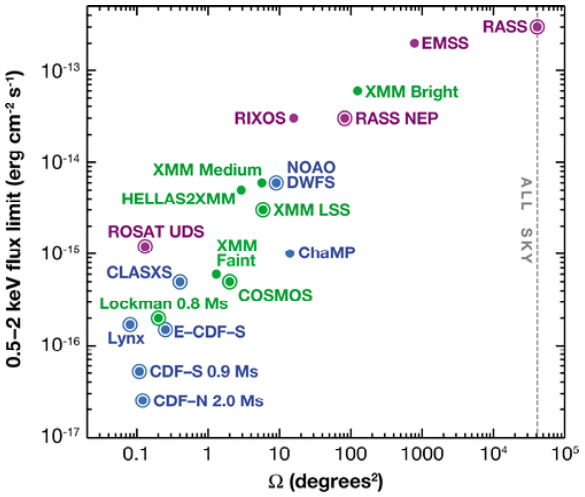

Figure 1.6: Limit flux ($0.5 - 2$ keV band) vs solid angle for some well-known extragalactic surveys by *Chandra* (blue), *XMM – Newton* (red) and early missions (magenta). Circled dots denote contiguous surveys. Each of the surveys shown has a range of flux limits across its solid angle; the most sensitive flux limit is generally shown. For comparison, the XMDS survey described in this Thesis (see next Chapters) covers an area of ~ 3.4 deg^2 and is complete down to $\sim 8 \times 10^{-15}$ erg cm^{-2} s^{-1} in the $0.5 - 2$ keV band, while the minimum flux detected in this band is $\sim 10^{15}$ erg cm^{-2} s^{-1} (see Chapter 6). The vertical dotted line shows the solid angle of the whole sky. Figure adapted from Brandt & Hasinger (2005).

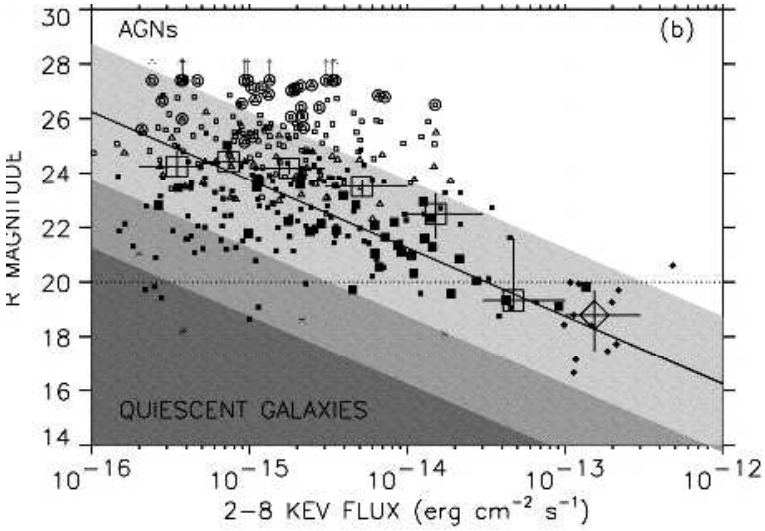

Figure 1.7: R magnitude vs. $2-8$ keV flux for the CDF-N hard X-ray sources and the Akiyama et al. (2000) ASCA data. Large open squares (large open diamond) with uncertainties show the median values of the optical magnitudes for the CDF-N (Akiyama et al. 2000) X-ray sources. The solid line is $\log(F_X/F_R) = 0$. Shaded regions indicate typical values of X-ray-to-optical flux ratios for different source classes: AGN typically lie in the lightest shaded region ($\log(F_X/F_R) = \pm 1$) and quiescent galaxies in the darkest shaded region ($\log(F_X/F_R) < -2$). Between these is a transitional zone populated by starburst galaxies and AGN (medium shading). Figure adapted from Barger et al. (2003).

1.4 Properties of the X-ray sources found in deep extragalactic surveys

A broad diversity of source types is found in deep *Chandra* and *XMM – Newton* surveys. This is apparent in even basic flux - flux plots such as that shown in Fig. 1.7: at the faintest X-ray flux levels in the CDFs, the extragalactic sources range in optical flux by a factor of ≥ 10000.

Classification of the X-ray sources detected in the deep surveys is challenging for several reasons. First, many of them are simply too faint for efficient optical spectroscopic identification with $8-10$ m class telescopes. Furthermore, most have modest apparent optical luminosities, and thus their host galaxies make substantial contributions to the flux measured in a spectroscopic aperture, preventing the detection of an AGN (Moran et al. 2002). Finally, as already stressed in the previous Sections, another challenge is the apparent "schism" between optical (type 1 vs type 2) and X-ray (unabsorbed vs absorbed) schemes

of classification: not all X-ray absorbed AGN have type 2 optical spectra, and not all AGN with type 1 optical spectra are unabsorbed.

Considering X-ray, optical and multiwavelength information, the primary extragalactic source types found in the deep surveys are the following:

- *Type 1 AGN:* blue, broad line AGN that do not show signs of obscuration at either X-ray or optical/UV wavelengths. They cover a broad range of redshift ($z \sim 0 - 5$) and comprise a significant fraction of the brightest X-ray sources (e.g. Barger et al. 2003; Szokoly et al. 2004). At $z \geq 1.5$ they also comprise a significant fraction of all X-ray sources with spectroscopic identifications, certainly in part because these objects are the most straightforward to spectroscopically identify.

- *Obscured AGN with clear optical/UV AGN signatures:* some objects showing X-ray evidence for obscuration have clear AGN signature in their rest - frame optical/UV spectra. Notably, such AGN can have both type 1 and type 2 optical/UV classification (e.g. Matt 2002). Most of these objects have $z \leq 1.5$.

- *Optically faint X-ray sources:* these objects have $I \geq 24$ and thus usually cannot be spectroscopically identified. Many, however, appear to be luminous, obscured AGN at $z \sim 1 - 3$ when their X-ray, optical (including photometric redshifts) and multiwavelength properties are considered (e.g. Alexander et al. 2001; Barger et al. 2003; Fiore et al. 2003; Treister et al. 2004; Zheng et al. 2004; Mainieri et al. 2005). Thus, these objects largely represent an extension of the previous class to higher redshifts and fainter optical magnitudes.

- *X-ray bright, optically normal galaxies (XBONGs):* some hypothesis on their nature were already presented in Section 1.2.

- *Starburst and normal galaxies:* at the faintest X-ray flux levels ($0.5 - 2$ keV fluxes below 5×10^{-16} erg cm^{-2} s^{-1}) a significant and rising (up to $30 - 40\%$) fraction of the detected sources appears to be starburst and normal galaxies at $z \sim 0.1 - 1.5$ (e.g. Hornschemeier et al. 2003; Bauer et al. 2004). At even fainter X-ray flux levels, normal and starburst galaxies should be the dominant class of extragalactic X-ray sources.

- *Group and clusters of galaxies:* groups and low luminosity clusters of galaxies at $z \sim 0.1 - 1$ are detected as extended, soft X-ray sources in

deep surveys (e.g. Bauer et al. 2002a; Giacconi et al. 2002; Rosati et al. 2002). Their X-ray luminosities ($10^{41.5} - 10^{43}$ erg s^{-1}), basic X-ray spectral properties ($kT \leq 3$ keV) and sizes appear broadly consistent with those of nearby groups and low luminosity clusters.

Morphological studies show that the AGN from deep X-ray surveys are generally hosted by galaxies with significant bulge components, and they do not show evidence for enhanced merging or interaction activity relative to normal field galaxies (e.g. Grogin et al. 2005). Many of the non broad line AGN have the rest frame colors of evolved, bulge - dominated galaxies, and there is little evolution of these colors from $z \sim 0 - 2$ (e.g. Barger et al. 2003; Szokoly et al. 2004). Most AGN from deep surveys are "radio quiet" in the sense that the ratio, R, of their rest frame 5 GHz and 4400 Å flux densities is $R < 10$ (Bauer et al. 2002b).

The combined results from deep and wider X-ray surveys show that the sources comprising most of the XRB have X-ray luminosities comparable to those of local Seyfert galaxies ($L_X \sim 10^{43}$ erg s^{-1}). While a few remarkable obscured quasar have been found, these appear fairly rare and only make a small contribution to the XRB. Indeed, it appears that the fraction of obscured AGN drops with luminosity from $\sim 60 - 70\%$ at Seyfert luminosities to $\sim 30\%$ at quasar luminosities (e.g. Ueda et al. 2003; Szokoly et al. 2004). Most spectroscopically identified AGN have $z \leq 2$, although a significant minority have $z \sim 2 - 5$. This is partly due to spectroscopic incompleteness bias (it is easier to measure redshifts for brightest objects, which are generally the nearest), however there is a real enhancement of AGN at $z \leq 1$ relative to the expectations from pre - *Chandra* AGN synthesis models of the XRB (see Section 1.5).

The observed sky density of AGN in the X-ray surveys (~ 6500 deg^2 in the deepest surveys) is about an order of magnitude higher than that found at any other wavelength with the current facilities. This exceptional effectiveness at finding AGN arise because X-ray selection has reduced absorption bias and minimal dilution by host galaxy starlight and allows concentration of intensive optical spectroscopy follow-up upon high probability AGN with faint optical counterparts (i.e. it is possible to probe further down the luminosity function).

1.5 Population synthesis models

The problem of the origin of the XRB is intimately linked to AGN. As already reported, it was soon realized that the XRB must be the result of the integrated emission of discrete sources, and AGN are the only possible candidates. However the XRB spectrum is much harder than the typical spectrum of an unabsorbed AGN. A possibility to reproduce the shape of the XRB spectrum is the existence of a significant number of absorbed AGN, with a suitable redshift distribution. A number of population synthesis models were developed in the context of the AGN unification model (e.g. Madau et al. 1994; Comastri et al. 1995; Wilman & Fabian 1999; Pompilio et al. 2000). With the increasing sensitivity of recent X-ray surveys, the population of absorbed AGN emerged and the main prediction of the AGN synthesis models was then confirmed. However, these models contained a number of implicit assumptions. For instance, the evolution of obscuration over cosmic time and the dependence of obscuration on intrinsic source luminosity were largely free parameters.

The main uncertainties are related to absorbed AGN. While the X-ray luminosity function (XLF) and evolution of unabsorbed AGN are rather well known (e.g. Miyaji et al. 2000), nothing was known about absorbed AGN. Comastri et al. (1995) showed that, assuming for the obscured AGN a distribution of absorbing column densities and the same evolution and XLF of unabsorbed ones, it was possible to fit the full XRB spectrum in the $\sim 1 - 100$ keV band, as well as the integral counts (logN-logS relation) in the $0.5 - 2$ and $2 - 10$ keV bands. Later, the local ratio between absorbed and unabsorbed AGN (in the Seyfert luminosity regime) was found to be about 4 (Maiolino & Rieke 1995), and the column density distribution of local Seyfert 2 was determined (Risaliti et al. 1999). Using these new constraints, Gilli et al. (1999) showed that, if the column density distribution of absorbed AGN is the same at all redshifts and luminosities, then additional absorbed sources at moderate/high redshifts are required to match the XRB constraints. Gilli et al. (2001) proposed that absorbed sources evolve slightly faster than unobscured ones. In particular, they favored a model where the ratio between absorbed and unabsorbed AGN increases from 4 at $z = 0$ to 10 at $z = 1.3$, where both populations stop evolving.

AGN synthesis models also showed that, while the XRB spectrum can be simply fitted with a population of Seyfert 2 galaxies in addition to unobscured AGN, the *ASCA* and *BeppoSAX* source counts in the $2 - 10$ keV band are matched only by assuming a population of luminous, obscured AGN, the so-

called type 2 QSOs (Gilli et al. 2001; Comastri et al. 2001).

A general problem for the population synthesis models is the low redshift peak observed in X-ray selected AGN samples in deep surveys (e.g. Szokoly et al. 2004; Barger et al. 2003), at $z \sim 0.7$, whereas the models predict a peak at $z \sim 2$, similar to optical quasar surveys (Boyle et al. 2000). Another problem is the discrepancy between the observed and predicted ratios of obscured to unobscured AGN. While, as said before, most models require a ratio of $4:1$ or higher to make up the hard X-ray peak in the XRB spectrum, the observed ratio in the deep X-ray surveys based on spectroscopic identifications is closer to $2:1$ (e.g. Barger et al. 2003; Szokoly et al. 2004).

It should also be noted that the population synthesis models are based on the assumption of a one to one correspondence between optical and X-ray properties, so that the XLF of X-ray unabsorbed AGN is based on that of optically type 1 AGN. As already shown, there is a significant number of cases where optical and X-ray classifications disagree, but there is not a clear estimate of how common these objects are.

Concerning type 2 QSOs, before the advent of *Chandra* and *XMM – Newton* only a few of them were known (e.g. Akiyama et al. 1998; Della Ceca et al. 2000; Franceschini et al. 2000). Deep X-ray surveys found indeed a large fraction of the objects to be obscured, but the number of identified type 2 QSOs was still very low compared to the model predictions. A significant fraction of high redshift, luminous obscured AGN may have escaped optical spectroscopic identification due to the weakness of their optical counterparts and misclassification due to the lack of AGN signature. On the other hand, Fiore et al. (2003) showed that medium deep X-ray surveys, covering relatively large sky areas at a higher flux limit, proved to be effective to select significant samples of type 2 QSO candidates among objects with high values of the X-ray to optical ratio. Nevertheless, their contribution to the XRB should not be dominant.

In the last few years, Cowie et al. (2003), Fiore et al. (2003) and Barger et al. (2005) independently demonstrated that the AGN number density for luminosities lower than 10^{44} erg s^{-1} peaks at lower redshift than that of high luminosity objects. The first model which was able to reproduce this result is that by Ueda et al. (2003), who determined the hard ($2-10$ keV) XLF of AGN up to $z = 3$ and found that the fraction of X-ray absorbed AGN decreases with intrinsic luminosity and that the evolution of the AGN hard XLF is best described by a luminosity dependent density evolution (LDDE), where the low luminosity AGN ($L_X \sim 10^{43}$ erg s^{-1}) peak at lower redshift than the high

luminosity AGN. This model is also able to reproduce the hard and soft source counts and the broad band spectrum of the XRB in the $0.5 - 300$ keV range.

La Franca et al. (2005) have determined the hard XLF up to $z \sim 4$, using an AGN sample 4 times deeper than the Ueda et al. (2003) one. They essentially confirm the findings of Ueda et al. (2003), and find that the fraction of X-ray absorbed AGN decreases with luminosity and increases with redshift. The difference with respect to the Ueda et al. (2003) findings is due to the larger and deeper sample used by La Franca et al. (2005).

These results mean that the luminous AGN (QSOs) formed in earlier epochs than less luminous AGN (Seyferts). The measure of the hard XLF cosmological evolution directly constrains the history of the formation of supermassive black holes (SMBHs). On the other hand, the accretion history of the SMBHs may have a strong link to the star formation history in their host galaxies. For example, Kauffmann & Haenelt (2000) showed that the optical luminosity function of quasars, its cosmological evolution and the cosmic star formation history can be well reproduced simultaneously with some reasonable assumptions in semianalythic models. According to Balland et al. (2003), the star formation of early type galaxies peaks earlier ($z \sim 3$) than that of late type galaxies ($z \sim 1.5$). This evolutionary difference is similar to that of the number density of AGN. A possible scenario is the following.

Luminous AGN have lived in galaxies that have large spheroids components at present, such as elliptical and S0 galaxies. Their SMBHs rapidly grew in accordance with strong starbursts that happened in early epochs of the universe (possibly as a result of mergers), followed by a rapid decrease of their activities after $z \leq 2$. On the other hand, galaxies that now have only small spheroids (i.e. spirals) made starbursts relatively later and/or slower than early type galaxies, and accordingly the activity of smaller mass (hence less luminous AGN) has continued until recently ($z < 1$). If the evolutionary history by Balland et al. (2003) is correct, the star forming activity peaks at somewhat earlier epochs (at $z \sim 3$ for early type and $z \sim 1.5$ for late type galaxies) than the AGN activity (at $z \sim 2$ for bright AGN and $z \sim 0.6$ for fainter ones). This would imply that the AGN activity of a galaxy occurs not in the same but in a later phase than the major starburst. However, an apparently weak AGN could be either a low mass black hole or a high mass black hole with a small accretion rate, making the actual picture more complex.

1.6 Aims and structure of the Thesis

As shown in the previous Sections, deep X-ray surveys have now resolved most of the XRB in the $0.5-2$ and $2-10$ keV energy bands, showing that the basic predictions of the XRB models are confirmed and finding a large number of X-ray absorbed AGN. However several problems remain. Worsley et al. (2005) have shown that a significant fraction of the XRB above 6 keV is still unresolved and as a consequence a large population of AGN, still undetected even in the deepest X-ray surveys, should exist.

Recently, a number of AGN not detected at X-ray energies have been identified at radio and IR wavelengths (Higdon et al. 2005; Donley et al. 2005; Polletta et al. 2006). On the other hand, *Chandra* and *XMM – Newton* observations show many X-ray sources sufficiently luminous to be AGN, but with no optical AGN characteristics (e.g. Green et al 2004, see also Section 1.4), and in the last few years many objects which show opposite X-ray and optical properties have been found (see Section 1.2). All these facts show that "what are a minimum set of properties which define an AGN?" is still an open question.

Since AGN are multiwavelength emitters, only a view in multiple wavebands can give a picture of the "true" AGN population. The XMM Medium Deep Survey (XMDS) and the associated multiwavelength projects permit to study large AGN samples throughout the entire wavelength spectrum, from radio to the X-rays. Hard X-ray selection over a large area ($\sim$ 1 deg^2) allowed us to obtain a sizable sample of X-ray sources (136), more than 90% of which are identified as AGN, thanks to the large photometric information. We used optical and IR data to construct the SEDs of our sources, to classify them and to compute photometric redshifts. We used X-ray spectra and/or hardness ratios to estimate the X-ray absorption and we investigated the relationship between the absorption in the X-rays and the dust obscuration at optical/IR wavelengths by comparing them as a function of X-ray flux, redshift and X-ray luminosity.

This Thesis is divided in three Parts. Part I includes this Introduction, a presentation of the XMDS and the associated surveys (Chapter 2) and a brief description of the scientific payload aboard the *XMM – Newton* observatory (Chapter 3). Part II is dedicated to data reduction. In Chapter 4 we briefly describe and the X-ray data reduction, while in Chapter 5 the optical and IR identification procedure is reported. In Part III we present our results. The logN-logS relationship obtained for the XMDS is shown and compared with

literature results in Chapter 6. We then present a hard X-ray sample, whose X-ray, optical and IR properties are compared in Chapter 7. The SEDs and template fitting process leading to the estimate of photometric redshifts are described in Chapter 8, while the X-ray spectral analysis is presented in Chapter 9. For sufficiently bright sources, X-ray spectra are analyzed individually, while for faint sources intrinsic absorption is estimated from hardness ratios. A stacking technique is instead used to derive average properties of different subsamples, such as optically obscured and unobscured AGN. The fraction of optically obscured and X-ray absorbed AGN is discussed as a function of redshift, X-ray flux and luminosity in Chapter 10. The surface density of optically obscured and unobscured AGN is estimated in Chapter 11, where we also derive the surface density of type 2 QSOs. Chapter 12 summarizes the results obtained. Throughout this Thesis $H_0 = 70$ km s^{-1}, $\Omega_\Lambda = 0.7$ and $\Omega_M = 0.3$ are assumed.

Chapter 2

The XMM Medium Deep Survey

2.1 Description of the XMM Medium Deep Survey

The XMM Medium Deep Survey (XMDS) is a joint effort of teams in three *XMM – Newton* hardware institutes (IASF Milan, Italy; Sérvice d'Astrophysique CEA Saclay, France; Institut d'Astrophysique et Géophysique, Liège, Belgium) which have dedicated part of their guaranteed time to observe a contiguous region of sky, to study the cluster and AGN evolution as a function of environment, in the context of structure formation.

The XMDS is the core of a wider, shallower survey, the XMM Large Scale Structure (XMM – LSS) survey (Pierre et al. 2004; Pacaud et al. 2006), which is principally devoted to clusters' study (Pierre et al. 2006). X-ray observations are associated with several surveys in the optical, IR, radio and UV, which will be described in the next Sections.

The survey location is such that follow-up observations with ground-based resources are possible from both hemispheres; it is at high galactic latitude, and was chosen not to contain known bright X-ray sources; a visibility of the field by *XMM – Newton* $> 15\%$ was also required. Given this, the survey field has been centered around $\alpha = 02\text{h } 26\text{m}$, $\delta = -4^\circ\ 30'\ 00''$.

The XMDS consists of 19 contiguous pointings, with typical exposure of about 20 ks, over an area of ~ 2.6 deg^2. The footprint of the pointings is shown is Fig. 2.1. The XMDS fields are surrounded by additional, shorter (typically 10 ks) pointings, performed as part of the XMM – LSS program, which currently cover an area of about 10 deg^2.

Observations were performed by EPIC MOS1, MOS2 and pn cameras in full frame mode with thin filter (see Chapter 3). The log of XMDS observations is reported in Table 2.1.

Field	ESA obs id	date	pointing RA	DEC	exposure (ks)		
					MOS1	MOS2	pn
G01	112680101	28 Jan 2002	02:27:25.4	-04:11:06.4	24.4	25.0	22.1
G02	112680201	14 Jul 2002	02:25:54.2	-04:09:05.6	9.8	9.8	7.2
G03	112680301	19 Jan 2003	02:24:45.6	-04:11:00.8	21.6	21.8	17.9
G04	109520101	29 Jan 2002	02:23:25.3	-04:11:07.6	25.8	25.7	20.1
G05	112680401	02 Feb 2002	02:28:05.1	-04:31:08.1	23.2	23.7	20.0
G06	112681301	26 Jul 2002	02:26:34.4	-04:29:00.8	12.7	13.0	8.6
G07	112681001	30 Jan 2002	02:25:25.3	-04:31:07.1	22.3	23.5	20.3
G08	112680501	25 Jul 2002	02:23:54.6	-04:29:00.1	18.1	18.3	15.3
G09	109520601	31 Jan 2002	02:22:45.2	-04:31:11.1	22.4	22.3	16.9
G10	109520201	29 Jan 2002	02:27:25.4	-04:51:04.4	24.7	24.8	19.0
G11	109520301	02 Feb 2002	02:26:05.1	-04:51:06.1	21.7	21.9	16.5
G12[a]	109520401	01 Feb 2002	02:24:45.4	-04:51:11.2	n/a	n/a	n/a
G13	109520501	03 Jul 2001	02:23:13.1	-04:49:03.1	23.8	23.9	18.2
G14	112680801	31 Jan 2002	02:22:04.1	-04:51:09.7	13.6	13.6	8.5
G15	111110101	06 Jul 2001	02:27:54.1	-05:09:02.3	21.2	20.8	14.5
G16a[b]	111110201	06 Jul 2001	02:26:34.2	-05:09:03.1	3.5	3.9	1.4
G16b[b]	111110701	14 Aug 2001	02:26:35.2	-05:08:46.6	11.7	11.7	7.5
G17	111110301	03 Jul 2001	02:25:14.3	-05:09:08.4	22.5	22.1	17.9
G18	111110401	03 Jul 2001	02:23:54.1	-05:09:09.7	27.6	28.1	19.9
G19	111110501	04 Jul 2001	02:22:34.0	-05:09:02.1	23.2	23.7	17.6

[a]: No useful data could be extracted from the observation G12 because of high background (see text).

[b]: Observation of pointing G16 has been repeated since the first instance was curtailed.

Table 2.1: Journal of XMDS observations; more details available through our ancillary web page `http://cosmos.iasf-milano.inaf.it/~lssadmin/Website/LSS/Anc/xmdsepic.html`

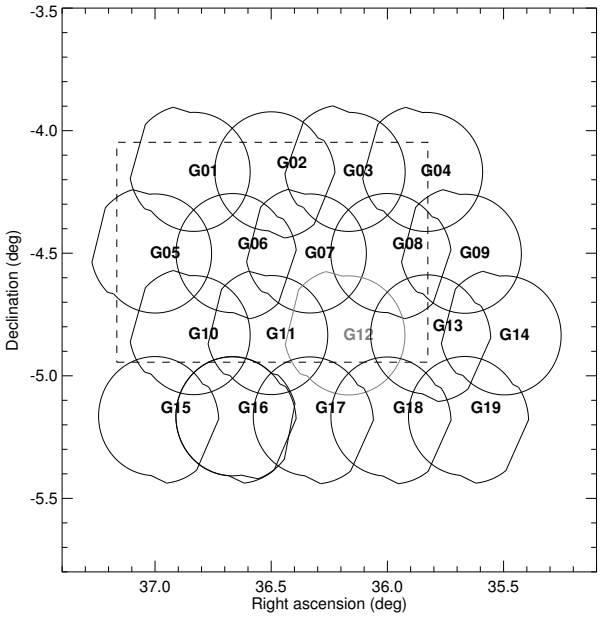

Figure 2.1: Location of the XMDS pointings on the sky: the approximate FOV footprint (with the pn protruding at the actual roll angle) is shown (solid lines; the gray colour for field G12 indicates that this field has not been used, see text). The dashed rectangle indicates the area of VVDS $BVRI$ photometry.

2.2 Associated multi-wavelength surveys

While optical information remains the primary source for X-ray source identification, contribution from other wavebands is critical to characterize the nature of the proposed identifications. A multiwavelength coverage provides an overview of the energy emission and absorption processes in astronomical objects, which is vital to our understanding of the AGN physics, formation and evolution (see Chapter 1). The contiguous design of the survey provides considerable advantages for complementary observations, compared to serendipitous fields, and numerous collaborations have been developed to obtain a very broad wavelength coverage. The main characteristics of associated surveys are outlined below.

2.2.1 Optical data

About half of the XMDS area is covered in the optical band by the VIMOS VLT Deep Survey (VVDS, Le Fèvre et al. 2004), both by $UBVRIJK$ photometry and by multi - object spectroscopy (see Fig. 2.1). $BVRI$ photometry was

obtained at the Canada France Hawaii Telescope with the CFH12K camera over a total area of 1.2 deg^2 at limiting magnitudes of $B_{AB} \sim 26.5, V_{AB} \sim 26.2, R_{AB} \sim 25.9$ and $I_{AB} \sim 25.0$ (50% completeness for point sources, see McCracken et al. 2003). The U band imaging was performed over an effective area of ~ 0.71 deg^2 with the Wide Field Imaging (WFI) mosaic camera on the ESO MPI 2.2 m telescope at La Silla, Chile. Two different U filters were used, the ESO U/360 filter and the Loiano observatory U filter. The limiting magnitude is $U_{AB} \sim 25.4$ (see Radovich et al. 2004). A small area (~ 165 arcmin^2) within the VVDS has also been observed in the J and K bands down to a limiting magnitude of $J_{AB} \sim 24.2$ and $K_{AB} \sim 23.9$ (50% completeness for point sources) with the SOFI instrument mounted on the ESO NTT telescope. A detailed description of the K band imaging survey is reported in Iovino et al. (2005).

Optical spectroscopy with the VIsible Multi Object Spectrograph (VIMOS) on the ESO – VLT UT3 is in progress; at present spectra for 11564 objects over a total area of 0.61 deg^2 in the apparent magnitude range $17.5 \leq I_{AB} \leq 24$ have been obtained (Le Fèvre et al. 2005). The useful wavelength range is $5500-9400$ Å.

The XMDS area is also within the sky region covered by the Canada France Hawaii Telescope Legacy Survey (CFHTLS), a large collaborative project between the Canadian and French communities. Observations are made using the wide field imager MegaPrime equipped with MegaCam, in the *u* g' r' i' z'* filters[1]. The "Wide" survey will cover 170 deg^2 in three patches of 49 to 72 deg^2; the "Deep" survey will cover 4 deg^2 in four independent fields of area 1 deg^2 each. Both the Wide survey field W1 (8 deg $\times$ 9 deg) and the Deep survey field D1 (1 deg $\times$ 1 deg) cover the XMDS and XMM - LSS region; D1 observations have been completed, while W1 observations are in progress. In the following we will use the D1 notation for data from the CFHTLS Deep and the W1 notation for data from the CFHTLS Wide. The completeness limits are $i' = 24.5$ for W1 (Hoekstra et al. 2006) $i' = 26.1$ for D1 (Semboloni et al. 2006).

2.2.2 Infrared data

Near-infrared observations of the XMM-LSS area are also in progress in the context of the UKIDSS, which is a program of five individual surveys covering

[1]see details at `http://www.cfht.hawaii.edu/Science/CFHLS/`

the wavelength range $0.83 - 2.37\mu$m and extending over both high and low galactic latitudes (Dye et al. 2006; Lawrence et al. 2006). The survey uses the Wide Field Camera (WFCAM) of the 3.8 m United Kingdom Infrared Telescope (UKIRT). The XMM-LSS region is one of the four target fields of the Deep Extragalactic Survey (DXS). Observations in the J and K filters down to $J = 22.3$ and $K = 20.8$ (Vega system) are in progress. About 0.8 deg^2 of sky have been observed up to now and part of the data are available in the UKIDSS Early Data Release (Dye et al. 2006). The photometric system used in the UKIDSS is described in Hewett et al. (2006).

The XMM-LSS field is also part of the *Spitzer* Wide-Area InfraRed Extragalactic Legacy Survey[2] (SWIRE, Lonsdale et al. 2003), which is one of six large programs undertaken as legacy surveys during the first year of the *Spitzer* Space Observatory. SWIRE has imaged nearly 49 deg^2 of the sky, divided among 6 different regions, selected to be the best possible infrared fields for detecting faint infrared galaxies and quasars. In the XMM-LSS field, observations were performed by the Infrared Array Camera (IRAC) at 3.6, 4.5, 5.8 and 8.0 μm to a 5 σ depth of 4.3, 8.3, 58.5, 65.7 μJy respectively and by the Multiband Imaging Photometer (MIPS) at 24, 70 and 160 μm to a 5 σ depth of 0.24, 15 and 90 mJy respectively. The SWIRE observations cover 95% of the XMDS field. Details on the SWIRE data and source catalogues are given in Surace et al. (2005).

2.2.3 Radio data

Radio observations have been obtained with the Very Large Array (VLA) at 1.4 GHz over an area of 1 deg^2 at a depth of 80 μJy (5 σ limit) and a resolution of $6''$ (see Bondi et al. 2003).

There is also a larger, shallower survey performed at VLA at 325 MHz (depth 275 mJy, area 110 deg^2) and 74 MHz (depth 4mJy, area 5.6 deg^2), described in Cohen et al. (2003).

2.2.4 UV data

In the UV domain, the XMM – LSS field is one of the targets of the Galex Deep Survey, whose main goal is to map the global history of star formation out to $z \sim 2$. However UV data were not used for the work presented in this Thesis.

[2] `http://swire.ipac.caltech.edu/swire/swire.html`

2.3 The XMM – LSS Database

The web site of the XMM – LSS Master Catalogue[3] contains information on aim and status of surveys involved in the consortium projects and X-ray data reduction pipeline, and gives access to the database[4]. Designed to be a working tool for the XMDS and XMM – LSS consortia, the database is now partially open to public access, as explained in Chiappetti et al. (2005).

The database presently includes data tables for:

- the results of the pipeline presented in Chapter 4 on XMDS data and those of an independent pipeline developed in Saclay for the analysis of the whole XMM – LSS data, best suited for extended sources (see Pacaud et al. 2006);
- VVDS photometry in the $UBVRIJK$ bands (see Section 2.2.1) for all objects within a $40''$ box around an X-ray source;
- photometric redshifts for the VVDS sources and spectroscopic redshifts when available;
- $u^*g'r'i'z'$ photometry obtained from the CFHTLS (see Section 2.2.1) both in the D1 and W1 fields within $9''$ radius from an X-ray source;
- mid infrared data from SWIRE (see Section 2.2.2) within $9''$ radius from an X-ray source;
- radio data from the VIRMOS 1.4 GHz Catalogue and from the Cohen et al. (2003) survey (see Section 2.2.3) within $40''$ box around an X-ray source;
- spectroscopic information from the XMM – LSS follow-up programs and the list of XMM – LSS confirmed or candidate clusters;
- the list of objects included in the SIMBAD[5], NED[6] and USNO A2 catalogue[7] within $20''$ from an X-ray source.

[3] `http://cosmos.iasf-milano.inaf.it/~lssadmin/Website/LSS`

[4] `http://cosmos.iasf-milano.inaf.it/~lssadmin/Website/LSS/Query`

[5] Set of Identifications, Measurements and Bibliography for Astronomical Data, `http://simbad.u-strasbg.fr/`

[6] NASA/IPAC Extragalactic Database, `http://nedwww.ipac.caltech.edu/`

[7] US Naval Observatory A2.0 Catalogue, `http://www.nofs.navy.mil/data/fchpix/`

There are also the following data products available:

- X-ray images and exposure maps for the XMDS pointings in the five energy bands $0.3 - 0.5$, $0.5 - 2$, $2 - 4.5$, $4.5 - 10$ and $2 - 10$ keV (see Section 4.2.2);
- finding charts in the I band of dimension $40'' \times 40''$ centered on X-ray sources position (in FITS format for sources in the VVDS area and as PNG images elsewhere);
- radio maps at 74 and 325 MHz.

The database also includes the first XMDS Catalogue, i.e. the catalogue of sources detected at $> 4\ \sigma$ in the XMDS and identified with an optical (or radio) counterpart. It is presented in Chapter 5 and in Chiappetti et al. (2005) (hereafter Paper I). The access to X-ray, VVDS and radio data for sources in this Catalogue is public.

Chapter 3

The *XMM – Newton* satellite

In the following we provide a brief description of the *XMM – Newton* satellite. More information on *XMM – Newton* can be found in the *XMM – Newton* Users' Handbook[1].

XMM – Newton is an European Space Agency (ESA) mission, launched on December 1999. It carries three Wolter type-1 X-ray telescopes, equipped with different detectors, and a 30 cm optical/UV monitor. Three different science instruments are on board of *XMM - Newton*:

- the European Photon Imaging Camera (EPIC), which consists of 2 MOS (Metal Oxide Semi-conductor) and one pn Charge-Coupled Device (CCD) arrays located at the prime focus of each of the three X-ray telescopes behind six-position filters (see Section 3.1.2). These CCDs are suited for X-ray imaging and moderate resolution X-ray spectroscopy.

- Two Reflection Grating Spectrometers (RGS), which provide high-resolution spectral information (E/dE from 200 to 800 over the energy range 0.35-2.5 keV). The RGSs are two identical grating structures on two mirror modules that deflect half of the beam on two of the X-ray telescopes. In fact, the RGSs are mounted in the light path of the two X-ray telescopes which have the EPIC MOS cameras at their primary focus and share the mirror with the MOS.

- The Optical Monitor, which can observe simultaneously a smaller region than the X-ray telescopes, but in the ultraviolet and visible wavelengths.

This work is based on observations with EPIC cameras, that will be described in detail in Section 3.1.

[1] `http://xmm.vilspa.esa.es/external/xmm_user_support/documentation/uhb/XMM_UHB.html`

Instrument	MOS1-2	PN	RGS1-2	OM
Bandpass	0.15-12 keV	0.15-15 keV	0.35-2.5 keV	180-600 nm
Field of view (FOV)	$30'$	$30'$	$\sim 5'$	$17'$
PSF (FWHM/HEW)	$5''/14''$	$6''/15''$	N/A	$1.4''$-$1.94''$
Pixel Size	$1.1\ ''$	$4.1''$	$9 \times 10^{-3} \AA$	$0.476''$
Spectral resolution[a]	$\sim$ 70 eV	$\sim$80 eV	$0.04/0.025 \AA$	0.5/1 nm

[a]: At 1 keV energy. At the energy of Fe Kα (6.4 keV), the energy resolution of both EPIC cameras is $\sim$ 150 eV.

Table 3.1: *XMM – Newton* basic characteristics.

The most important parameters of *XMM – Newton* are compiled in Table 3.1, and a comparison with other X-ray satellites is provided in Table 3.2. By examining this Table it becomes clear that *XMM – Newton* and *Chandra* are complementary in their attributes with various combinations of effective areas, angular and spectral resolutions, and energy ranges. The major points of *XMM – Newton* are the exceptionally large effective area and the broad energy range.

The main characteristic of *XMM – Newton* are:

- possible simultaneous operation of all science instruments, if not prohibited, e.g. by target brightness constraints;
- high sensitivity: *XMM – Newton* carries the X-ray telescopes with the largest effective area for a focusing telescope ever flown (see Table 3.2). The total mirror geometric effective area at 1.5 keV energy is $\sim$ 1550 cm^2 for each telescope, i.e. 4650 cm^2 in total, but the MOS have a lower effective area that the pn, because only part of the incoming radiation falls onto these detectors, which are partially obscured by the RGSs;
- angular resolution: the achieved point-spread function (PSF) has a full width at half maximum (FWHM) on the order of $6''$ and a Half Energy Width (HEW, at which 50% of the total energy is encircled) of $\sim 15''$;
- moderate (EPIC) and high (RGS) spectral resolution (see Table 3.1);
- long continuous target visibility: a highly elliptical orbit offers continuous target visibility of up to about 40 hours, with a minimum height for science observations of 46,000 km. This is very favorable for studies of source variability.

Satellite	PSF (FWHM) ($''$)	PSF (HEW) ($''$)	Energy band (keV)	A_e at 1 keV (cm^2)
XMM – Newton	6	15	0.15 - 15	4650
Chandra	0.2	0.5	0.1 - 10	800
ROSAT	3.5	7	0.1 - 2.4	400
ASCA	73	174	0.5 - 10	350

Table 3.2: Comparison of XMM-*Newton* with other X-ray satellites

The telescopes focal length is 7.5 m and the diameter of the largest mirrors is 70 cm. Each of the three X-ray telescopes on board *XMM – Newton* consists of 58 Wolter I grazing-incidence mirrors, which are nested in a coaxial and cofocal configuration to increase the effective area. The design of the optics was driven by the requirement of obtaining the highest possible effective area over a wide range of energies, with particular emphasis in the region around 7 keV. In particular, the design of *XMM – Newton* has been driven by the requirement of having a very shallow grazing angle of $30'$ in order to provide sufficient reflectivity at high energies.

Each telescope includes, apart from the mirror modules, baffles for visible and X-ray stray-light suppression and an electron deflector for diverting soft electrons. The detector layout and the baffled X-ray telescope FOV of both types of EPIC camera are shown in Fig. 3.1. For all cameras the sensitive area of the detector is about $30'$ across.

The effective area (A_e) is one of the most important parameters of a telescope and reflects the ability of the mirrors to collect radiation at different photon energies. Fig. 3.2 (left panel) shows the effective areas derived with the ready-made EPIC response matrices in case of full-frame mode (see Section 3.1) and with the thin filter applied (see subsection 3.1.2) for all the different instruments. The *XMM – Newton* mirrors are most efficient in the energy range from 0.1 to 10 keV, with a maximum at about 1.5 keV and a pronounced edge near 2 keV (the Au M edge).

The effective area of the mirrors is a function of the off-axis angle (i.e. the distance from the center of the FOV) . With increasing off-axis angle, less of the photons entering the telescopes actually reach the focal plane. This effect, called "vignetting", is principally due to the shadowing of the inner shells by the outer shells yielding a decrease of the effective area, that becomes larger as the photon energy increases. This effect is described by the vignetting function,

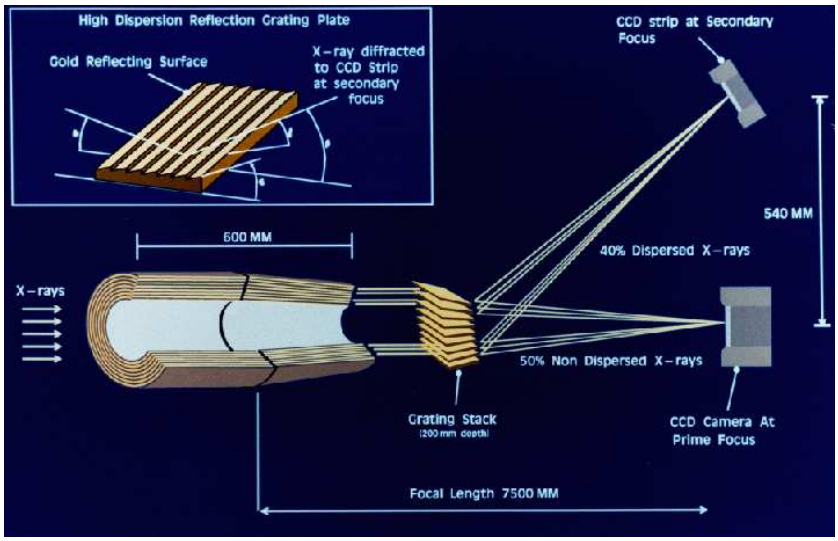

Figure 3.1: Light path in the *XMM – Newton* for the two telescopes in which a RGS is mounted into the optical path. Figure adapted from the *XMM – Newton* Users' Handbook.

which is the ratio of the off-axis area and the on-axis area at a fixed energy. The vignetting function for different energies is shown in Fig. 3.2 (right panel).

3.1 The EPIC Cameras

As already described, two Wolter X-ray telescopes are equipped with EPIC MOS CCD arrays, while the third carries a different CCD camera, the EPIC pn. Since the pixel size of MOS and pn cameras are of $1.1''$ and $4.1''$ respectively (see Table 3.1), the EPIC's angular resolution is determined by the PSF of the mirror modules ($\sim 6''$).
The *XMM – Newton* EPIC cameras allow to perform extremely sensitive imaging observations (in the 0.15–10 keV energy range) with moderate spectral ($E/\Delta E \sim 20-50$) and angular resolution ($6''$ FWHM; $15''$ HEW) over a field of view (FOV) of $30'$. All the EPIC CCDs operate in photon counting mode with a fixed, mode dependent frame read-out time frequency, producing event lists (which contain the x and y at which the events are registered, their energy and their arrival time). The two types of EPIC cameras (pn and MOS) are fundamentally different, while the two MOS arrays (MOS1 and MOS2) are basically the same cameras but they are rotated by 90% with respect to each other.

The MOS cameras consist of 7 individual identical, front-illuminated chips, while the heart of the pn camera is a single silicon wafer with 12 CCD chips

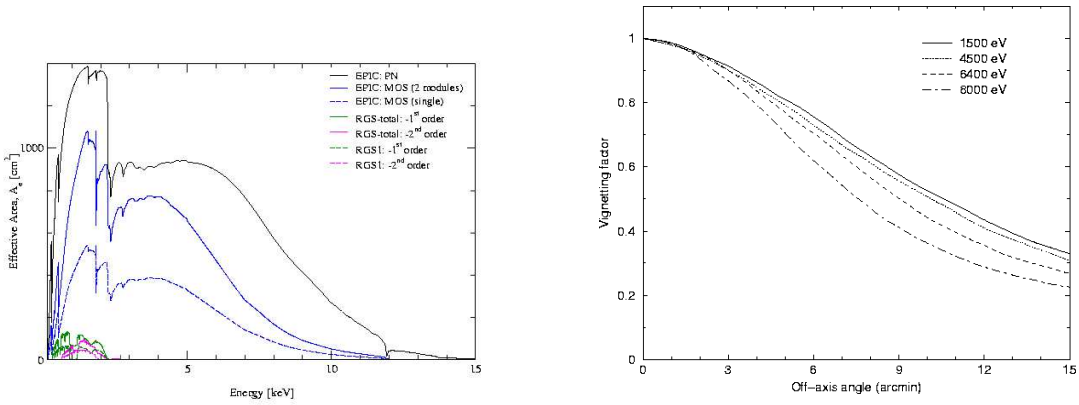

Figure 3.2: Left panel: the net effective area of all *XMM – Newton* X-ray telescopes, combined with the response characteristics of the focal X-ray instruments, EPIC and RGS (linear scale). Right panel: vignetting function of the X-ray telescope in front of the pn camera as a function of off-axis angle (0′-15′, based on simulations) at a few selected energies. Figure adapted from the *XMM – Newton* Users' Handbook.

integrated. The MOS and pn chip array numbering scheme, the individual chip coordinate frames and the directions of the detector coordinates are displayed in Fig. 3.3.

A major difference between MOS and pn is the readout time, much faster in the pn, because each pixel column has its own readout node. With this camera high-speed photometry of rapidly variable targets can be conducted, down to a minimum integration time of 30 (7) μs in the timing (burst) mode. On the other hand, the out of time events contamination is more severe in pn.

The EPIC cameras allow several modes of data acquisition. In "full frame" and "extended full frame" (pn only) all pixels of all CCDs are read out and thus the full FOV is covered. In the case of MOS, the central CCD can also be operating separately ("partial window" mode), while the pn camera can also be used in "large window" mode (half of the area in all 12 CCDs is read out) or "small window" mode (only a part of CCD number 4 is used). Observations of the XMDS were performed in full frame mode.

3.1.1 The *XMM – Newton* Point-Spread Function (PSF)

The first critical parameter which determines the quality of an X-ray mirror is its ability to focus photons. Each of the three Wolter type I X-ray telescopes on board *XMM – Newton* has its own PSF. Moreover the PSF could vary with the off-axis angle and with the energy. One of the most important characteristic of

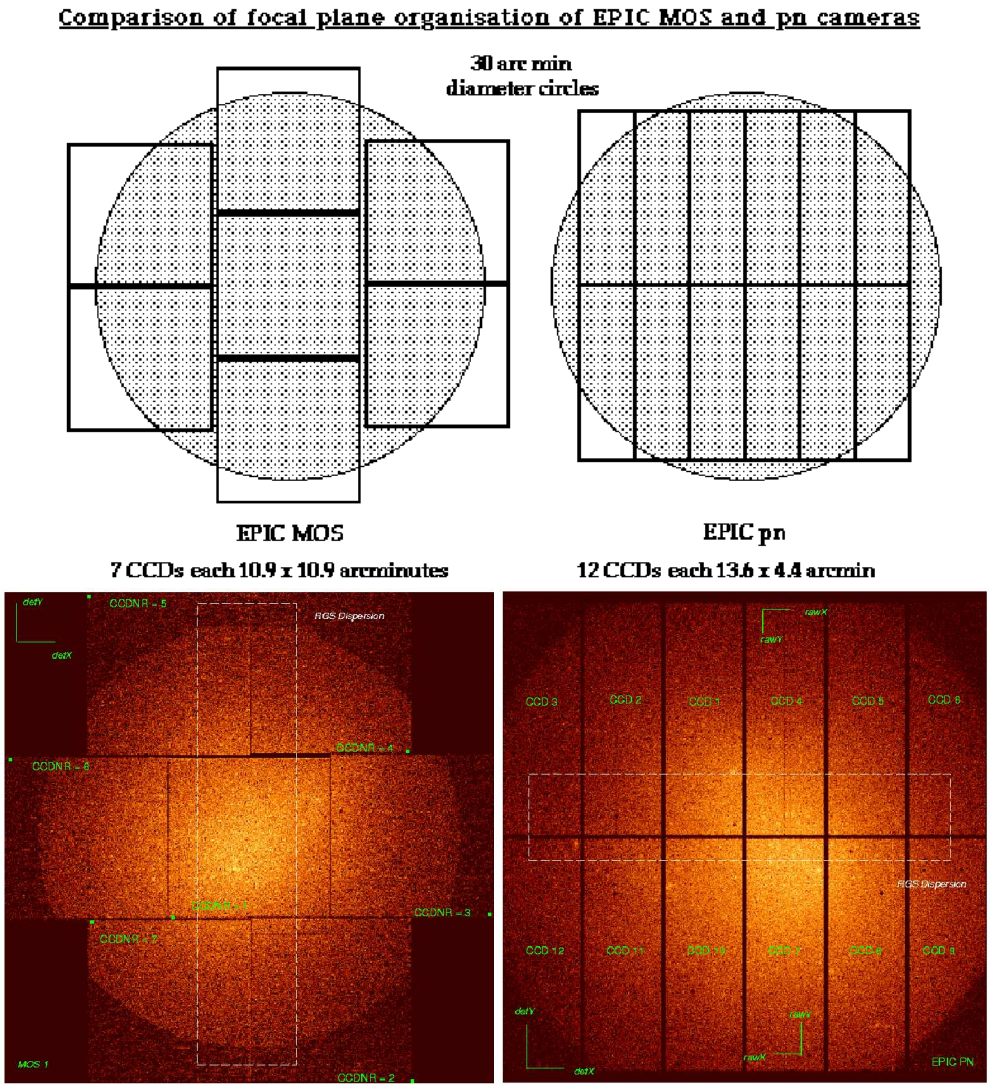

Figure 3.3: Upper panel: Rough sketch of the field of view of the two types of EPIC camera, MOS (left) and pn (right). The shaded circle depicts a 30′ diameter area. Lower left panel: layout of the EPIC MOS1 camera. The orientation of the DETX/DETY axes are shown, highlighting that the RGS dispersion axes are parallel within spacecraft physical coordinates. Lower right panel: layout of the EPIC pn camera; the orientation of the RAWX/RAWY (CCD specific) and of the DETX/DETY axes are shown. Figure adapted from the *XMM – Newton* Users' Handbook.

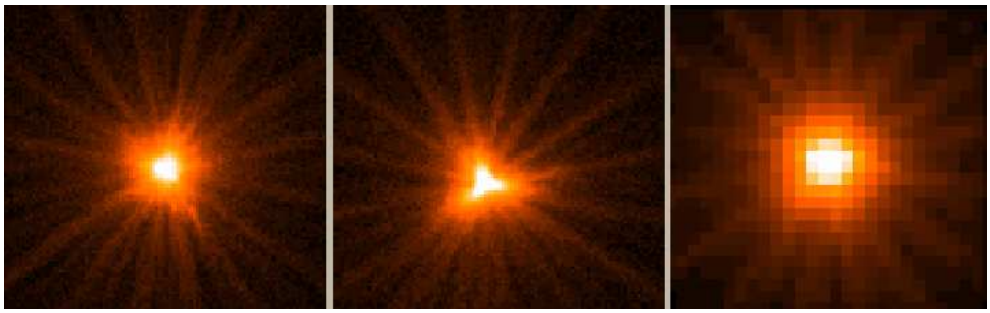

Figure 3.4: On axis point spread function of the MOS1, MOS2 and pn X-ray telescopes (left to right) registered on the same source, with each MOS camera in Small Window Mode, and the pn camera in Large Window Mode (see Section 3.1). The star-like pattern is created by the spider which supports the 58 co-axial Wolter I mirrors of the telescope. The shape of the point spread function core is slightly different for all cameras, with MOS2 having a somewhat triangular shape. Figure adapted from the *XMM – Newton* Users' Handbook.

XMM – Newton is that the core of its on-axis PSF is narrow and varies little over a wide energy range (0.1–4 keV). Above 4 keV, the PSF becomes only slightly more energy dependent. As an example, Fig. 3.4 shows the in orbit on-axis PSF of the MOS1, MOS2 and pn X-ray telescopes, registered on the same source. This figure is primarily provided to show the shape of the PSFs, with for example the radial substructures caused by the spiders holding the mirror shells. Values for the full width at half maximum (FWHM) and half energy width (HEW) of the PSFs (both in orbit and ground measurements) are listed in Table 3.3.

As said above the PSF is a function of the energy and of the off-axis angle; in particular at large off-axis angles it is elongated due to off-axis aberration (astigmatism). The on-axis fractional encircled energy as a function of the angular radius and at different energies is shown in Fig. 3.5. The shape of the PSF at different off-axis angles can be parameterized through the extraction radius at which 90% of the source photons are encircled (W90). Fig. 3.6 shows this radius as a function of the off-axis angles for different photon energies. As can be seen, as the off-axis angle increases the energy dependence of the PSF changes, since focusing of high energy photons is no longer confined to the inner shells. A large fraction of these high energy photons are redistributed into the wings of the PSF by X-ray scattering, hence W90 is larger at high energies than at soft energies and for large off-axis angles.

	pn orbit/ground	MOS1+RGS1 orbit/ground	MOS2+RGS2 orbit/ground
FWHM	<12.5 ″/6.6 ″	4.3 ″/6.0 ″	4.4 ″/4.5 ″
HEW	15.2″/15.1 ″	13.8 ″/13.6 ″	13.0″/12.8 ″

Table 3.3: The on-axis in orbit and on ground 1.5 keV PSFs of the different X-ray telescopes

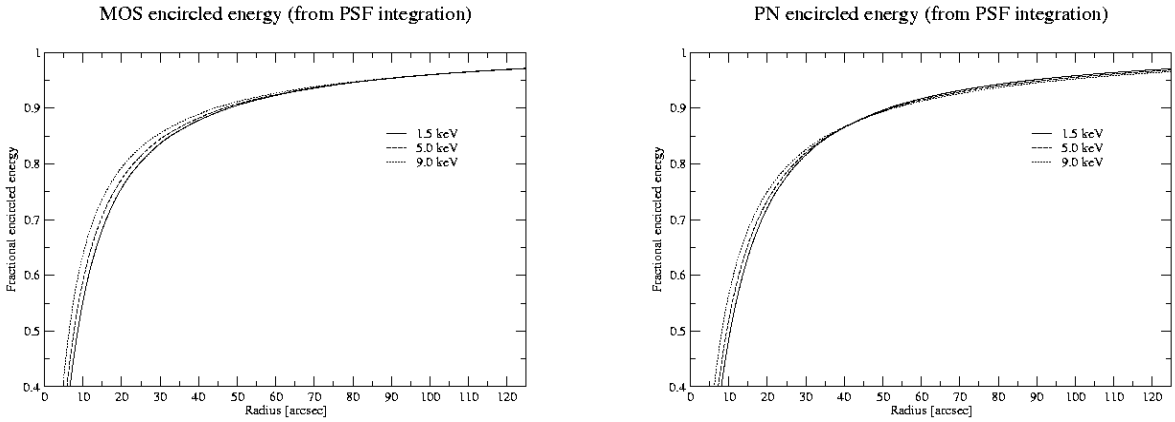

Figure 3.5: The MOS (left panel) and pn (right panel) fractional encircled energy as a function of angular radius (on-axis) at different energies. Figure adapted from the *XMM – Newton* Users' Handbook.

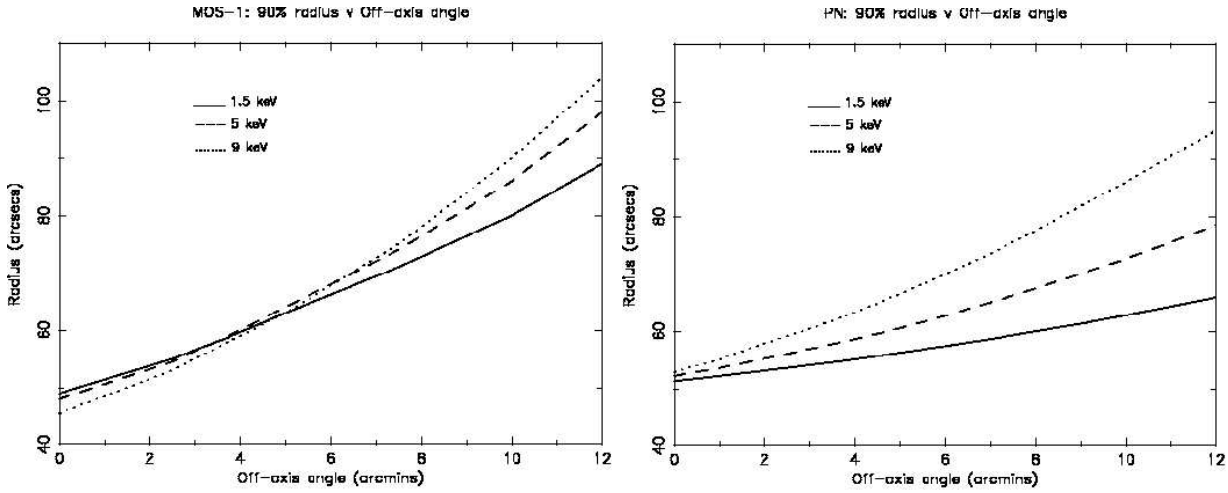

Figure 3.6: Dependence of the W90 radius on the off-axis angle at different energies for a point source observed with the MOS (left panel) and pn (right panel). The curves were calculated assuming a fractional encircled energy of 100% at a radial distance of $5'$, independent of the off-axis angle. Figure adapted from the *XMM – Newton* Users' Handbook.

3.1.2 The *XMM – Newton* filters

The EPIC CCDs are equipped with three different aluminized optical blocking filters that influence the effective area, in particular in the low energy part of the pass-band. These filters, named "thick", "medium" and "thin", are used because the EPIC CCDs are sensitive not only to X-ray photons, but also to IR, visible and UV light. The effects of these photons are mainly: increase of the system noise, incorrect energy scale (because of finite offset for the nominally zero signal) and excess signal and noise fluctuations.

The effect of the different filters on the X-ray response for the pn camera is shown in Fig. 3.7. The use of a thick blocking filter (capable of minimizing the optical light contamination) will necessarily limit the softest X-ray energy response. It should be noted that also an off-axis bright optical object will leak through the filters, generating false X-ray events which could contribute to degrading the effective telemetry bandwidth. For XMDS observations, the thin filter was used.

3.1.3 EPIC background

Both the cosmic X-ray background (XRB), and an instrumental component contribute to the background on EPIC cameras.

The XRB is made by two substantially different components: a soft (at

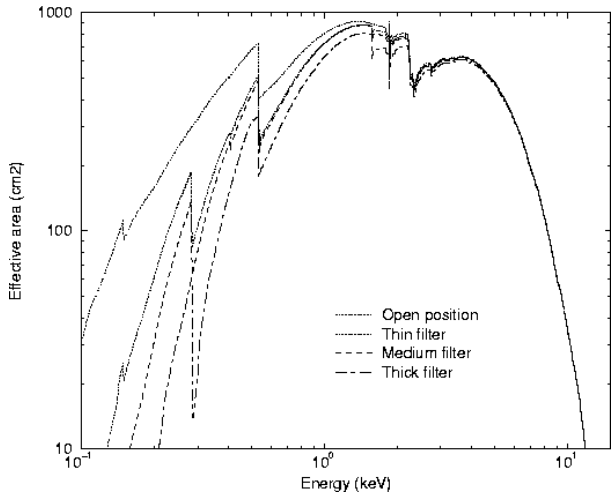

Figure 3.7: The EPIC pn effective area for each of the optical blocking filters applied and without filter. Figure adapted from the *XMM – Newton* Users' Handbook.

energies below 2 keV) and a hard component (above 2 keV). The soft component shows a strong anisotropy, as observed by Tanaka & Bleeker (1977) and is mainly of galactic origin. In the $0.1 - 0.5$ keV band, the background is mostly due to a local bubble with a temperature of about 10^6 K. Above 0.5 keV a large fraction of the soft XRB is produced by thermal emission from hot gas ($T \sim 2.2 \times 10^6$ K) in our Galaxy (Hasinger 1992; Wang & McCray 1993). On the other hand, the hard component is highly uniform and almost entirely of extragalactic origin. It was extensively described in Section 1.3.

The instrumental contribution may be further divided into a detector noise component, which becomes important at low energies (i.e. below 200 eV) and a particle background, caused by their interactions with the structure surrounding the detectors and the detectors themselves. This component is characterized by a flat spectrum and is particularly important at high energies (i.e. above a few keV).

Detector noise

The dark currents of both types of EPIC CCD are negligible sources of background noise under nominal operating conditions.

In MOS there are low level "flickerings" of a small number of pixels at an occurrence rate $< 1\%$. In pn occasional (mainly during high particle background) the offset calculation leads to a slightly under estimate of the offset in some pixels, which can result in blocks of approximatively 4×4 pixels with enhanced low energy signal.

Particle induced background

This component can be further divided into 2 components: an external 'flaring' component, characterized by strong and rapid variability, which is often totally absent, and a second more stable internal component, always present.

The flaring component is attributed to soft protons (E_p smaller than a few 100 keV), which are presumably funneled towards the detectors by the X-ray mirrors. The current understanding about these phenomena is that soft protons are most likely organized in clouds populating the Earth's magnetosphere. The number of such clouds encountered by *XMM – Newton* in its orbit depends upon many factors, such as the altitude of the satellite, its position with respect to the magnetosphere, and the amount of solar activity, therefore their impact is highly variable (see examples from our observations in Chapter 4).

The stable component is due to the interaction of high-energy particles (E larger than some 100 MeV) with the structure surrounding the detectors and possibly the detectors themselves. This component shows only small intensity variations in time which are typically observed on long time-scales. The intensity of the quiescent component has been measured for both MOS and pn cameras during CLOSED filter observations. In the case of the MOS cameras the intensity in the $2-7$ keV range (which is free of the most prominent fluorescent lines) is found to be $\sim 2.2 \times 10^{-3}$ cts cm^{-2} s^{-1} keV^{-1} (3.0×10^{-8} cts arcsec^{-2} s^{-1} keV^{-1}). For the pn camera, the intensity in the same energy range is $\sim 5 \times 10^{-3}$ cts cm^{-2} s^{-1} keV^{-1} (6.7×10^{-8} cts arcsec^{-2} s^{-1} keV^{-1}).

3.1.4 Event reconstruction

Event selection is performed on-board in order to allow transmission of useful data only (i.e., removal of empty pixels from the data stream). A significant number of X-ray events are expected to be split between pixels, and these must be recognized as such. The Science Analysis Subsystem (SAS) software allows these data to be reconstructed to a single energy value in an event list. For MOS cameras, a real time on-board recognition scheme filters out cosmic ray tracks and transmits to the ground exclusively the information supposedly related to X-ray events. The board recognition scheme looks for a local enhancement of signal in flat fielded images. The signal is defined with respect to a threshold value set by telecommand for each observation. An event is identified if in a 5×5 pixel matrix, pixels above threshold form a predefined pattern. In case of imaging mode, 32 patterns have been defined, shown in Fig. 3.8 (upper panel). They

each correspond to an isolated event, i.e. to a zone above threshold completely encircled by pixels below threshold. Good X-ray pattern must be compact, with the highest charge at the center (pattern $0 - 25$). Single events are those in which a single pixel is above threshold (pattern 0), in double events there are 2 pixels over the threshold (patterns from 1 to 4), in triple events 3 pixels are over the threshold (patterns from 5 to 8), and so on. On-ground calibration of the imaging mode has shown that soft X-rays mainly generate patterns from 0 to 12, corresponding to compact regions of X-ray energy deposition. However pattern 0 events comprise most of the valid X-ray events with the most accurate energy resolution.

In contrast to the MOS, all non bad pn events supposedly related to X-rays are transmitted to the ground and the pattern recognition and recombination of split partner is done off-line by the SAS task `epevents`. Filtering of an EPIC pn dataset is entirely performed by the EPIC pn pipeline processing. For pn, 13 valid patterns (from 0 to 12) have been defined. As in case of the MOS, pattern 0 events are single pixel events. These comprise most of the valid X-ray events with the most accurate energy resolution.

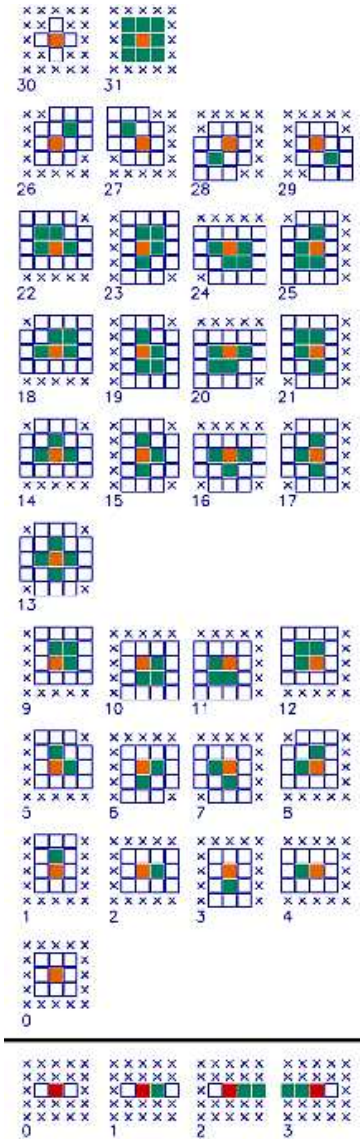

Figure 3.8: List of EPIC MOS patterns for imaging mode (upper panel) and for timing mode (lower panel). The pixel with the highest charge is colored in red, the other pixels above threshold in the pattern are colored in green, all pixel colored in white must be below threshold, the crossed pixels are indifferent (they can be above threshold). The philosophy for patterns $0 - 25$ is that a good X-ray pattern must be compact, with the highest charge at center, and isolated (all pixels around are below threshold). Patterns $26 - 29$ are so-called diagonal patterns, not expected from a genuine X-ray, but which can arise in case of Si-fluorescence or of pileup of two monopixel events. The scheme for timing mode should be interpreted in the same way as imaging mode, with the difference that the place where maximum charge occurs is ignored. Due to this, all doubles appear as pattern 1. Patterns 2 and 3 are mostly not due to true X-rays, but to cosmic-ray tracks. Figure adapted from the *XMM – Newton* Users' Handbook.

Part II

Data reduction

Chapter 4

The X-ray analysis

In this Chapter we will describe the X-ray data reduction and the source detection and characterization procedure. Our pipeline was written to detect pointlike sources, such as AGN. An independent pipeline has been developed in Saclay for the analysis of the whole XMM – LSS, using a wavelet technique that is best suited for extended sources (see Pacaud et al. 2006).

4.1 Preliminary data preparation and cleaning

We used the *XMM – Newton* Science Analysis System (XMM – SAS) v. 5.4.1 to analyze observations G1 – G19, performed between July 2001 and January 2003, as summarized in Table 2.1. We adapted a pipeline developed by Baldi et al. (2002) for the HELLAS2XMM survey.

First, raw data provided to the observer have to be calibrated. Contrary to other missions, the *XMM – Newton* calibration database is updated continuously and does not have a version number. The Current Calibration File (CCF) contains information on all the *XMM – Newton* calibration files ever made public. To analyze data, one must build a CCF Index File, i.e. identify what calibration files are appropriate for the given observation and analysis dates. This must be done with the SAS tool `cifbuild`. We used it with the option *analysisdate* ="now" to pick up the latest CCF relevant to the original observation time, using the latest calibration set available at the time the procedure was run (July 2003).

The Observation Data Files (ODF) distributed to the observer contain a summary file, that however does not contain all the information required to process the ODF with the SAS. The XMM – SAS `odfingest` extends the summary file with data extracted from the instrument housekeeping data files and

the calibration database. It examines all files in the ODF directory and from those it reconstructs the structure of the observation in terms of exposures. For each exposure it determines the start and stop times.

We then used `epproc` and `emproc` tasks to produce linearized event files, for pn and MOS respectively.

The event files have then to be cleaned up from hot pixels and soft protons flares, both worsening data quality.

A hot pixel is a definitely damaged element, which consequently shows a permanently high signal, such that it is detected in every frame of a CCD, and is caused by CCD extra dark current generating states or other defects. For the X-ray cameras, such sites appear like isolated X-rays. Due to the requirement to examine data for events splitting between pixels, the hot pixel invalidates signals from the 8 surrounding pixels.
Occasionally, a hot pixel generates so much charge that it emits charge into every pixel within a column, making unusable every single pixel in the column. Tasks `epproc` and `emproc` provide a reliable identification of the location of bad pixels, flagging them with different numerical codes. Using `evselect` task with the $FLAG == 0$ condition allowed us to reject all bad pixels and events close to bad pixels.

Soft protons flares were described in subsection 3.1.3. We located them analyzing the light curves at energies higher than 10 keV, where the contribution from the X-ray source is negligible relative to the proton flux, in order to avoid contribution from real X-ray source variability. We fixed the threshold for good time intervals at 0.15 cts s^{-1} in the $10 - 12.4$ keV band for MOS and 0.35 cts s^{-1} in the $10 - 13$ keV band for pn. The use of a fixed threshold for soft protons ensures a greater uniformity in data reduction than a variable threshold. The soft protons contamination is highly variable. As an example, considering our observations, in G01 pointing less than 10% of exposure time had to be excluded, while for G02 pointing we had to exclude about 50% of exposure time and the whole G12 observation had to be rejected because almost completely affected by soft protons flares.

In order to exclude any residual contamination by spurious events, we used a conservative threshold on patterns, 0 for pn events and a ≤ 4 for MOS events (see subsection 3.1.4).

4.2 Source detection and characterization

4.2.1 Data preparation

The clean event files are used to generate MOS1, MOS2 and pn images in several energy bands: $0.3-0.5$ keV (A), $0.5-2$ keV (B), $2-4.5$ keV (C), $4.5-10$ keV (D), $2-10$ keV (CD) and $0.3-10$ keV (ABCD). All images are built up with a spatial binning of $4.35''$ per pixel, roughly matching the physical binning of the pn images ($4''$ pixels) and a factor of about 4 larger than that of MOS images ($1.1''$ pixels). In any case, the image binning does not significantly worsen *XMM – Newton* spatial resolution, which depends almost exclusively on the PSF.

The excellent relative astrometry between the three cameras (within $1.5''$ for all cameras and over the full field of view, well under the FWHM of the PSF, see Kirsch et al. 2004) allowed us to merge together the MOS and pn event files and to generate merged images in the energy bands listed above; source detection was performed on these images, in order to increase the signal to noise ratio of source and reach fainter X-ray fluxes.

A corresponding set of exposure maps is generated to account for spatial quantum efficiency, mirror vignetting and field of view of each instrument (see Chapter 3). SAS task `eexpmap` was used. It evaluates the above quantities assuming an event energy which corresponds to the mean of the energy boundaries. However, given that CD and D bands cover a wide range of energies, for exposure maps generation the energy limits for these bands were fixed to appropriate narrower values around 3.9 and 6.2 keV for pn and 3.6 and 5.8 keV for MOS.

Similarly to the X-ray images, merged exposure maps were created for each energy band.

4.2.2 Source detection

We run the detection algorithm on the five images from the A, B, C, D and CD energy bands. We did not perform detection in the total $0.3-10$ keV band and counts and fluxes reported in the database referring to this band are the sum of results in individual bands.

A preliminary source list was created running the SAS task `eboxdetect`, which scans the image and searches for sources accumulating counts from a 5×5 pixel window, computing the background in the surrounding 56 pixels (9×9 pixel window). We ran it in each band independently. Then we used the task

`esplinemap` to remove all sources in the list from the original merged image, thus creating a "cheesed image" (image with holes at the position of sources), and to create a background map. Next we ran `eboxdetect` again simultaneously on all images, using the background maps produced by `esplinemap` to estimate the background. We set the level of significance for source detection to a very low value, in order to avoid losing sources at this preliminary stage. We finally used the `emldetect` task, which performs a maximum likelihood fit to the source counts distributions and provides a best fit value of source position. We note that, although detection is performed in 5 different bands, we have an unique set of coordinates for each sources, as a result of `eboxdetect` running simultaneously on all energy bands.

4.2.3 Source characterization

In order to obtain background maps able to reproduce the local variations of the background, we corrected pixel by pixel the background maps obtained by task `esplinemap` in the following way. We measured counts in the cheesed image (cts_{ch}) and in the background map (cts_{bk}), within three times the radius corresponding to an encircled energy fraction of the PSF of 0.68 (see below) and multiplied the merged image created at the beginning of the data preparation phase (see subsection 4.2.1) by a correction factor given by the ratio $\mathrm{cts}_{ch}/\mathrm{cts}_{bk}$.

Source characterization was done using FORTRAN programs. First, for each source in each band we computed the total net counts and errors:

$$S = \frac{\mathrm{cts}_{img} - \mathrm{cts}_{bk}}{\alpha}, \qquad \sigma_S = \frac{1 + \sqrt{\mathrm{cts}_{img} + 0.75}}{\alpha} \tag{4.1}$$

where $\alpha = 0.68$, cts_{img} are the counts on merged images (source + background) and cts_{bk} are counts in the background map, computed within the radius $\mathrm{r}_{0.68}$, corresponding to an encircled energy fraction of the PSF of 0.68. The value of $\mathrm{r}_{0.68}$ is a function of position and ranges from $\sim 13.5''$ at the center of the field, to $\sim 20''$ at an off-axis angle of $14'$. It was estimated from a 4 – gaussian model for the PSF, as described in the `emldetect` documentation[1]. Errors were estimated assuming the approximation to Poisson noise (see Gehrels 1986). If in a given band net counts were negative, they were set to zero. Sources within 50 pixel from the image borders had net counts set to zero in each energy bands and were excluded from the list.

[1] `http://xmm.vilspa.esa.es/sas/current/doc/emldetect/node9.html`

Count rates were computed as

$$CR = \frac{S}{T_{MOS1} + T_{MOS2} + T_{pn}} \tag{4.2}$$

i.e. the ratio between net counts and the sum of exposure times of the three instruments, computed as the average of the values within $r_{0.68}$ at the source position, in the individual exposure maps.

The count rate - to - flux conversion factors were computed for each camera and each energy band using XSPEC (v. 11.3.1) from response matrices, generated using SAS tasks `rmfgen` and `arfgen` at the center of field, with our pattern selection (see Section 4.1). We assumed a simple power law spectral model with a photon index $\Gamma = 1.7$ and a galactic column density $N_H = 2.61 \times 10^{20}$ cm^{-2}, which is the average value in the XMDS fields direction (Dickey & Lockman 1990). The total conversion factors for the three cameras combined were calculated using the exposure times and the conversion factors of individual cameras, according to the formula

$$\frac{T_{tot}}{cf_{tot}} = \frac{T_{MOS1}}{cf_{MOS1}} + \frac{T_{MOS2}}{cf_{MOS2}} + \frac{T_{pn}}{cf_{pn}} \tag{4.3}$$

where $T_{tot} = T_{MOS1} + T_{MOS2} + T_{pn}$. The source flux is then

$$F_X = cf_{tot} \cdot CR. \tag{4.4}$$

The fact that a source may fall close to (or on) a inter-CCD gap or at the edge of the field of view is taken into account in the exposure maps, which are used to compute the rates and therefore the fluxes. This should be in general an acceptable approximation. When a source is outside the FOV of one of the cameras, the relative exposure time is zero and the fluxes are estimated from the other two cameras. Parameters that enter in the flux computation, such as source and background counts, exposures and so on, are average values within a circle of radius r_{68}. When a source is near a CCD gap, r_{68} will include both pixels inside and outside the gap, and therefore the gap effect will be smoothed. However, when a significant fraction of the source falls in a CCD gap, or sources are near (but not outside) the borders of the FOV, the fluxes will be more uncertain. In these cases a more careful, non automatic analysis

could be needed. To identify them, we assigned a numerical flag to each source, with the following meaning:

- 0: the source is free of gaps/borders;
- -1: the source region is outside the FOV in one (two) of the instruments, the camera(s) with zero exposure;
- 1: the source region may partially overlap a CCD gap or may be partially outside the FOV;
- 2: the center of the source is near/in a CCD gap/border.

Flag -1 is trivial to assign, since it only requires a zero exposure in one (or two) of the cameras. To automatically assign the other flags, we computed the ratios

$$M12 = \frac{|\frac{exp_{M1}}{exp_{M2}} - \frac{exp_{M1,max}}{exp_{M2,max}}|}{\frac{exp_{M1,max}}{exp_{M2,max}}} \tag{4.5}$$

$$M1P = \frac{|\frac{exp_{M1}}{exp_{pn}} - \frac{exp_{M1,max}}{exp_{pn,max}}|}{\frac{exp_{M1,max}}{exp_{pn,max}}} \tag{4.6}$$

$$M2P = \frac{|\frac{exp_{M2}}{exp_{pn}} - \frac{exp_{M2,max}}{exp_{pn,max}}|}{\frac{exp_{M2,max}}{exp_{pn,max}}} \tag{4.7}$$

where $exp_{M1(M2)(pn)}$ is the value of exposure map (in the B band) at the source position for the MOS1 (MOS2) (PN) camera, and $exp_{M1(M2)(pn),max}$ is the maximum value of exposure map for the observation in the same camera.

Sources free of gaps (flag 0) should have values of M12, M1P and M2P close to zero, but values up to 0.15 are acceptable (this takes into account different efficiencies of the instruments at large off-axis angles). Above this value the contamination from CCD gaps is increasingly severe. We estimate that when at least one of the ratios $M12, M1P, M2P > 0.24$, the source is in a CCD gap (flag 2). Values between 0.15 and 0.24 are indicative of some contamination (flag 1), although the degree of contamination is not directly related to the values of M12, M1P and M2P.

For each energy band we computed the probability p that counts originate from a background fluctuation, using the Poisson's formula

$$\sum_{n=cts_{img}}^{\infty} e^{-cts_{bk}} \frac{cts_{bk}^{n}}{n!} > p \tag{4.8}$$

where cts_{img} and cts_{bk} have the same meaning as in Eq. (4.1). We set a threshold $p = 2 \times 10^{-4}$ below which we considered sources for our final catalogue. We found 1322 X-ray sources with $p < 2 \times 10^{-4}$ in *at least one energy band*. For these we computed source parameters (net counts, count rates, fluxes, etc) for all energy band. Since source detection and characterization were performed in each field independently, these 1322 sources include multiple detections in overlapping regions. Multiple detections of the same source were recognized only a posteriori (see Chapter 5).

Like all other source parameters, hardness ratios (i.e. ratios between count rates in different energy bands) are computed from MOS1, MOS2 and pn combined images; we verified that they are consistent with those computed from single camera images. In Fig. 4.1 and 4.2 we show the hardness ratios HR_{cb} and HR_{dc}, defined as

$$\mathrm{HR}_{cb} = \frac{CR_{2-4.5} - CR_{0.5-2}}{CR_{2-4.5} + CR_{0.5-2}} \tag{4.9}$$

$$\mathrm{HR}_{dc} = \frac{CR_{4.5-10} - CR_{2-4.5}}{CR_{4.5-10} + CR_{2-4.5}} \tag{4.10}$$

where CR are the count rates in the given energy band as defined by Eq. (4.2), computed from the merged images, as a function of those computed from single camera images, for sources in the G01 field. The agreement is good, in particular for HR_{cb} and for sources with a high number of counts. We concluded that we can use the hardness ratios computed on count rates from the three cameras combined.

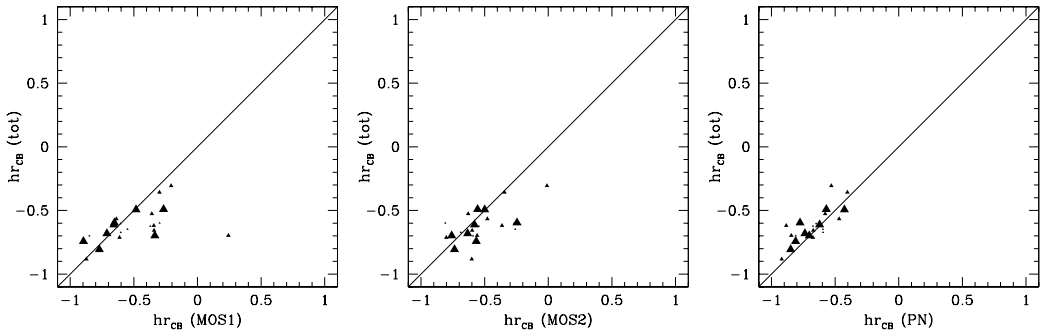

Figure 4.1: Hardness ratio between C and B bands computed from the merging of the three cameras vs that computed from MOS1 (left panel), from MOS2 (middle panel) and from pn cameras (right panel) for sources of G01 field. Symbol size is proportional to net counts of the source.

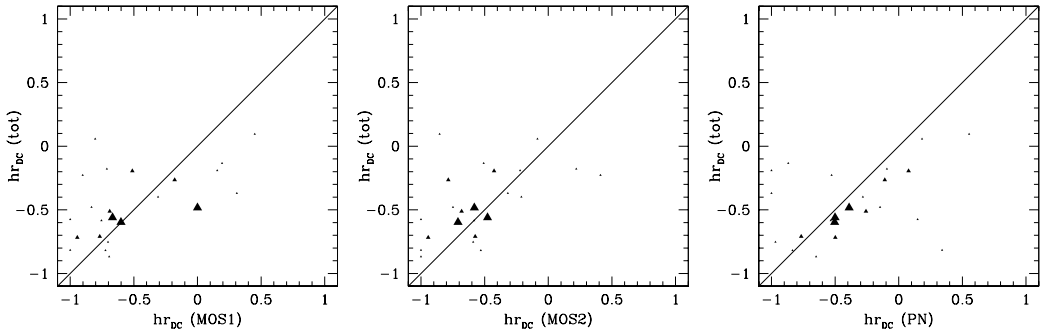

Figure 4.2: Hardness ratio between D and C bands computed from the merging of the three cameras vs that computed from MOS1 (left panel), from MOS2 (middle panel) and from pn (right panel) for sources of G01 field. Symbol size is proportional to net counts of the source.

Chapter 5

The identification procedure

We describe here the semi automatic procedure developed to associate one optical and/or infrared counterpart to each X-ray source.

Since the fields of view of adjacent *XMM – Newton* pointings in the XMDS overlap, the same source could be detected in more than one field (up to four, see subsection 4.2.3). We have estimated first a) the minimum and b) the maximum distances to use as thresholds to examinate detections in overlapping fields:

a. After inspection of the distribution of distances between the X-ray positions of pairs of sources in adjacent fields, we decided to automatically consider as multiple detections of the same source all detections in different pointings with X-ray positions closer than $6''$.

b. Since there are in the survey only two pairs of sources detected in the same field that are closer than $18''$, this was considered as the maximum distance between possible multiple detections.

Between $6''$ and $18''$, we examined all the 26 pairs found, using X-ray images and optical finding charts (see Section 2.3) to check if the different detections could be associated to the same optical objects. We retained only one of the detections in 5 cases, that correspond to X-ray sources detected in three different fields, where, for example, the distance between the source 1, detected in field A, and source 2, detected in field B, is $< 6''$, and also the distance between source 2 and source 3, detected in field C, is $< 6''$, but the distance between source 1 and source 3 is $> 6''$. In the other 21 cases, each X-ray detection was considered as an independent source.

Among the multiple detections, we chose as "best" detection that with the best combination of S/N ratio, count rate, flux, number of counts and detection

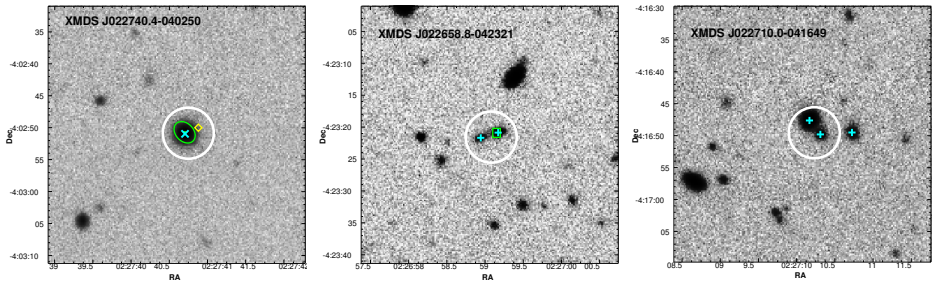

Figure 5.1: Examples from our identification procedure: some representative I band finding charts (size $40'' \times 40''$) with overlays of a circle of $4''$ radius centered on the X-ray position (white thick circle; the distance between the X-ray source and the identified counterpart is $< 4''$ in more than 90% of cases, see text and Fig. 5.2), the positions of all optical sources within $6''$ (cyan X's and crosses respectively for point-like and possibly extended objects), the positions of NED catalogue objects (yellow diamonds) and the radio source error box (green rectangles) or extent (green ellipses). Three cases are shown: an unique counterpart, an identification preferring a radio source, an ambiguous identification.

probability. We also checked that the chosen X-ray detection is within the field of view of all the EPIC cameras and verified the flux consistency of the multiple detections. We do not detect any significant flux variation in the multiply detected sources with the possible exception of three, which are however close to inter-CCD gaps. Of the 1322 X-ray detections, 1147 are independent X-ray sources.

A first identification work was made on a sample of relatively bright X-ray sources, which in several cases should have a obvious optical counterpart. In order to obtain a sufficiently large sample of non spurious sources, we selected the X-ray sources detected with a signal to noise ratio[1] larger than 4, in at least one of the energy bands A, B, C, D or CD defined in subsection 4.2.1, and lying in the area covered by the VVDS photometry (see subsection 2.2.1).

We positioned the X-ray source onto the VVDS optical finding charts (see Section 2.3) and for each of them inspected all optical objects within a radius of $6''$ from the X-ray position. Examples of finding charts used in our identification procedure are shown in Fig. 5.1. A $6''$ radius is considerably larger than the nominal SAS (`emldetect`) position error combined with the $2''$ *XMM – Newton* estimated astrometrical uncertainty for $> 99\%$ of our sources, but it also takes into account possible astrometrical misalignements and gives a larger set of candidate identifications for future refinements. It is also consistent with the values chosen by other authors (e.g. Waskett et al. 2004).

[1] S/N $= S/\sigma_S$ where net counts S and their error σ_S are defined in Eq. (4.1).

We used the following criteria for optical identifications:

a. unique optical counterpart (see example in the left panel of Fig. 5.1);

b. closest and brightest counterpart;

c. no optical counterpart down to $R_{AB} \sim 25.3$, the magnitude limit of McCracken et al. (2003).

The presence of a radio counterpart was used as a preference criterion (see example in the middle panel of Fig. 5.1). Associations with radio sources are relatively few and were evaluated by visual inspection.

When we were not able to assign an unambiguous optical counterpart based on the criteria listed above (see example in Fig. 5.1, right panel), all possible optical counterparts were retained.

After a first pass with this procedure, we found evidence in some X-ray fields of a systematic rigid shift between the position of the X-ray sources and their counterparts. We then used the best identified sources (essentially cases a and the best cases b) to correct the astrometry of the X-ray observations. The SAS task `eposcorr` was used to compute for each *XMM – Newton* field a rigid shift (as high as $3''$ in G13 field) in both right ascension and declination. Since at this stage only VVDS optical data were available for identifications, the correction was applied only to the fields covered by the VVDS photometry (G01, G02, G03, G04, G05, G06, G07, G08, G10, G11 and G13). No rotational correction was required.

After the astrometrical correction, we revised the identifications, considering again all optical objects within a $6''$ radius from the X-ray position. Of the 286 X-ray sources in the sample, 233 (i.e. $\sim 83\%$) were identified, while 3 are optically blank fields (no optical counterparts down to $R_{AB} \sim 25.3$). The remaining cases did not allow us to assign an unambiguous optical counterpart using the criteria listed above. 93% of the optical counterparts of the identified sources were within a $2''$ radius from the X-ray source and 99% within $4''$. We therefore concluded that, after astrometric correction have been applied, the search radius for optical counterparts can safely be reduced to $4''$. We also verified that there is no correlation between the X-ray to optical distance and the off-axis position in the field of view, while there is a mild correlation with count rate, in the sense that sources with a large X-ray to optical separation are among the weakest. This is not surprising, given that a correlation exists between X-ray counts and X-ray positional errors, in the sense that sources

with few X-ray counts have on average a greater error on X-ray position than those with a larger number of counts. The Catalogue of optical identifications of these sources (the 4 σ VVDS Catalogue), together with X-ray and optical properties of the sources, was presented in Paper I.

As a final step, we computed the probability of chance coincidence between the X-ray source and the optical candidates within the given radius, according to the equation

$$P = 1 - exp(-\pi\ n(< m)\ r^2) \tag{5.1}$$

(Downes et al. 1986), where r is the distance between the X-ray source and the optical candidate, and $n(< m)$ is the density of optical objects having I magnitudes brighter than m, computed using the full VVDS Catalogue (McCracken et al. 2003). A $P < 0.01$ criterion, corresponding e.g. to the probability of finding a $I = 21$ object at $2''$, applied to the X-ray/optical pairs produced a list of identifications very similar to our visually identified sources. About 90% of our identified sources have $P < 0.01$, while only 21% of the ambiguous cases have $P < 0.01$. We therefore decided to use the probability criterion to obtain a semi automatic identification procedure. This was applied to the whole XMDS and in particular to identify sources in the 3 σ hard sample, which has been used to study the multiwavelength properties of AGN (see Chapter 7).

After the publication of the 4 σ VVDS Catalogue, optical CFHTLS and infrared SWIRE data (see Section 2.2) became available, so we used them in addition to VVDS data to identify all X-ray sources in the XMDS. Since we do not have access to the whole VVDS and CFHTLS catalogues and images, but we only have positions and photometric data for optical sources within a fixed radius from the X-ray positions, we made use of our database to associate to each X-ray source all combinations of optical and IR objects in the catalogues considered within a search radius of $6''$. Optical objects in the VVDS and CFHTLS catalogues are matched only a posteriori. The same is true for infrared SWIRE objects.

We computed the probability of chance coincidence between an X-ray source and all optical VVDS, optical CFHTLS and infrared SWIRE candidates within a search radius of $6''$ using the equation (5.1), where r is now the distance between the X-ray source and the proposed counterpart (with a lower value fixed at $2''$, which roughly corresponds to the *XMM – Newton* astrometrical uncertainty). To compute $n(< m)$ we used I magnitudes for VVDS sources

and i' magnitudes for CFHTLS objects (from D1 where available). We used the density $n(> F_{3.6})$ for infrared candidate counterparts. For each candidate counterpart there are therefore from 1 to 3 values of P, depending if the object is detected in the VVDS, CFHTLS and SWIRE. We classified the probabilities as "good" ($P < 0.01$), "fair" ($0.01 < P < 0.03$) or otherwise "bad" and took as identification the object with the best probability combination. All tentative identifications were then checked by visual inspection using the VVDS finding charts (or DSS-II IR images obtained from ESO outside the VVDS area). The probability criterion allows us to always prefer a counterpart, however in some cases the probabilities of two or more candidates are very similar; these cases were considered as ambiguous.

Again, we used the identified sources to compute the astrometrical correction to the X-ray positions. Since positions in fields covered by the VVDS photometry were already corrected in the previous step, we checked that the results obtained using the new optical/IR identifications were consistent with the previous ones and we retained the corrected coordinates obtained from the 4 σ VVDS Catalogue. The corrections for all XMDS fields are reported in Table 5.1. After the application of the astrometrical correction, all probabilities were recomputed. The identifications changed only for a limited number of cases, for which the visual inspection was repeated.

Fig. 5.2 shows the angular separation between the position of the identified optical counterparts and that of the X-ray sources in the whole XMDS after astrometric correction. About 92% of the optical counterparts are within a $4''$ radius from the X-ray source, essentially confirming the results obtained from the 4 σ VVDS Catalogue.

As in the case of the preliminary work made on the 4 σ VVDS sample, associations with radio sources were evaluated by visual inspection. We also flagged candidate or confirmed galaxy clusters.

Field	ΔRA (″)	ΔDEC (″)
G01	−1.60	0.00
G02	0.00	−0.53
G03	−0.53	1.07
G04	−1.60	0.00
G05	0.00	0.00
G06	0.00	0.53
G07	−0.53	−0.53
G08	0.00	0.00
G09	1.07	0.53
G10	−0.54	0.53
G11	0.00	0.53
G13	−2.67	−2.13
G14	1.60	1.07
G15	−1.60	−2.13
G16b	0.53	0.00
G17	−2.13	−1.60
G18	−2.67	−0.53
G19	−3.73	0

Table 5.1: Astrometric correction applied to *XMM – Newton* observations using reliable optical identifications. Field G16a has not been corrected since it contains only "duplicated" sources from G16b, which are detected with a better statistics.

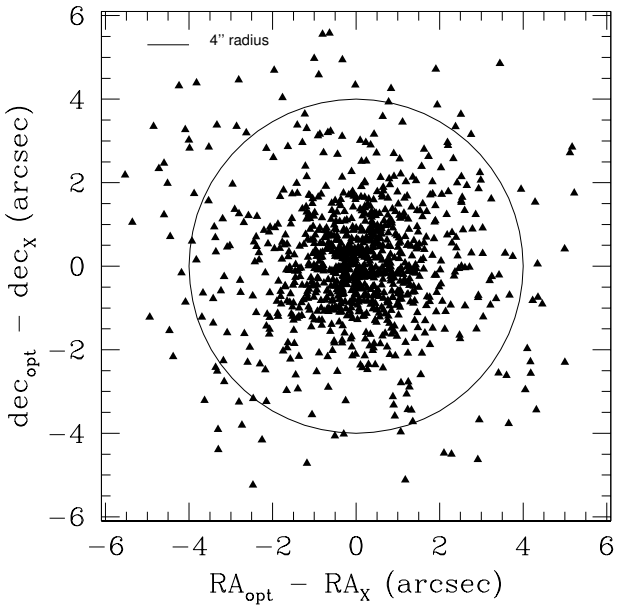

Figure 5.2: Distance in RA and DEC between the X-ray source position (inclusive of astrometric correction) and the optical counterpart position. The fiducial radius of $4''$ shown includes $\sim 92\%$ of objects (see text).

Part III

Results

Chapter 6

The logN-logS relationship

The integral number-count or logN-logS relationship gives, for each value of flux F, the surface density of sources detected at flux $> F$. The determination of the logN-logS is essential to study for example the nature of X-ray background, the source evolution and their distribution in space.

Based on deep surveys with *Chandra* and *XMM - Newton*, number-count relationships have now been determined down to $0.5-2$, $2-8$ and $5-10$ keV fluxes of about 2.3×10^{-17}, 2.0×10^{-16} and 1.2×10^{-15} erg cm^{-2} s^{-1}, respectively (e.g. Brandt et al. 2001; Hasinger et al. 2001; Cowie et al. 2002; Rosati et al. 2002; Moretti et al. 2003; Bauer et al. 2004). These surveys have now resolved about 90% of the XRB in the $0.5-2$ keV band into discrete sources (e.g. Moretti et al. 2003; Bauer et al. 2004; Worsley et al. 2005). Above 2 keV the fraction of resolved sources varies from $\sim 80-90\%$ between 2 and 6 keV and $\sim 50-70\%$ between 6 and 10 keV (see also Sec. 1.3).

At the deepest flux within the XMDS ($\sim 10^{-15}$ erg cm^{-2} s^{-1} in the $0.5-2$ keV band and $\sim 7\times10^{-15}$ erg cm^{-2} s^{-1} in the $2-10$ keV band, see Section 6.1) the logN-logS is therefore well determined both in the soft and in the hard band. However the survey properties make it suitable to obtain information on, e.g., cosmic variance. In fact, contrary to most of surveys of comparable depth, such as the HELLAS2XMM, the XMDS is made of contiguous pointings, thus sampling a specific part of the sky. Moreover, it covers a much larger area with respect to deep, pencil beam surveys like the *Chandra* Deep Fields (Giacconi et al. 2002; Alexander et al. 2003), or the Lockman Hole (Hasinger 2004), therefore it should provide a larger number of sources at higher fluxes. In addition, the computation of the logN-logS is an useful test to check the efficiency of our detection procedure, in particular with respect to the HELLAS2XMM, whose pipeline and flux range are similar to ours.

6.1 Flux limit computation

To compute the surface density of X-ray sources detected at fluxes greater than a given value, one must know the sky area in which a source with a given flux can be observed. The curve of this area as a function of flux is called sky coverage. The flux limit is related to the sky coverage and is defined as the faintest flux at which a source can be detected above the local background. In a single X-ray observation the faintest observable flux is not a constant, but it depends on a number of factors, such as the exposure time, the position of the source in the field of view, the spectrum of the source and the background. Moreover, in a survey like the XMDS, each field has a different exposure time. As a consequence, the flux limit must be determined in each point of each X-ray observation.

The computation of the flux limit was done using a FORTRAN procedure that generates, for each observation and energy band, a map, which gives the value of flux limit as a function of position (x,y) in the merged images (see subsection 4.2.1). It requires the exposure maps of each instrument, the corrected background maps for the merged images and a model for the PSF. We used the 4 – gaussian model already mentioned in subsection 4.2.2. The procedure evaluates at each image pixel (x,y) the total background counts B (from the corrected background map), within a radius r_{68}, and the mean exposure times T_{MOS1}, T_{MOS2} and T_{pn} (from the relative exposure maps). From the value of the background it computes the minimum total counts S (source + background) necessary for a source to be detected at a probability p, using the formula

$$\sum_{n=S}^{\infty} e^{-B} \frac{B^n}{n!} > p. \tag{6.1}$$

p is the poissonian probability that counts originate from a background fluctuation. For the logN-logS determination, we chose $p = 2 \times 10^{-5}$, which is well above our acceptance threshold for sources ($p = 2 \times 10^{-4}$), ensuring very few spurious sources in the sample while giving us a large dataset of objects. Given a detection probability threshold p, the number of expected spurious sources can be estimated by multiplying p by the number of independent (not overlapping) detection cells. In our detection procedure we used circular detection cells with variable radii, depending on the PSF size (see subsection 4.2.3), therefore the area covered by a detection cell ranges from 0.16 to 0.35 arcmin^2. Taking a

mean value of 0.25 arcmin^2 and given that the survey area obtained considering all *XMM – Newton* fields as independent areas (see below) is ~ 3.48 deg^2, the number of independent detection cell is $\sim 5 \times 10^4$. We therefore expect to have ~ 10 spurious sources in the whole survey area at $p = 2 \times 10^{-4}$ and ~ 1 spurious source at $p = 2 \times 10^{-5}$ (corresponding to 0.1% of total number of sources in the $0.5 - 2$ keV band and 0.3% of total sources in the $2 - 10$ keV band).

The minimum count rate is computed by dividing the minimum counts, background subtracted and PSF corrected, by the mean exposure time:

$$CR = \frac{(S - B)/\alpha}{T_{MOS1} + T_{MOS2} + T_{pn}}. \tag{6.2}$$

The flux limit is then obtained from the count rate – to – flux conversion factor computed in Eq. (4.3):

$$F_{lim}(x, y) = cf \cdot CR. \tag{6.3}$$

From flux limit maps we computed the sky coverage for the single fields. The sky coverage of the whole survey is the sum of those of single fields, that were considered as independent areas, consistently with our detection procedure. The XMDS sky coverage is shown in Fig. 6.1 for the $0.5 - 2$ and $2 - 10$ keV bands. Our faintest flux is $\sim 10^{-15}$ erg cm^{-2} s^{-1} in the $0.5-2$ keV band and $\sim 7\times10^{-15}$ erg cm^{-2} s^{-1} in the $2 - 10$ keV band.

6.2 The cumulative and differential logN-logS

We computed the logN-logS distribution in the $0.5 - 2$ and $2 - 10$ keV bands, both for single fields and for the whole survey. In combining the different observations, we included multiple detections of the same source in overlapping fields because we considered all fields as independent areas. There are 1028 X-ray sources detected at $p < 2 \times 10^{-5}$ in the $0.5 - 2$ keV band and 328 in the $2 - 10$ keV band.

Fig 6.2 shows the comparison between the cumulative logN-logS computed for individual fields and that of the whole survey: there is a good agreement between the logN-logS obtained in each field and that from the whole area, excluding the brightest and the faintest fluxes. At the highest fluxes the number of sources is small and the sky coverage value approaches the geometrical area

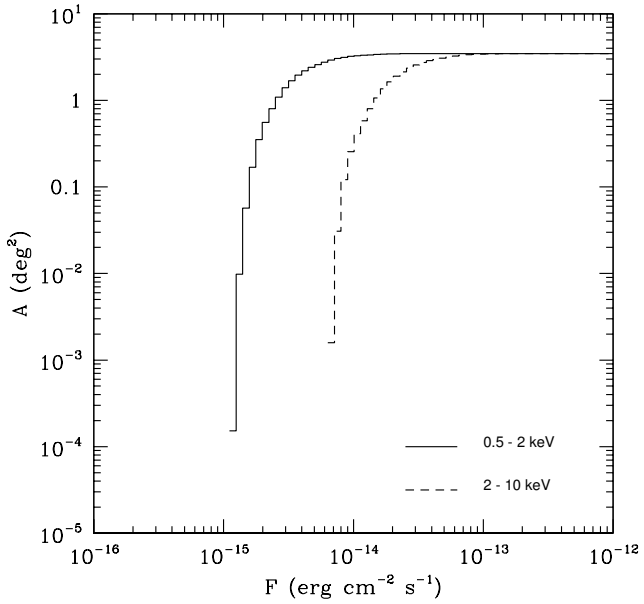

Figure 6.1: Sky coverage for sources detected at $p < 2 \times 10^{-5}$ in the $0.5 - 2$ keV band (solid line) and in the $2 - 10$ keV band (dashed line) computed considering all fields independently.

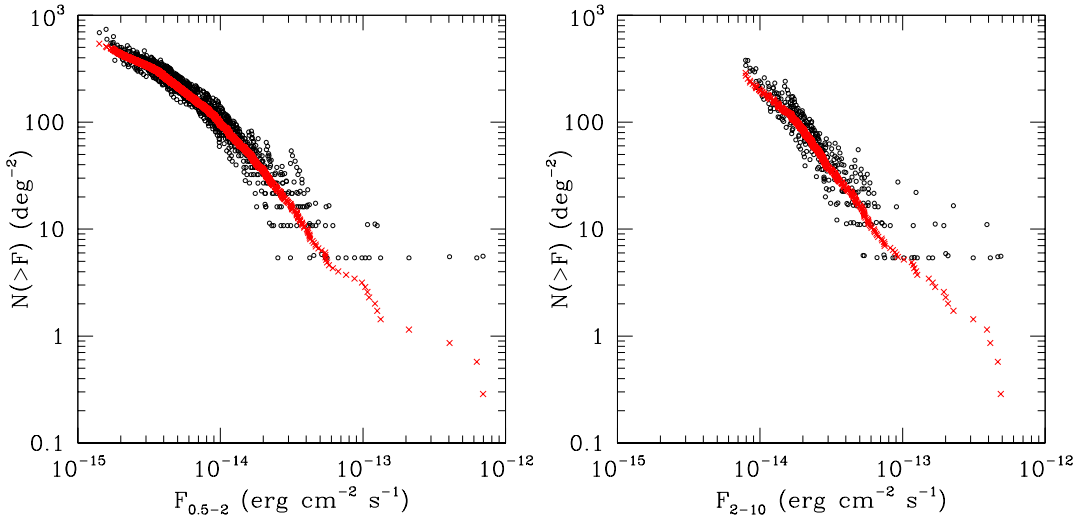

Figure 6.2: The cumulative logN-logS distribution for the whole survey (red crosses) compared with those of single fields (empty circles), for the $0.5 - 2$ keV band (left panel) and for the $2 - 10$ keV band (right panel).

of the field of view. The difference at the faintest fluxes is instead due to the different depth achieved in the different fields. As an example, in the $0.5-2$ keV band, the minimum flux at which a source is detected is 1.4×10^{-15} erg cm^{-2} s^{-1}, and the surface density computed from the whole survey is 543 sources deg^{-2}. In practice, sources at this flux are detected only in the G13 field, and at this flux we would obtain 687 sources deg^{-2} if only this field were considered. This happens because the area covered in the G13 field at $F = 1.4 \times 10^{-15}$ erg cm^{-2} s^{-1} is 0.005 deg^{-2}, but the sky coverage computed from the whole survey takes into account also the area in other fields in which a source with that flux would be observable, even if no sources have been detected. In fact, the area covered in the whole XMDS at $F = 1.4 \times 10^{-15}$ erg cm^{-2} s^{-1} is 0.03 deg^{-2}, a factor of 6 greater than that covered in G13 alone. The same is true for the $2-10$ keV band.

The shape of the cumulative logN-logS is clearly curved in both bands and cannot be represented by a single power law. A fit to the cumulative distribution does not allow a meaningful computation of confidence limits on the parameters, because points and errors are not independent (Crawford et al. 1970; Murdoch et al. 1973). Therefore we computed the differential logN-logS by binning (in equal bins in logarithmic space) the number N(F) of sources with flux F into flux bins of width ΔF_i (i.e. between fluxes F_{jmin} and F_{jmax}), then computing the average sky coverage A_i in the bin. The i-th bin of the differential curve $n(F)$ is given by

$$n(F)_i = \sum_{F_{jmin}}^{F_{jmax}} \frac{\mathrm{N}(F_j)}{\Delta F_i A_i}. \tag{6.4}$$

The plots of cumulative and differential logN-logS are shown in Fig 6.3, both for the soft (upper panels) and the hard bands (lower panels). A Poissonian error on the number of sources is assigned to each bin of the differential curves. The differential plots confirm that a single power law does not give a good fit. Therefore we used a broken power law.

For the $0.5-2$ keV band, the best fit is

$$n(F) = \begin{array}{ll} 6.515 \times 10^3 \times F_{15}^{-2.62} & F_{15} > 10.58 \\ 384.2 \times F_{15}^{-1.42} & F_{15} < 10.58. \end{array}$$

All fluxes F_{15} are normalized to 10^{-15} erg cm^{-2} s^{-1}. 90% confidence limits on slopes are $2.62^{+0.25}_{-0.22}$ and $1.42^{+0.14}_{-0.15}$, while the break position is at $1.06^{+0.30}_{-0.22} \times 10^{-14}$

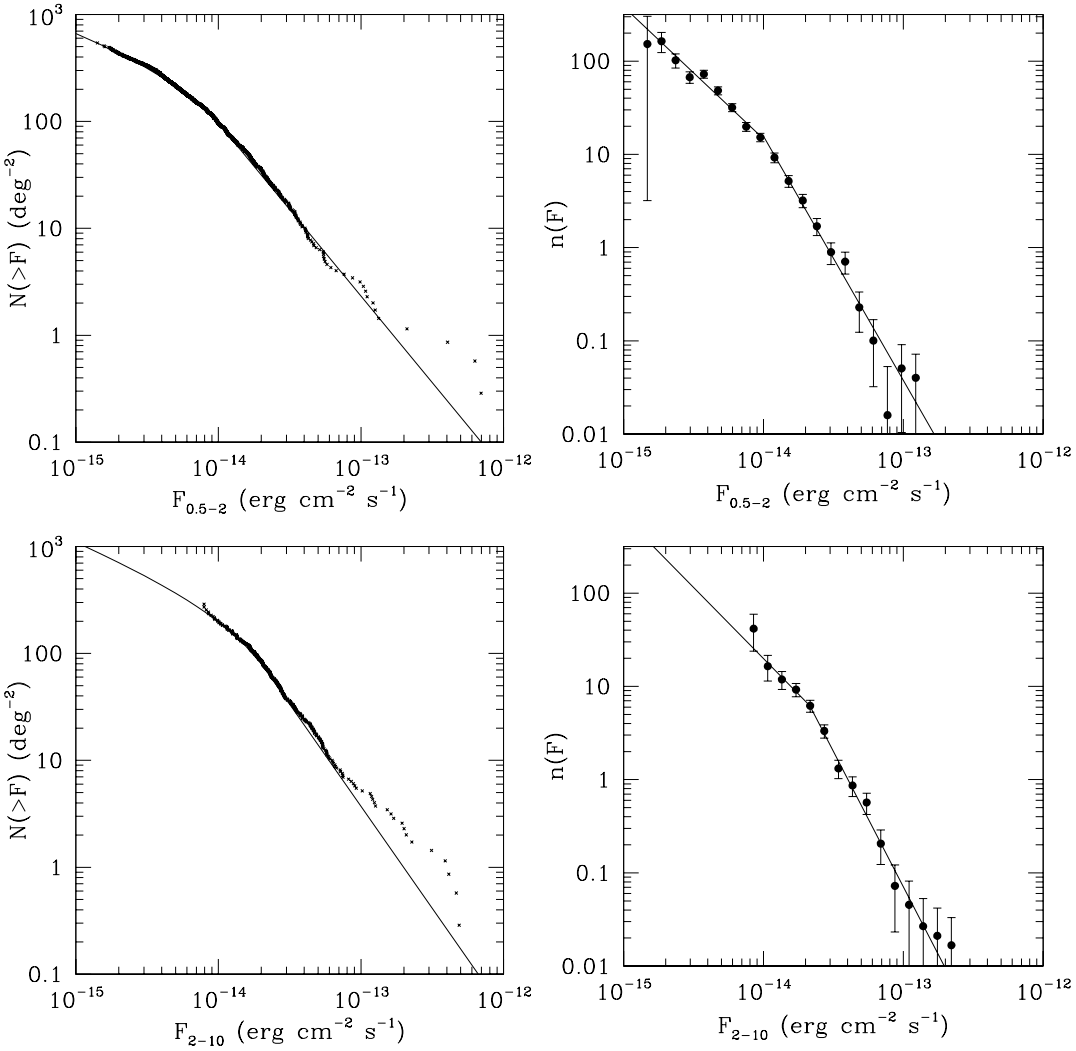

Figure 6.3: LogN-logS of sources *detected at* $p < 2 \times 10^{-5}$ in the $0.5 - 2$ keV band in the cumulative (upper left panel) and differential (upper right panel) form and the same in $2 - 10$ keV band (lower left and right panels). The unit of n(F) is number per 10^{-15} erg cm^{-2} s^{-1} . Our best fits are reported as solid lines on the differential plots and have also been converted to the cumulative form.

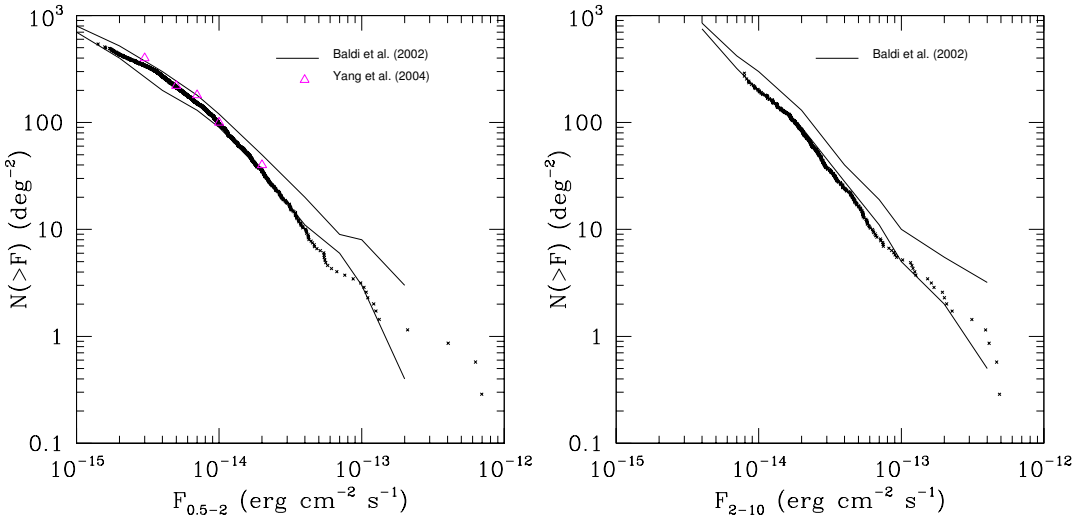

Figure 6.4: Comparison between our cumulative logN-logS (crosses) and that of Baldi et al. (2002) (solid line), in the soft (left panel) and hard band (right panel). In the left panel some points obtained from the logN-logS of the CLASXS survey (Yang et al. 2004) are also plotted (empty triangles).

erg cm^{-2} s^{-1}.

For the $2-10$ keV band we find

$$n(F) = 4.483 \times 10^4 \times F_{15}^{-2.91}$$

or $F_{15} > 21.4$, with 90% errors on slope $2.91^{+0.45}_{-0.30}$ and break $2.14^{+0.81}_{-0.54} \times 10^{-14}$ erg cm^{-2} s^{-1}. At lower fluxes the slope is not well constrained: the best fit is 1.53, but the confidence interval ranges between 0.37 and 2.04.

In Chapter 11 we will use the logN-logS computed here to estimate the surface density of different kinds of AGN, such as optically obscured and unobscured AGN and type 2 QSOs.

6.3 Comparison with the literature

Since our probability threshold $p < 2 \times 10^{-5}$ is one of those used by Baldi et al. (2002) in the HELLAS2XMM, our procedure is derived from theirs and the flux ranges are very similar, as noted before, our logN-logS should in principle be almost identical to the HELLAS2XMM ones. In Fig. 6.4 we compare our points with their upper and lower limits to the logN-logS, for the soft (left panel) and hard bands (right panel).

In the soft band we find consistency excluding the flux range $\sim 3\times10^{-14}- \sim 10^{-13}$ erg cm^{-2} s^{-1}, where our points are below the HELLAS2XMM lower envelop. In the hard band our logN-logS has a similar slope but a slightly lower normalization than that of Baldi et al. (2002). However, taking into account the purely statistical error on the number of sources, we are consistent with the Baldi et al. (2002) relationship in both the energy bands.

The Baldi et al. (2002) data are also used by Moretti et al. (2003), who combine data from six different surveys from *ROSAT, Chandra* and *XMM - Newton*, obtaining a logN-logS in the flux range $2.4 \times 10^{-17} - 10^{-11}$ erg cm^{-2} s^{-1} in the $0.5 - 2$ keV band and $2.1 \times 10^{-16} - 8 \times 10^{-12}$ erg cm^{-2} s^{-1} in the $2 - 10$ keV band. In the flux range common to the XMDS ($10^{-15} - 10^{-13}$ erg cm^{-2} s^{-1}) Moretti et al. (2003) use data from the HELLAS2XMM, therefore we are in agreement also with the Moretti et al. (2003) estimates.

We compared our results also with those of other surveys of similar depth, such as the *Chandra* Large Synoptic X-ray Survey (CLASXS, Yang et al. 2004) and the Serendipitous Extragalactic X-ray Source Identification (SEXSI, Harrison et al. 2003) program. Yang et al. (2004) give both integral and differential plots, while Harrison et al. (2003) only show the differential curve. Given the uncertainties in the fits, we prefer the comparison with the actual data where possible.

For the soft band, no plot is given in Harrison et al. (2003), while Yang et al. (2004) give both integral and differential curves. In the left panel of Fig. 6.4 our integral logN-logS is compared also with the Yang et al. (2004) points, and a good agreement is found.

For the hard band, the comparison between ours and the Harrison et al. (2003) differential relationships is shown in Fig. 6.5. The Harrison et al. (2003) points are generally higher, but consistent with ours, within errors.

Yang et al. (2004) use the $2 - 8$ keV band in CLASXS. Converting their fluxes in the $2 - 10$ keV band, we find that our points are systematically lower than theirs. This is not surprising, given that Yang et al. (2004) find that their total counts at $F_{2-8} \sim 10^{-14}$ erg cm^{-2} s^{-1} are $\sim 70\%$ higher than those of Moretti et al. (2003), who use Baldi et al. (2002) data for the flux range we are interested in.

The sky location of the XMDS has been intentionally chosen in order to avoid known bright X-ray sources and this could therefore explain, at least partially, the low density observed in our survey for fluxes above a few 10^{-14} erg cm^{-2} s^{-1}. On the other hand, Yang et al. (2004) interpret their overdensity as an indication

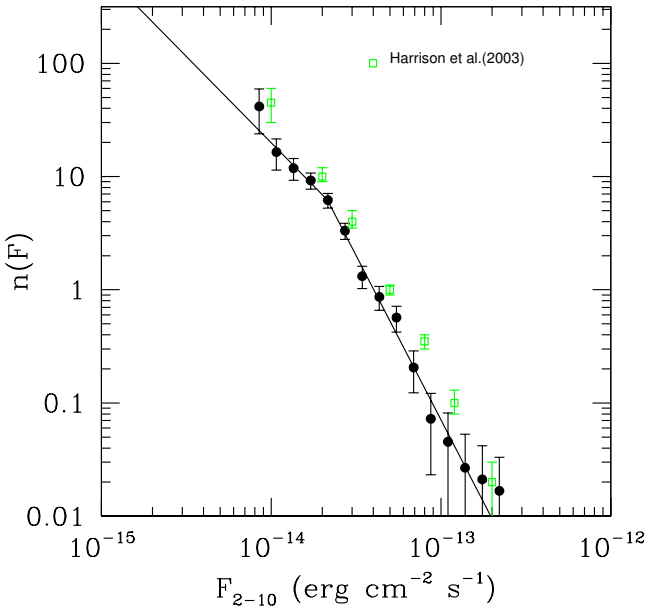

Figure 6.5: Comparison between or differential logN-logS (solid circles, the solid line is our best fit) and that of the SEXSI survey (Harrison et al. 2003, empty squares).

of an underlying large scale structure. We note that the CLASXS, like the XMDS, is constructed on contiguous pointings, while the HELLAS2XMM and the SEXSI are serendipitous surveys; it seems reasonable that the number count difference we find between the different surveys is caused by cosmic variance.

Recently, Gandhi et al. (2006) have computed the logN-logS relationship for 48 *XMM – Newton* pointings in the XMM - LSS region, including the 18 fields observed as part of the XMDS. They use a completely different detection pipeline, based on the wavelet technique (see Pacaud et al. 2006) and select only point-like sources detected with a signal to noise ratio greater than 3 in the soft or in the hard bands. In order to avoid problems due to multiple detections of the same source in adjacent pointings, they only consider sources that lay within $10'$ of the optical axis center of each pointing. They find excellent agreement with the XMDS logN-logS both in the soft and in the hard band. This supports our hypothesis that the lower surface density observed in our survey with respect to those cited above is due to the paucity of sources in the sky region chosen and not to pipeline systematics.

Our logN-logS can also be compared with that obtained from the two *Chandra* Deep Fields (CDFs) combined (Bauer et al. 2004): even if the flux limits

in these deep observations are at least two orders of magnitude lower than ours in both the soft and hard band, their cumulative logN-logS also cover the flux range $10^{15} - 10^{-13}$ erg cm^{-2} s^{-1}.

We find a good agreement with the Bauer et al. (2004) logN-logS in essentially the whole flux range common to the two surveys for the soft band, while our surface density is lower by a factor of ~ 2 in the hard band (we converted the CDFs $2 - 8$ keV fluxes in the $2 - 10$ keV band). On the other hand, given the small area covered (~ 0.2 deg^2 if the two CDFs are considered together), the number of sources detected at fluxes $> 10^{-14}$ erg cm^{-2} s^{-1}in the CDFs is small in both bands (~ 70 in the hard band and ~ 20 in the soft band; for comparison, in the XMDS ~ 300 X-ray sources are detected at $F > 10^{-14}$ in both soft and hard bands) and therefore errors affecting the Bauer et al. (2004) logN-logS at these fluxes are larger than ours. Moreover, the logN-logs relationship in the hard band is steep in the flux range we are interested in, so that a small difference in flux, due, for example, to different conversion factors used to compute fluxes, corresponds to a large variation in $N(> F)$. We therefore conclude that the difference observed between the XMDS and CDFs logN-logS in the hard band is not highly significant and could likely be ascribed to cosmic variance.

Chapter 7

The 3 σ hard sample

From the catalogue of the 1322 X-ray sources detected in the XMDS (see Chapter 4), a number of samples can be extracted, with which different aspects of the properties of X-ray sources can be studied. As already discussed in Chapter 5, we first selected sources detected with a signal to noise ratio > 4 in at least one of the five energy bands considered. This sample of relatively bright sources was used to test our identification procedure. We also selected two samples of sources with a probability of false detection $p < 2 \times 10^{-5}$ in the $0.5 - 2$ and $2 - 10$ keV bands, used to compute the logN-logS relationships (see Chapter 6). In this and the following Chapters we will concentrate on the properties of X-ray absorption in AGN. For this analysis, we selected a sample based on detections with a S/N threshold ≥ 3 in the $2 - 10$ keV band only. We considered only the area covered by the VVDS photometry, where data from CFHLTS, UKIDSS and SWIRE surveys are also available. This sample (hereafter the 3 σ hard sample) consists of 136 X-ray sources detected over an area of ~ 1 deg^2. We present here the results of optical and IR identifications on the 3 σ hard sample and their X-ray, optical and IR properties.

7.1 Sample composition

In Chapter 5 we described the procedure used to associate to each X-ray source an optical and/or IR counterpart. The results obtained with this procedure applied to the 3 σ hard sample are the following:

- Secure optical counterparts were found for 123 of 136 X-ray sources (90%). All of these within the SWIRE area are also detected in the IR. In a few cases, we actually used the IR detection to resolve ambiguities among

the possible optical counterparts. 12 of the 136 X-ray sources are instead outside the area covered by SWIRE.

- For 10 X-ray sources there are two or more optical objects within the search radius. Neither the probability criterion and visual inspection nor the IR detections allowed us to unambiguously identify the optical counterpart. In 6 cases, however, the optical candidates had similar magnitudes and colors. Since objects were classified on the basis of optical and infrared colors and SEDs (see below), these uncertain identifications were retained together with identified sources in most aspects of the work. In the other 4 cases, the candidate optical counterparts had different optical colors; these sources were dismissed since we could not use even the color information (see Section 7.3).

- The 3 remaining sources have no optical counterpart down to $R_{AB} = 25.3$ within the search radius. They are however detected in the IR. We will refer to them as optically blank fields hereafter.

In summary, the 3 σ hard sample consists of 126 identified objects (of which 3 are optically blank fields), 6 sources with ambiguous identification but with unambiguous color classification, and 4 sources with ambiguous identification and color classification.

Near-IR data from the UKIDSS survey (see subsection 2.2.2) are also available in a $\sim$ 0.8 deg^2 area in the VVDS region. We therefore searched for UKIDSS counterparts of X-ray sources in the 3 σ sample, using a radius of $4''$. We found a near-IR counterpart for 72 X-ray sources. Generally UKIDSS sources are coincident with optical counterparts. There are however two exceptions: source XMDS 449, for which the UKIDSS source lies between the two possible counterparts, at a distance of about $3''$ from both, and XMDS 760, for which there are two possible UKIDSS counterparts, both within $\sim 1''$ from the optical counterpart. The first case is one of the 4 X-ray sources that we could not identify, and the UKIDSS detection did not allow us to resolve the ambiguity. In the second case we associated to the optical counterpart the brightest UKIDSS source.

33 X-ray sources in the 3 σ hard sample (24%) have a radio counterpart at 1.4 GHz, one of them is also detected at 325 MHz. One is however associated to a spectroscopically confirmed cluster. The correlation between the X-ray and radio luminosities is explored in Polletta et al. in prep.

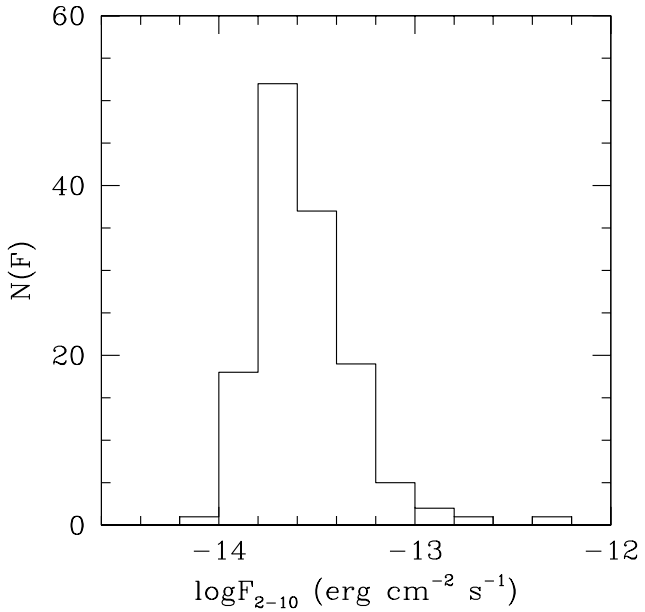

Figure 7.1: $2-10$ keV flux distribution for the 136 X-ray sources in the 3 σ hard sample.

Two of the optically identified X-ray sources correspond to spectroscopically confirmed galaxy clusters (XLSSC 025 and 041, see Pierre et al. 2006) and will not be considered in the following. The sample therefore reduces to 124 identified X-ray sources, and the 6 sources with ambiguous identification but with unambiguous color classification. Their X-ray, optical and infrared properties are reported in Table A.1.

In this and the following Chapters we will limit our analysis to sources in the 3 σ sample. This work is also reported in Tajer et al. submitted.

7.2 X-ray to optical ratio

The $2-10$ keV flux distribution of the 3 σ sample is shown in Fig. 7.1; the lowest flux sampled is $\sim 10^{-14}$ erg cm^{-2} s^{-1}.

We expect that almost all of X-ray sources in the 3 σ hard sample are AGN (see Chapter 1). The X-ray to optical ratio is a simple and useful tool to recognize them.

The X-ray to optical ratios of the sources in the sample are shown as a function of the X-ray flux in Fig. 7.2. They were computed using the VVDS R

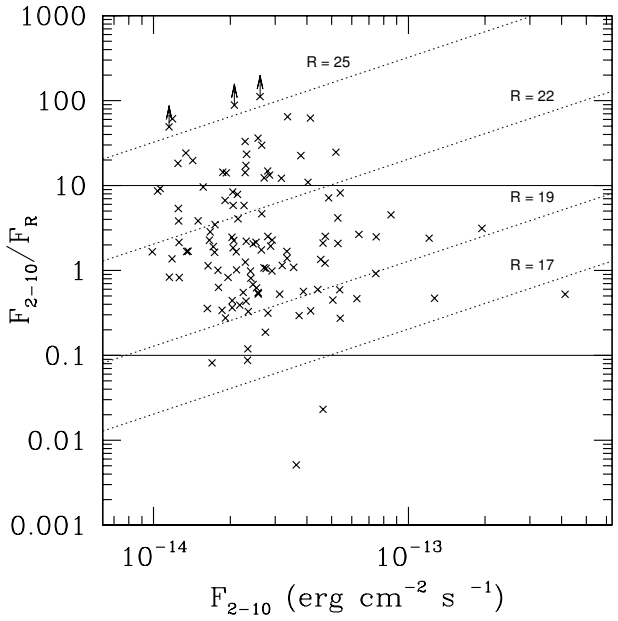

Figure 7.2: X-ray to optical ratio ($2-10$ keV band vs R band) as a function of X-ray flux for sources in the 3 σ hard sample. Diagonal dotted lines indicate loci of constant R magnitude while horizontal solid lines mark the region of canonical AGN ($0.1 < F_X/F_R < 10$). Lower limits mark the optically blank fields, whose R magnitude was fixed to 25.3 (see Fig. 13 in McCracken et al. 2003).

magnitudes (in the AB system)[1] according to the equation

$$\log(F_X/F_R) = \log F_X + 5.51 + R_{AB}/2.5 \tag{7.1}$$

where the constant derives from the standard conversion of AB magnitudes into monochromatic flux and from the integration of the monochromatic flux over the filter bandwidth assuming a flat spectrum. For about 20 objects in the sample, VVDS magnitudes were not fully reliable because the objects were saturated, or masked, or near the borders of the field of view; in these cases we used the CFHTLS r' band magnitudes and computed the X-ray to optical ratio using the appropriate conversion factor taken from Silverman et al. (2005).

About 80% of the sources are in the typical range of X-ray to optical ratio used to define the locus of AGN ($0.1 < F_X/F_R < 10$, see Fig. 1.7 and Akiyama et al. 2000; Hornschemeier et al. 2001). About 20% of the sources have instead

[1]This magnitude system is defined such that, when monochromatic flux f_ν is measured in erg cm^{-2} s^{-1} Hz^{-1}, $m_{AB} = -2.5\log f\nu - 48.60$, where the value of the constant is selected to define $m_{AB} = V$ for a flat-spectrum source (Oke 1974).

$F_X/F_R > 10$, which could indicate heavy absorption in the optical and/or high redshift (Hornschemeier et al. 2001). Only two sources fall significantly below the AGN borderline (XMDS 1248 and 842). Both objects appear extended in the optical as well as on the infrared images. The first (XMDS 1248) has a hardness ratio consistent with no intrinsic absorption in the X-ray spectrum, while the second (XMDS 842) has a hardness ratio consistent with X-ray absorption ($N_H \sim 10^{22}$ cm^{-2}). Using photometric redshifts (see Chapter 8), we obtained X-ray luminosities of $\sim 10^{40-41}$ erg s^{-1} for both of them, even when the absorption correction is taken into account for XMDS 842. We classify both as normal galaxies, though we can not exclude the presence of a low luminosity AGN or even a Compton thick AGN in XMDS 842 (see e.g. FSC 1021+4724 in Alexander et al. 2005a). There is in the sample another source with $L_{0.5-10} < 10^{42}$ erg s^{-1}, XMDS 178, however its X-ray to optical ratio of 0.27 puts it in the AGN class. We use here the X-ray to optical ratio criterion to distinguish between AGN and "normal" galaxies. Since we lack of optical spectroscopy and the X-ray statistics do not allows us to extract a spectrum, the classification of these "border line" objects remains dubious. However, this issue does not affect the results presented in the next Chapters.

To summarize, we identify 128 sources with AGN (including the 6 having 2 optical counterparts, but of the similar colors), and 2 with normal galaxies.

7.3 Optical magnitude and colors

The R_{AB} magnitude from the VVDS and $B-I$ color distributions for the identified sources are shown in Fig. 7.3 and 7.4.

The $B-I$ color distribution shows a high peak at $B-I \leq 1.0$, and a tail extending up to $B-I \sim 4$. Based on the observed color distribution we adopt a somewhat arbitrary threshold of $B-I = 1.0$ to divide the sample into two roughly equal size samples of "blue" objects, with $B-I < 1.0$ (43% of all sources), and "red" objects, with $B-I > 1.0$ (57%). As will be shown later, this criterion, although crude, proved to be a good one for a rough separation between type 1 AGN and type 2 AGN/normal galaxy-like AGN based on observed quantities alone, and is substantially confirmed by the more detailed (but model-dependent) classification based on the spectral energy distributions.

The magnitude distributions of these two broad classes are also plotted in Fig. 7.3: on average, blue sources ($B-I \leq 1.0$) are brighter, with a peak at $R \sim 20$ and 90% of objects at $R < 22$, while red sources ($B-I > 1.0$) have a

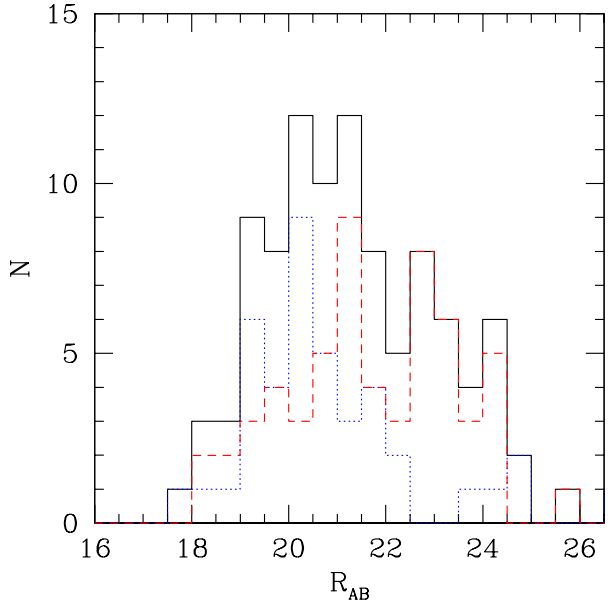

Figure 7.3: R magnitude distribution for the 3 σ hard sample. Solid histogram: total sample; dotted histogram: blue sources (see text); dashed histogram: red sources (see text).

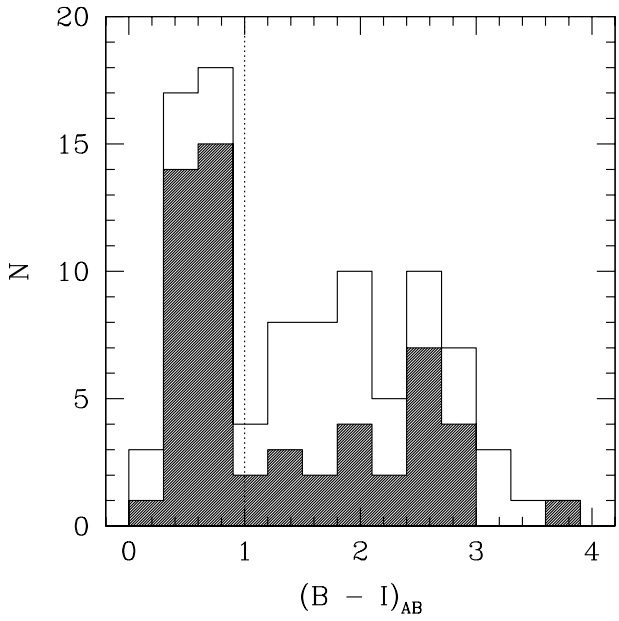

Figure 7.4: $B - I$ distribution for optical counterparts of X-ray sources in the 3 σ hard sample (solid line) and for X-ray sources detected with a signal to noise ratio > 4 in the hard band (shaded histogram). The dotted line marks the division between the adopted definition of "blue" and "red" objects (see text).

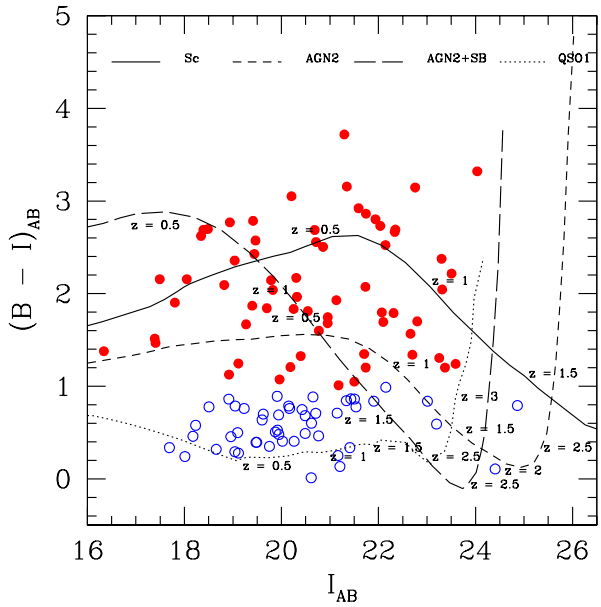

Figure 7.5: $B-I$ color vs I magnitude for sources in the 3 σ hard sample. Empty circles are blue objects, filled circles are red objects. Overimposed to points are the evolutionary tracks for an Sc galaxy (solid line), a type 1 QSO (dotted line), a type 2 AGN (short-dashed line) and a type 2 AGN plus a starburst component (long-dashed line). The B band absolute magnitudes assumed are -15.7 for the Sc galaxy template, -22.3 for the QSO1, -16.9 for the type 2 AGN and -23.9 for the type AGN plus starburst.

broader distribution, extending from $R \sim 18$ to $R \sim 26$.

In Fig. 7.5 we show the $B-I$ color as a function of the I magnitude for our sources, along with the evolutionary tracks for various kinds of galaxies and AGN: a late spiral galaxy (Sc, solid line), a type 1 QSO (dotted line), a type 2 AGN (short-dashed line) and a type 2 AGN plus a starburst component (long-dashed line). These tracks were obtained from a library of templates of SEDs of normal galaxies and AGN, which will be described in Chapter 8. The effects of absorption due to the Intergalactic Medium (IGM) have been taken into account at high redshift ($z \geq 2.5$) as prescribed in Madau (1995). Blue sources are near the QSO1 track, while red objects are generally consistent with normal galaxies and AGN2 tracks. Though a posteriori, this justifies our arbitrary separation at $B-I=1$.

We searched for a possible evolution of the $B-I$ distribution with X-ray flux. As we will show in the next Chapters, most of the red sources are consistent with being optically obscured and X-ray absorbed AGN. Since increasing the

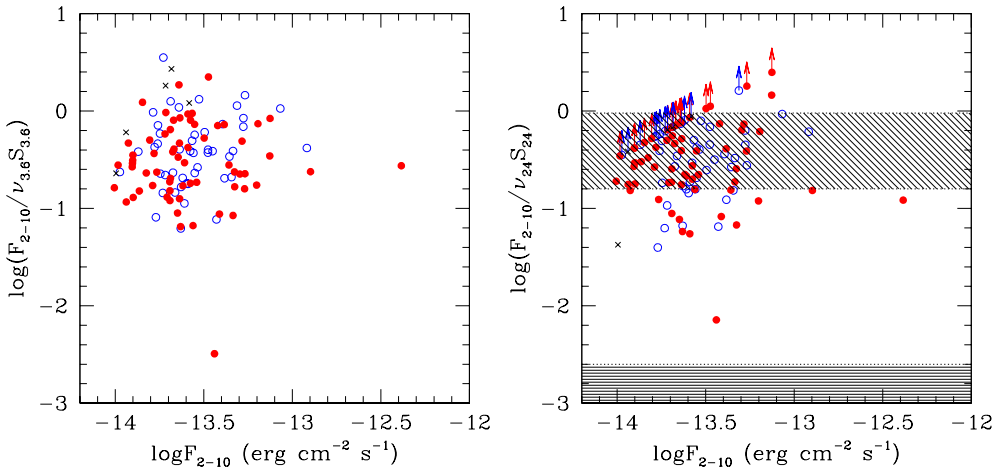

Figure 7.6: X-ray to IR ratio as a function of X-ray flux for sources in the 3 σ hard sample. Empty circles are blue sources, filled circles are red sources, crosses are the optically blank fields or sources with undefined color classification (because B or I magnitudes are not available). In the left panel IRAC 3.6 μm flux is used, while in the right panel MIPS 24 μm is used. Lower limits are sources detected in one or more IRAC bands and undetected in the MIPS 24 μm band, where 5 σ upper limit is used. The diagonally shaded area is the region occupied by hard X-ray selected AGN with IR emission and $z < 0.12$ from Piccinotti et al. (1982); the horizontally shaded area is the region occupied by local starburst galaxies from Ranalli et al. (2003).

S/N threshold implies that the flux limit increases, we selected from the 4 σ VVDS Catalogue (see Chapter 5) sources detected with a signal to noise ratio > 4 in the $2-10$ keV band; the shaded histogram in Fig. 7.4 shows their $B-I$ distribution. In this higher signal to noise subsample the proportion of blue and red sources (59% blue and 41% red) is inverted with respect to the 3 σ hard sample. This should imply that at fainter fluxes the number of obscured AGN should increase, and, based on the AGN unified model, we expect that also the fraction of X-ray absorbed (i.e. hard X-ray sources) AGN increases with decreasing X-ray flux. This topic will be discussed in Chapter 10.

7.4 X-ray to infrared ratios

As in the case of X-ray to optical ratio, AGN and starburst galaxies are known to have different X-ray to IR ratio values (Alonso-Herrero et al. 2004). In Fig. 7.6 we plot the ratios of X-ray to infrared fluxes at 3.6 μm (left panel) and 24 μm respectively (right panel) as a function of the X-ray flux. Sources are

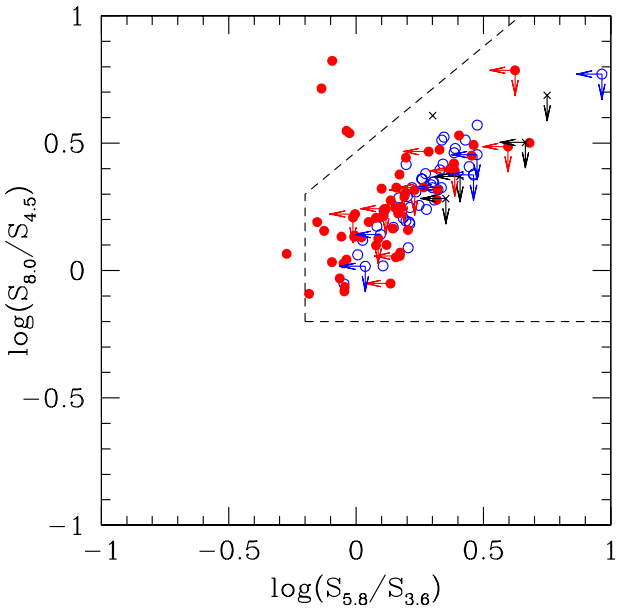

Figure 7.7: IRAC color - color plot for sources in the 3 σ hard sample. Empty circles are blue sources, filled circles are red sources, crosses are the optically blank fields or sources with undefined color classification. Left pointing arrows are sources undetected in the 5.8 μm band, down pointing arrows are sources undetected in the 8.0 μm band. 5 σ upper limits are used. The dashed lines mark the region expected for AGN according to Lacy et al. (2004)

all clustered in the same region with no clear separation between blue and red sources. We note that the same is true for the X-ray to optical ratio distribution. For this reason, we do not distinguish blue and red sources in Fig. 7.2.

Two typical loci of local sources are shown in the right panel of Fig. 7.6: the area at $-0.8 < \log F_X/F_{IR} < 0$ is the region occupied by hard X-ray selected AGN (from Piccinotti et al. 1982) with IR emission and $z < 0.12$; the area close to $\log F_X/F_{IR} = -3$ is the region occupied by local starburst galaxies from Ranalli et al. (2003), adapted from Alonso-Herrero et al. (2004). No objects with X-ray to infrared ratios typical of local starburst galaxies are found in our sample. 80% of the objects have X-ray/IR ratios $-1 < \log(F_X/\nu_{3.6}S_{3.6}) < 0$ (i.e. within a factor of 10), and 98% of them have $-1.2 < \log(F_X/\nu_{3.6}S_{3.6}) < 0.6$ (i.e. a factor of ~ 70). The most discrepant object is one of the two normal galaxies with low X-ray to optical ratio in Fig. 7.2. The X-ray to optical ratios for the same sources ranges from ~ 0.1 to ~ 60 (i.e. a factor of 600 excluding lower limits, see Fig. 7.2). This implies that the IR flux is a better diagnostics of the X-ray flux compared to the optical, a behaviour likely due the smaller extinction in the IR and to the fact that nuclear light absorbed by dust is likely re-radiated in the IR.

The observed range in the $F_X/\nu_{24}S_{24}$ plot is fully consistent with other X-ray and 24 μm samples, (e.g. Alonso-Herrero et al. 2004; Franceschini et al. 2005; Polletta et al. 2006), but broader than that of local hard X-ray selected AGN of Piccinotti et al. (1982). This broader dispersion is not surprising given the better sensitivity of X-ray observations with respect to the Piccinotti et al. (1982) data.

A broad range in the X-ray to infrared ratio could be caused by different amounts of absorption in different sources that depresses the observed X-ray flux, but not the infrared emission. Alternatively, it could be an intrinsic dispersion in the AGN SEDs that is not sampled properly in local objects. If this dispersion were due only to absorption in the X-rays, it would imply a broad range of column densities, up to 1.5×10^{23} cm^{-2}, consistent with the distribution of measured column densities (see Chapter 9). However, the similarity in the distribution of flux ratios of blue and red sources is not observed in the column density distribution, the majority of blue sources being unabsorbed and the majority of red sources being absorbed. These arguments suggest that the variety of the intrinsic SED shapes that characterize the AGN population is a more likely explanation and that such a variety is also observed for optically blue AGN. In fact a recent study of X-ray and 24μm-selected AGN by Rigby et al.

(2005) shows that there is no correlation between the ratio $F(X)/\nu_{24}F(24\mu\mathrm{m})$ and the amount of absorption in the X-rays, or their optical properties. Elvis et al. (1994) measure a dispersion of a factor of 10 at 24 μm for a large sample of optically-selected quasars after normalizing their SEDs at 1 μm, consistent with the observed dispersion in the X-ray/infrared flux ratios of our sample. An analysis of the SEDs of the AGN in the sample is presented in Chapter 8.

IRAC infrared colors proved to be a useful diagnostics to identify AGN among IR sources; in particular, Lacy et al. (2004) found that the 8.0/4.5 μm ratio vs the 5.8/3.6 μm ratio plot is effective in isolating AGN in IR selected samples, which have red colors (i.e. high values of the ratios) in both axis. In Fig. 7.7 we reproduce the plot of Lacy et al. (2004) for sources in our sample, and we find that the vast majority of them (both optically blue and red) lies in the region expected for AGN. At the boundaries of the AGN region there could be contamination by low redshift galaxies (Lacy et al. 2004); in fact, all the objects near the borders of the AGN region in Fig. 7.7 have a red optical color. The AGN with the reddest IR colors are predominantly blue in the optical, while optically red AGN show a broad range of IR colors.

Chapter 8

Photometric redshifts and Spectral Energy Distributions

Taking advantage of the broad band photometry in the optical (from the VVDS and the CFHTLS), near infrared (from UKIDSS) and mid infrared (from SWIRE), we were able to produce well sampled photometric distributions of the emission in the optical and IR bands for objects in the 3 σ hard sample. These data points were then compared with a range of templates that reproduce the SEDs of different types of sources from galaxies to AGN. From the comparison we could obtain a photometric redshift for each object and associate a photometric classification. In the present Chapter, we describe the procedure used to compute the photometric redshifts, the library of SED templates and the SEDs of our objects.

8.1 Template fitting and photometric redshift technique

In order to classify the SEDs and estimate photometric redshifts of the sources in the 3 σ hard sample, optical and IR data were combined and fitted with a library of galaxy and AGN templates. The SEDs were fitted using the HYPERZ code (Bolzonella et al. 2000). HYPERZ has been already successfully applied to various data sets and offers the possibility of using any template library and filters set. The code fits the observed photometric data with all the templates in the library, varying the redshift. The best fit is that with the minimum χ^2. The effects of dust extinction were taken into account by reddening the reference templates according to a selected reddening law. We used the extinction curve derived in high redshift starbursts by Calzetti et al. (2000). In order to limit degeneracies in the best fit solutions we limited the extinction A_V to be less

than 0.55 mag. and included templates of highly extincted objects to fit more heavily obscured sources.

The library contains 20 templates including 1 elliptical, 7 spirals, 3 starbursts, 6 AGN and 3 composite (starburst + AGN) templates covering the wavelength range between 1000 Å and 1000 μm. The elliptical, spiral and starburst templates were generated with the GRASIL code (Silva et al. 1998). The 7 spirals range from early to late types (S0 - Sd), the starburst templates correspond to the SEDs of NGC 6090, M82 and Arp 220. In all of the spirals and starburst templates the spectral region between 5 and 12 μm, where many broad emission and absorption features are observed, was replaced using observed IR spectra from the PHT-S spectrometer on the *Infrared Space Observatory* (ISO) and from IRS on *Spitzer*.

Templates for moderately luminous AGN, representing Seyfert 1.8 and Seyfert 2 galaxies, were obtained by combining models, broad band photometric data (from NED) and ISO PHT-S spectra of a random sample of 28 Seyfert galaxies with empirical interpolations.

The other four AGN templates include three templates representing optically selected QSOs with different values of infrared/optical flux ratios (QSO1, TQSO1 and BQSO1) and one type 2 QSO (QSO2). The QSO1 templates are derived by combining the SDSS quasar composite spectrum and rest frame infrared data of a sample of 35 SDSS/SWIRE quasars (Hatziminaoglou et al. 2005). After normalizing each SED in the optical, three templates are derived, one corresponding the the average of the entire sample (QSO1), one to the 25% of the sample with the highest IR data (TQSO1) and the third to the 25% of the sample with the lowest IR data (BQSO1). The QSO2 template was obtained by combining the observed optical/NIR spectrum of the red quasar FIRST J013435.7−093102 (Gregg et al. 2002) and the rest frame IR data from the quasars in the Palomar - Green sample with consistent optical SEDs (Polletta et al. 2006).

The composite (starburst + AGN) templates are empirical templates created to fit the SEDs of the following objects: the heavily obscured BAL QSO Mrk 231 (Berta 2005), the Seyfert 2 galaxy IRAS 19254−7245 South (I19254; Berta et al. 2003) and the Seyfert 2 galaxy IRAS 22491−1808 (I22491; Berta 2005). All these objects also show powerful starburst with an IR luminosity greater than 10^{12} $L_{\odot}$, which makes them ultraluminous infrared galaxies (ULIRGs, Sanders & Mirabel 1996).

The full library of galaxy and AGN templates, except the elliptical galaxy

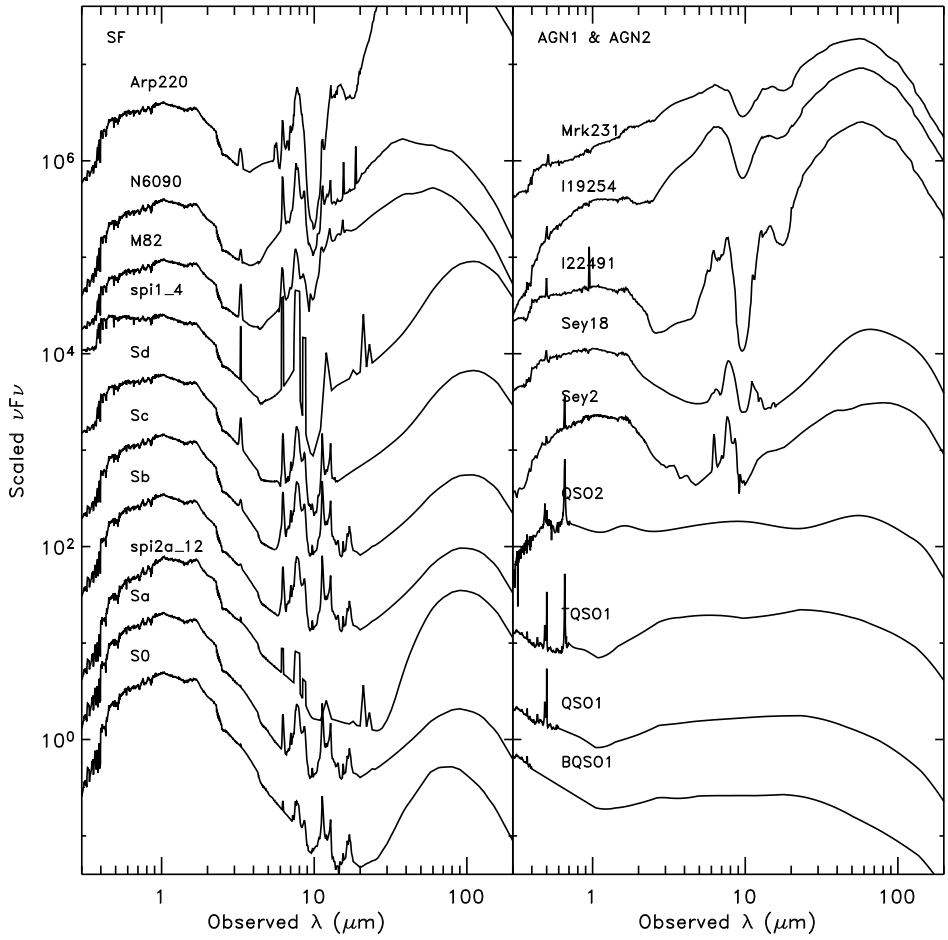

Figure 8.1: SEDs of the template library used to compute photometric redshifts. Spiral and starburst galaxy templates are shown in the left panel and AGN templates in the right panel; the type 2 AGN are the top 6 and the type 1 AGN are the bottom 3. The names of the templates are annotated. The elliptical galaxy template is not shown because no objects in the sample are fitted by such a template (see text).

one, because no source in the sample is best-fitted with an elliptical template, is shown in Fig. 8.1. With respect to existing template libraries derived from empirical SEDs (Coleman et al. 1980) or from models (Bruzual & Charlot 2003; Fioc & Rocca-Volmerange 1997; Silva et al. 1998; Devriendt et al. 1999), this library has a broader wavelength coverage and a larger variety of spectral types. Examples of application of this library to various types of SWIRE sources can be found in Lonsdale et al. (2004), Franceschini et al. (2005), Hatziminaoglou et al. (2005), Jarrett et al. (2006), Polletta et al. (2006) and Weedman et al. (2006).

Photometric redshift techniques have been applied to optical or optical and near-IR data sets providing reliable photometric redshifts (e.g. Rowan-Robinson et al. 2005; Ilbert et al. 2006; Brodwin et al. 2006). With a limited spectral coverage, some spectral types can be degenerate, e.g. obscured starbursts and ellipticals. In those cases, the inclusion of mid-IR data can break the degeneracy. However, the inclusion of mid-IR data in photometric redshift techniques could degrade the photometric redshifts estimates if the templates represent only a limited range of optical/IR ratios. In this work, we used both approaches, fitting optical + near-IR and optical + near-IR + mid-IR data, to maximize the accuracy and reliability of both the photometric redshift estimates and spectral type determination.

The SEDs were fitted twice, first using the data up to 4.5 μm, then including the data up to 24 μm. The best solution in each case corresponded to the solution with minimum χ^2 among all the solutions with $z = 0 - 4$ and B band absolute magnitude within a pre - defined range. The B band absolute magnitude range varied with redshift and was different for normal galaxies and for AGN templates. For normal galaxies, it must be greater than $-5\times\log(d_L)-6$ and lower than $-5 \times \log(d_L) - 0.7$, with d_L in Mpc, but always between the range $-23.5, -17$, while for AGN it must be greater than $-5\times\log(d_L)-6.5$ and lower than $-5\times\log(d_L)$, but always within the range $-27.5, -19$. If there were no solutions in the defined absolute magnitude range, the criterion was modified by extending the M_B limits by steps of 0.5 magnitudes, but always within the maximum allowed range (defined by the expressions reported above). The two solutions with the smallest χ^2 were retained for each of the two HYPERZ cycles (one obtained using only optical and near-IR data, the other obtained using also data from 5.8 to 24 μm). These 4 solutions were then weighted by the goodness of the fit and by the difference from the median redshift in order to select the solution with the lowest χ^2 and redshift closer to the median.

We obtained a redshift for all X-ray sources except the two confirmed clusters (134). We also obtained an estimate of redshifts for all optical objects associated to the 10 unidentified X-ray sources, but we will not use them in what follows. We will consider only the 121 objects with an identified optical counterpart and the 3 optically blank fields, for which the redshift and the photometric classification were based only on IR data (for a total of 124 objects). The photometric redshifts are reported in Table A.1.

In order to evaluate the quality of our photometric redshifts, we need a comparison with spectroscopic redshifts. 34 objects in the 3 σ hard sample have a spectroscopic redshifts: 8 objects are part of the VVDS spectroscopic sample (Gavignaud et al. 2006), 23 are included in a sample of 100 X-ray sources detected in the $2-10$ keV band in the XMM-LSS and with an optical spectrum available (these objects will be presented in Garcet et al., in prep.), 2 are taken from Lacy et al. (2006), who present optical spectroscopy of luminous AGN selected in the mid-IR in two fields covered by *Spitzer* observations, one of which is the XMM-LSS field, and for one object a redshift measurement is reported in NED. To obtain a larger set of data, we have also considered 16 additional sources that were observed as part of the VVDS spectroscopic sample and were included in the 4 σ VVDS sample discussed in Chapter 5, for which we could easily apply the same procedures to obtain SEDs and photometric redshifts. For 47 objects both optical and infrared photometric data were used, while for the remaining 3, which fall outside the area covered with SWIRE, only optical data were available. Photometric and spectroscopic redshifts are compared in in Fig. 8.2 and in Table 8.1 (for objects in the 3 σ hard sample) and Table 8.2 (for the 16 objects with spectroscopic redshifts in the 4 σ VVDS sample). Spectroscopic redshifts are also reported in Table A.1. Most of the objects are along the line of equality in Figure, with only few notable discrepancies.

The reliability and accuracy of the photometric redshifts are usually measured via the fractional error

$$\Delta z = \left(\frac{z_{phot} - z_{spec}}{1 + z_{spec}} \right) \tag{8.1}$$

and the rate of catastrophic outliers, defined as the fraction of sources with $|\Delta z| > 0.2$. For our 50 objects, the outlier fraction is 16%. These results are significantly better than what has been previously obtained for AGN samples, where the fraction of outliers is usually higher than 25% (Kitsionas et al. 2005; Babbedge et al. 2004). On the other hand, they are not as satisfactory as those

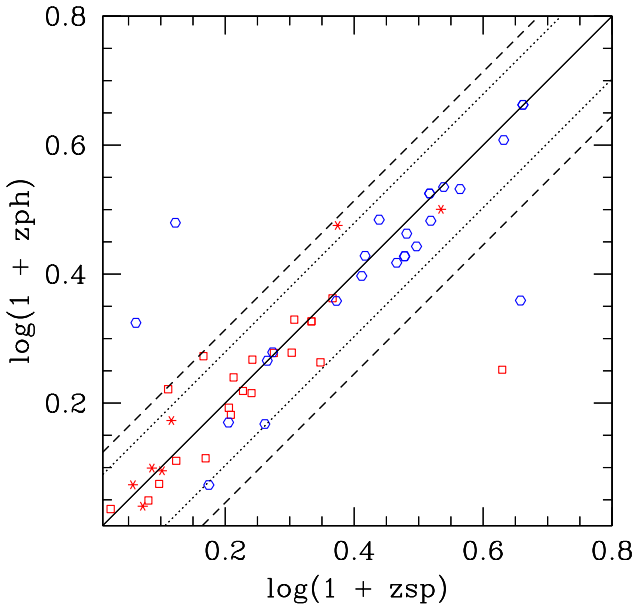

Figure 8.2: Photometric vs spectroscopic redshifts. Hexagons are type 1 AGN, empty squares are type 2 AGN and asterisks are star-forming like AGN. Solid line is the $z_{ph} = z_{sp}$ relationship, dotted lines mark the 20% "error" in $1 + z_{ph}$ and dashed lines mark the 30% "error" in $1 + z_{ph}$.

XMDS ID	z_{sp}	z_{ph}	Spectroscopic class.	SED class.	Ref.
4	0.265	0.245	AGN2	SF	Garcet et al. in prep.
12	3.5893	3.597	AGN1	AGN1	VVDS
55	1.029	1.135	AGN2	AGN2	Garcet et al. in prep.
60	0.478	0.302	AGN2	AGN2	Garcet et al. in prep.
112	0.878	0.900	AGN1	AGN1	Garcet et al. in prep.
118	1.1573	1.122	AGN1	AGN2	VVDS
140	0.220	0.257	AGN2	SF	Garcet et al. in prep.
161	0.0530	0.086	AGN1	AGN2	Lacy et al. (2006)
179	0.183	0.495	AGN1	AGN1	Garcet et al. in prep.
420	2.2900	2.350	AGN1	AGN1	VVDS
439	1.3679	1.988	em. line gal.	SF	VVDS
487	0.308	0.489	AGN2	SF	Garcet et al. in prep.
498	2.031	1.903	AGN1	AGN1	Garcet et al. in prep.
503	0.6336	0.737	early type gal.	AGN2	VVDS
505	0.327	2.018	AGN2	AGN1	Garcet et al. in prep.
521	1.3253	1.305	em. line gal.	AGN2	VVDS
523	2.0060	1.678	AGN1	AGN1	VVDS
571	2.666	2.404	AGN1	AGN1	Garcet et al. in prep.
577	0.2520	0.188	AGN2	AGN2	Lacy et al. (2006)
602	0.181	0.097	AGN2	SF	Garcet et al. in prep.
738	1.010	0.898	AGN1	AGN2	Garcet et al. in prep.
739	0.140	0.184	AGN2	SF	Garcet et al. in prep.
742	1.924	1.615	AGN1	AGN1	Garcet et al. in prep.
760	1.2275	0.833	em. line gal.	AGN2	VVDS
782	0.826	0.471	AGN1	AGN1	Garcet et al. in prep.
789	0.604	0.479	AGN1	AGN1	Garcet et al. in prep.
807	2.302	2.039	AGN1	AGN1	Garcet et al. in prep.
817	2.458	2.428	AGN1	AGN1	Garcet et al. in prep.
820	0.293	0.666	AGN2	AGN2	Garcet et al. in prep.
842	0.0430	0.010	gal.	SF	NED
846	0.842	0.844	AGN1	AGN1	Garcet et al. in prep.
1199	0.331	0.290	AGN2	AGN2	Garcet et al. in prep.
1246	3.550	1.286	AGN1	AGN1	Garcet et al. in prep.
1265	0.205	0.120	AGN2	AGN2	Garcet et al. in prep.

Table 8.1: Comparison between spectroscopic and photometric redshifts and classifications for objects with a spectroscopic redshift available in the 3 σ sample. The reference in the last column specify the origin of spectroscopic redshift.

XMDS ID	z_{sp}	z_{ph}	Spectroscopic class.	SED class.	Ref.
20	2.1384	1.773	AGN1	AGN1	VVDS
21	0.1524	1.111	AGN1	AGN1	VVDS
23	0.6173	0.520	em. line gal.	AGN2	VVDS
48	0.4671	0.874	gal.	AGN2	VVDS
80	0.8863	0.896	gal.	AGN2	VVDS
81	3.2852	3.055	AGN1	AGN1	VVDS
82	0.6890	0.655	gal.	AGN2	VVDS
84	1.5806	1.495	AGN1	AGN1	VVDS
89	1.3582	1.282	AGN1	AGN1	VVDS
176	0.7421	0.643	em. line gal.	AGN2	VVDS
187	0.6061	0.559	AGN1	AGN2	VVDS
412	2.4250	2.165	AGN1	SF	VVDS
448	1.7466	2.051	AGN1	AGN1	VVDS
480	3.2619	0.786	AGN1 (BAL QSO)	AGN2	VVDS
1238	0.7471	0.851	gal.	AGN2	VVDS
1259	1.6120	1.681	AGN1	AGN1	VVDS

Table 8.2: Comparison between spectroscopic and photometric redshifts and classifications for objects with a spectroscopic redshift available in the 4 σ VVDS sample (see text). The reference in the last column specify the origin of spectroscopic redshift.

obtained for galaxy populations, even when few photometric data points are available (Babbedge et al. 2004).

The achieved accuracy does not allow us to perform detailed analysis on single sources, however it is adequate for a statistical analysis of the population as presented in this work.

8.2 Spectral Energy Distributions and classification

Each source was classified according to the template which gives the best-fit solution. We defined three broad classes, type 1 AGN, type 2 AGN, or star forming galaxy-like AGN (SF). Since no source is best-fitted with an elliptical template, we do not consider such a class. The type 1 AGN class includes all of the sources best-fitted with a QSO1 template. The type 2 AGN class includes the sources best-fitted with either the two Seyfert 2 templates, the three composite AGN+starburst templates, or the QSO2 template. The SF class includes the sources fitted by a spiral or a starburst template. We classified 50 (40%) sources as type 1 AGN, 48 (39%) type 2 AGN and 26 (21%) SFs. The SED classification is also reported in Table A.1.

Examples of observed SEDs with their best fit templates are presented in Fig. 8.3. For sources with both optical and IR data, the photometric classification is reliable since the SED shape of the different classes has specific signatures that can be easily identified. Interestingly, while photometric redshifts for type 1 AGN might be the most uncertain, their classification is instead straightforward. On the other hand, the only difference between the AGN2 and SF classes is in the shape of the near- and mid-IR SED, and in case the fit is not optimal or when only few IR data points are available, the separation between the two classes is somewhat uncertain, as can be seen comparing the SEDs of left and middle panels in Fig. 8.3.

The terms type 1 and type 2 have been introduced to distinguish AGN characterized by the presence of, respectively, broad and narrow (high ionization) emission lines in their optical spectra. These are thought to correspond to a direct view of the nucleus or to an intervening obscuration of the broad emission line regions. Recently, X-ray observations have also revealed X-ray emission attributable to an AGN from objects which show galaxy-like spectra, e.g. XBONGs (Comastri et al. 2002), ELGs, and ALGs (Alexander et al. 2002, see also Moran et al. 2002 and Section 1.4). Given the very limited available spectroscopy, we base our classification only on the shape of the optical-IR

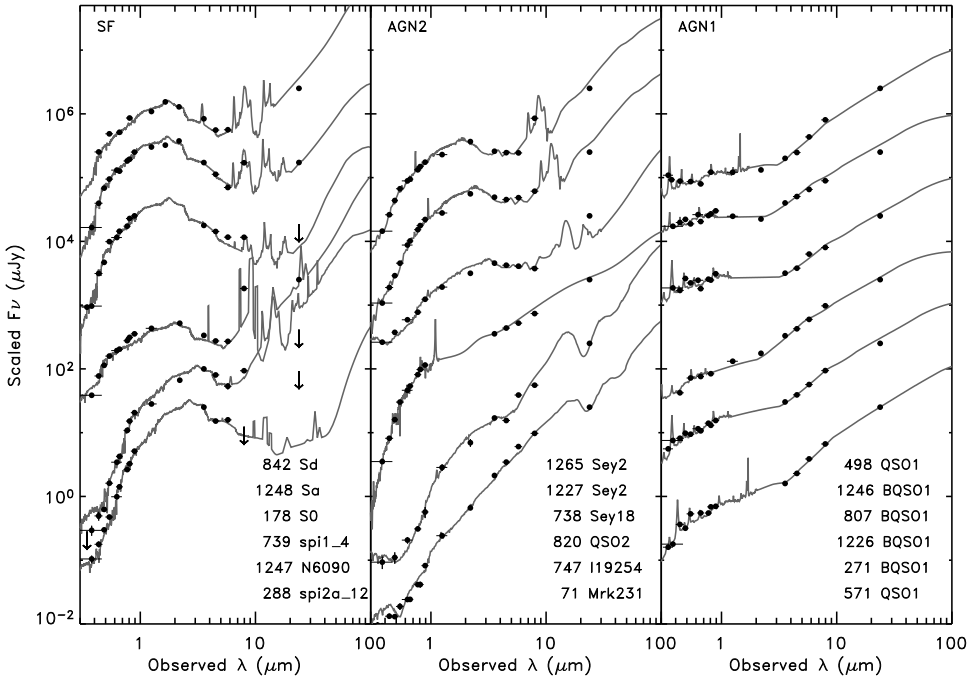

Figure 8.3: Observed SED (filled circles) and redshifted best-fit templates (grey solid curves) of 18 sources: 6 with star-forming like SEDs (left panel), 6 with type 2 AGN SEDs (middle panel), and 6 with type 1 AGN SEDs (right panel). Downward pointing arrows correspond to 5σ upper limits. The source sequence number and best-fit template names are listed in the same order as the SEDs are plotted.

SEDs. We adopt the point of view that objects with high X-ray luminosity ($> 10^{42}$ erg s^{-1}) must contain an AGN even in the absence of AGN signatures in their IR - optical SEDs.

In Table 8.1 and 8.2 the spectroscopic and photometric classifications are reported. About half of the spectra come from the VVDS, where objects are classified as type 1 AGN if broad lines with full width half maximum (FWHM) larger than 1000 km/s are identified in the spectrum. On the other hand, no attempt was made at this stage to separate starburst galaxies from type 2 AGN (see Le Fèvre et al. 2005; Gavignaud et al. 2006). The objects taken from the Garcet et al. (in prep.) sample are classified as type 1 AGN if lines with FWHM > 1500 km/s are found in the spectrum, while the type 2 AGN class includes both Narrow Emission Lines Galaxies and Absorption Lines Galaxies. Therefore, while the type 1 AGN spectroscopic classification can be considered secure, the remaining objects are simply classified as non type 1 AGN.

The agreement between spectroscopic and photometric classification is good. In the 3 σ hard sample (Table 8.1) there are only 4 objects (out of 34) with discrepant classifications: XMDS 505 is classified as type 1 AGN by our method but does not show broad emission lines in the spectrum (we also note that this object is one of the catastrophic outliers), while XMDS 118, 161 and 738 are photometrically classified as type 2 AGN, but spectroscopically classified as type 1 AGN. On the other hand, if we consider the spectra in the 4 σ VVDS sample (Table 8.2), we note that all the 3 objects with discrepant classifications (XMDS 187, 412 and 480) are photometrically classified as type 2 AGN or SFs and spectroscopically classified as type 1 AGN. It is therefore possible that with our method we underestimate the fraction of type 1 AGN with respect to that obtained using spectroscopic criteria. Based on the results obtained from this comparison, we expect that in about 20% of objects which show a type 2 AGN or a SF SED, i.e. where the AGN features are partly or totally obscured in the optical-IR, the broad emission lines could still be visible in the optical spectrum. These objects could be similar to the reddened type 1 quasars classified by Lacy et al. (2006), which generally have broad emission lines in the spectrum but a continuum significantly redder than that of a normal quasar. They classify them as obscured AGN. It is not possible at this stage a more detailed study of these objects. This would require, e.g., a high signal to noise spectrum over a large band, to compare the continuum shape with that obtained from the broad band photometry, and a larger sample of optical spectra.

In the following we will distinguish optically unobscured AGN (that based on the comparison with the spectroscopic sample are expected to have broad emission lines in the spectrum) from optically obscured ones (which will include all objects having type 2 AGN and SF spectral features). The latter group may include also some AGN with broad emission lines, but a significantly redder continuum than that of normal quasars.

In Fig. 8.4, we compare the classification based on the SED shape with the optical color $B - I$ (see Chapter 7) as a function of redshift. The horizontal dashed line corresponds to the threshold between blue and red sources ($B-I = 1$). 90% of the blue objects are classified as unobscured AGN and 94% of red sources are classified as obscured AGN. Thus the simple classification based on observed color appears in retrospect rather successful when compared with the more sophisticated template fitting procedure. However, while at $z < 1.6$ the SED and "color" classifications practically coincide (except for 2 obscured objects near the borderline), at larger redshifts there is a degeneracy among the

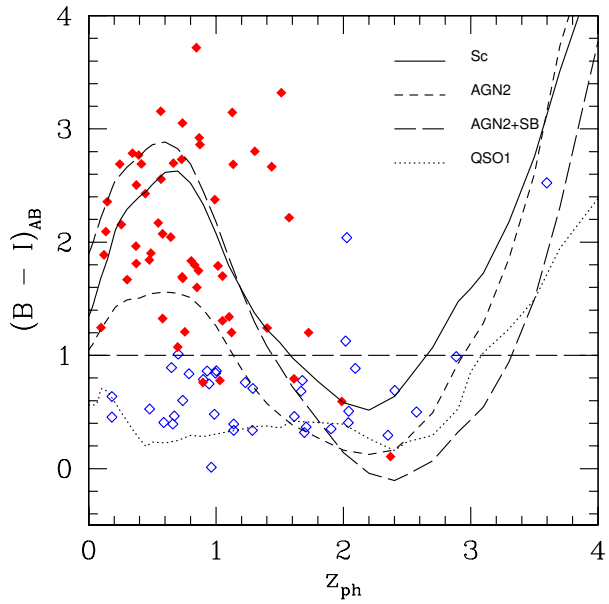

Figure 8.4: $B - I$ distribution of sources in the 3 σ sample as a function of photometric redshift. Empty diamonds are optically unobscured AGN, filled diamonds are optically obscured AGN. Overimposed to points are the evolutionary tracks for an Sc galaxy (solid line), for a type 1 QSO (dotted line), for a type 2 AGN (short-dashed line) and a type 2 AGN plus a starburst component (long-dashed line).

different evolutionary tracks so that the optical color alone is not indicative of a spectral type.

Among the optically obscured AGN, the number of objects fitted by a SF template is quite high (26 of 124) for a sample of AGN. However there can be no doubt that these systems harbor AGN, since all of them except the three discussed in Section 7.2 have high X-ray luminosities, inconsistent with those of "normal" galaxies ($L_X \geq 10^{42}$ erg s^{-1}).

The distribution of photometric redshifts is shown in Fig. 8.5. The overall distribution, reported in both panels, shows a peak at $z \sim 1$. The majority (57%) of sources has $z < 1$, with a tail extending up to $z \sim 4$. These results are consistent with the redshift distribution of other X-ray selected samples (e.g. Barger et al. 2003; Hasinger 2003; Barger et al. 2005).

The redshift distributions of the unobscured and obscured AGN defined in the analysis of their SEDs are shown in the left and right panels, respectively. The two are clearly different: the first is broader and reaches higher redshifts, while obscured AGN appear more concentrated at $z < 1$ (70%). Several authors

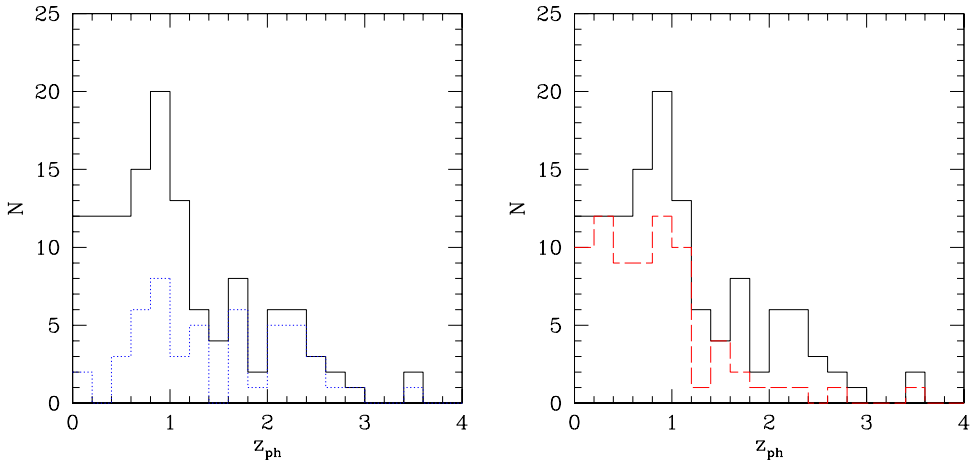

Figure 8.5: Distribution of photometric redshifts. Left panel: total sample (solid histogram) and optically unobscured AGN (dotted histogram); right panel: total sample (solid histogram) and optically obscured AGN (dashed histogram).

(e.g. Steffen et al. 2004; Treister et al. 2005; La Franca et al. 2005; Eckart et al. 2006) find different redshift distributions for type 1 and non type 1 AGN. An analysis on the fraction of obscured and unobscured AGN as a function of redshift will be discussed in Chapter 10.

Chapter 9

X-ray spectral properties

We studied the X-ray spectral properties of our sample, both with spectral fitting, for individual sources with a sufficient number of counts (Section 9.1), and using hardness ratios, for fainter sources (Section 9.2). In the majority of cases we aimed at obtaining a reliable measure of N_H. A stacking technique was also used to study systematic trends in the whole sample (Section 9.3).

9.1 Individual sources

We extracted spectra for all sources having at least 50 net counts in the MOS + pn merged image in the $2-10$ keV band. There are 55 X-ray sources in our catalogue which satisfy this criterion; 24 of them are optically unobscured AGN, and 31 are optically obscured AGN.

Counts were extracted for each source using the *XMM – Newton* Science Analysis System (SAS) `evselect` task in a circular region with a radius of $20''$, corresponding to an encircled energy fraction of $\sim 70-75\%$ (off-axis angles between 0 and $10'$), for a point-like source. The pn data were used, unless the source was close to a CCD gap, in which case we used the MOS data, fitting simultaneously MOS1 and MOS2. Background counts were extracted from a nearby circle in a source free region, excluding areas near gaps in the CCD array. We used the SAS `rmfgen` task to create response matrices (one for each camera and each XMDS pointing) and `arfgen` to generate ancillary response files (one for each source).

X-ray spectra were analyzed using the XSPEC package (v. 11.3.1). We considered the energy range $0.3-10$ keV. When the number of counts was large enough, we binned the data in order to have at least 15 or 20 counts for each energy channel and χ^2 statistics was used, otherwise we used Cash statistics

(Cash 1979), which, however, does not give a "goodness of fit" evaluation, like the χ^2. In order to better match the spectral resolution of the instruments, we binned the data of these sources with few counts using a fixed number of PHA channels before fitting using the Cash statistics.

We first fitted the spectra using a simple power law model with galactic absorption computed at the XMDS position ($N_H = 2.6 \times 10^{20}$ cm^{-2}, Dickey & Lockman 1990), plus a component for intrinsic absorption at $z = 0$ (XSPEC model: `phabs*zphabs*pow` with abundance table of Wilms et al. 2000).

For all spectra for which χ^2 statistics can be used in the fit (22 sources), we set both intrinsic column density and photon index as free parameters. Spectral fit results are reported in Table B.1 in Appendix B. The errors in Tables and Figures correspond to the 90% confidence level for one interesting parameter. The average photon index is $\Gamma \sim 2.1$ and $N_H < 10^{21}$ cm^{-2}. They cannot be considered representative of the whole sample, because they are the brightest sources and generally they are less affected by X-ray absorption than fainter sources.

We then fixed the photon index for all the 55 objects, in order to obtain an estimate of the column density. We used two different values of the photon index, $\Gamma = 2.0$ and $\Gamma = 1.7$, both appropriate for AGN (Turner & Pounds 1989; Nandra & Pounds 1994). Results for $\Gamma = 2.0$ and $\Gamma = 1.7$ are reported in Table B.2 in Appendix B. The best fit values of N_H obtained with $\Gamma = 2.0$ are higher than those obtained with photon index frozen to 1.7, however the two column density estimates are consistent within errors in 90% of cases. The two N_H distributions are compared in Fig. 9.1.

For three sources (XMDS 161, 282 and 1199, see Table B.2) the spectral model with $\Gamma = 2.0$ gives a poor fit ($\chi^2_\nu > 2$). XMDS 1199 shows a moderate X-ray absorption ($N_H \sim 10^{21}$ cm^{-2}) and Γ frozen to 1.7 gives a better fit ($\chi^2_\nu = 1.35$). The other two sources have instead very steep spectra, in fact the spectral fit obtained with free photon index (see Table B.1) gives $\Gamma > 2$ for both of them, but, while for XMDS 282 the fit with Γ free is quite good ($\chi^2_\nu = 1.07$), we were not able to find an acceptable fit with a simple power law model for XMDS 161, as shown in Fig. 9.2, where it is evident that the spectrum exhibits a significant soft excess with respect to the single power law model. The soft excess has been shown to be a common feature of the X-ray spectra of Seyfert 1 and Seyfert 2 galaxies (e.g. Turner & Pounds 1989; Turner et al. 1997). The physical origin of this emission is still unclear. It has been interpreted as primary emission from the accretion disk, gravitational energy released by viscosity in

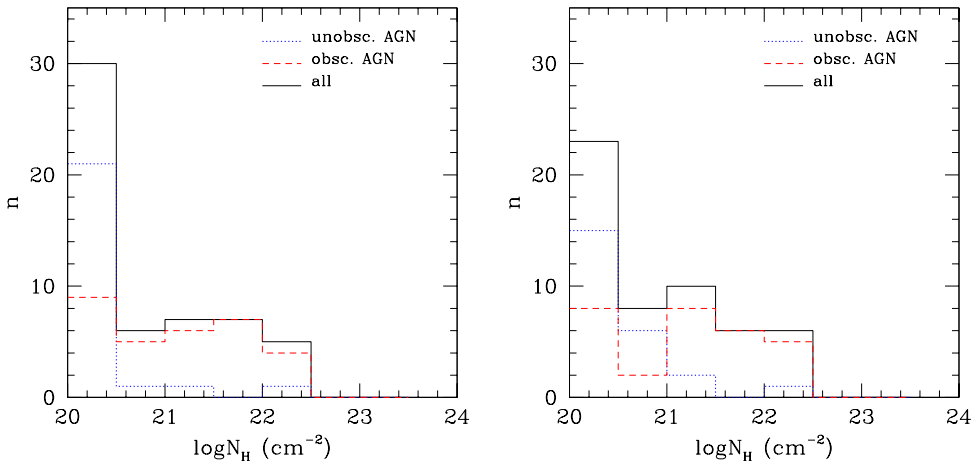

Figure 9.1: Column density distribution for X-ray spectra fitted by the simple absorbed power law model with $\Gamma = 1.7$ (left panel) and $\Gamma = 2.0$ (right panel). Solid histogram refers to the whole sample, dotted and dashed histograms refer to optically unobscured AGN and optically obscured AGN, respectively.

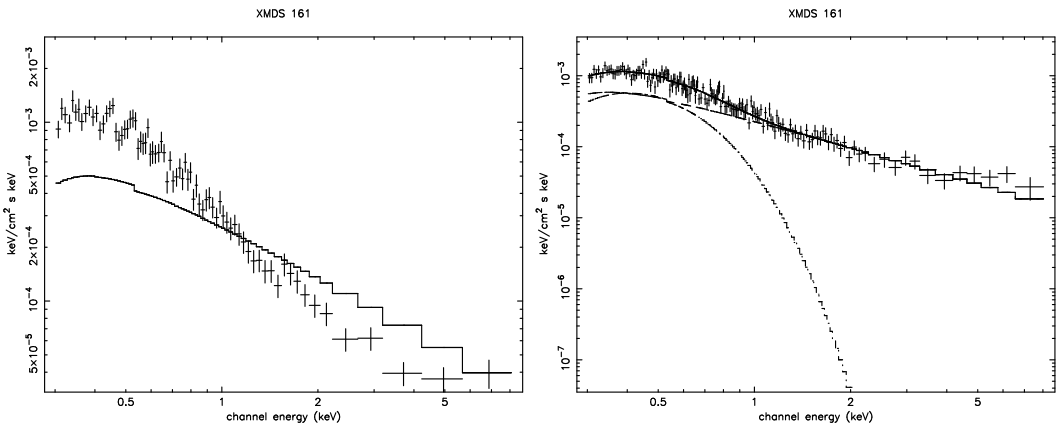

Figure 9.2: Unfolded spectrum of source XMDS 161, fitted by a simple power law model with $\Gamma = 2.0$ (left panel) and with a power law plus a low temperature black body component (right panel).

the disk, or as secondary radiation from the reprocessing of hard X-rays in the surface layers of the disk (see also Section 1.1). It is often modeled with a black body spectrum with low temperature ($kT \sim 0.1 - 0.2$ keV, see e.g. Mateos et al. 2005a,b; Galbiati et al. 2005). XMDS 161 is the brightest source found in the XMDS; its spectrum has about 5000 net counts, so that a more detailed spectral analysis was possible. We therefore fitted the spectrum with a power law plus black body component, with the Galactic absorption (XSPEC model `phabs*(pow + bbody)`). We obtained a black body temperature $kT = 0.11^{+0.07}_{-0.08}$ keV and a photon index of $\Gamma = 2.29 \pm 0.15$, with a $\chi^2_\nu = 0.92$. The temperature and the photon index obtained are fully consistent with those found by Mateos et al. (2005a,b). The spectrum of XMDS 161 along with the black body plus power law model is shown in the right panel of Fig. 9.2.

When $\Gamma = 1.7$, there are 9 sources in the spectral sample (apart for XMDS 161) having $\chi^2_\nu > 2$: all of them are bright, soft sources, for which the spectral fit with free photon index gives $\Gamma > 2$. In 5 cases there are some evidences of soft excess, but the low statistics prevents us to perform a detailed spectral analysis.

For sources XMDS 124 and 779 no stable solutions were found fixing the photon index to 2.0.

Examples of spectra of different count statistics, with and without evidences of photometric absorption are shown in Fig. 9.3 and 9.4.

The observed column density distributions of optically obscured and unobscured AGN turn out to be different: considering the distribution obtained with Γ fixed to 2.0, 13% of unobscured AGN (3 out of 24) have $N_H > 10^{21}$ cm^{-2}, while more than 65% of obscured AGN (19 out of 29) have $N_H > 10^{21}$ cm^{-2}.

To compute intrinsic column densities, we have to introduce the redshift dependence in the spectral model (`phabs*zphabs*pow`). Spectral fit results, along with redshifts, are reported in Table B.2 in Appendix B. We used photometric redshifts in all cases but XMDS 521, for which the spectroscopic redshift is available. The photon index was left free when the χ^2 statistics could be used, otherwise it was fixed to 2.0, except in the cases of XMDS 124, 779 and 739, where no stable solution was found for $\Gamma = 2.0$ and we fixed the photon index to 1.7. For XMDS 453 no stable solution was found with either values of Γ, therefore no value of the intrinsic column density is reported for this source in Table B.2. We computed its intrinsic column density from the observed one, as explained in Sec. 9.2.

Fig. 9.5 shows the intrinsic N_H distribution. Again, optically obscured and

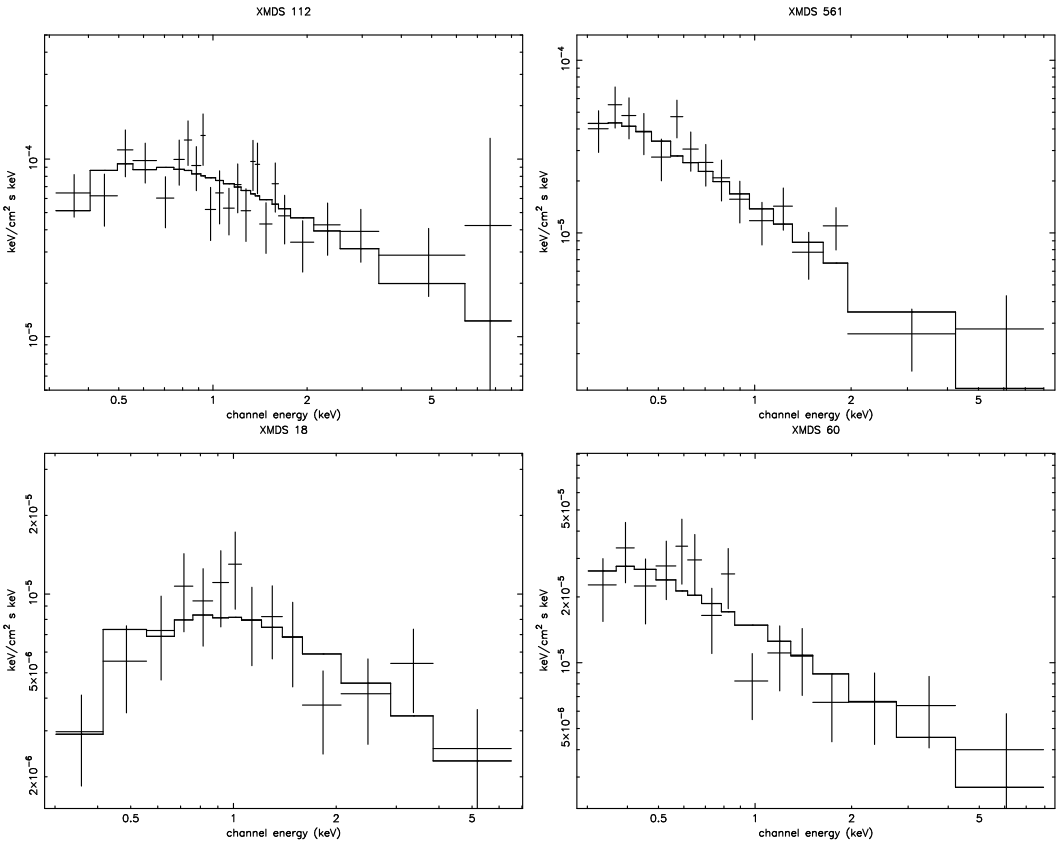

Figure 9.3: Examples of spectra with a measured X-ray absorption (left) and with column density consistent with the galactic value (right). All spectra are extracted from the pn camera, except that of XMDS 112, which is extracted from the MOS1 camera. Upper left: XMDS 112 (345 net counts); upper right: XMDS 561 (251 net counts); lower left: XMDS 18 (151 net counts); lower right: XMDS 60 (166 net counts). The counts reported here are values measured by XSPEC within the source area and in the single camera used. As a consequence, they are smaller than the net counts reported in the database and used to select the sources for spectral analysis.

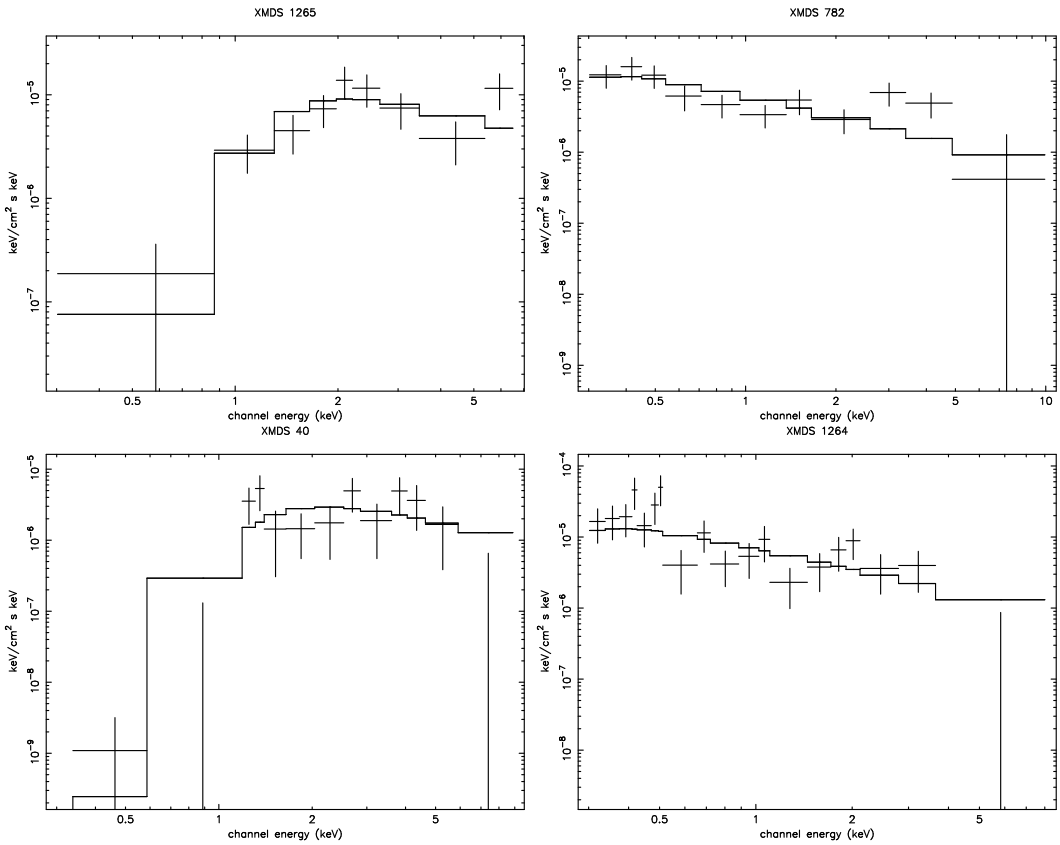

Figure 9.4: Other examples of spectra with a measured X-ray absorption (left) and with column density consistent with the galactic value (right). All spectra are extracted from the pn camera. Upper left: XMDS 1265 (103 net counts); upper right: XMDS 782 (110 net counts); lower left: XMDS 40 (72 net counts); lower right: XMDS 1264 (99 net counts). As explained in the text, when the Cash statistics was used, data were binned using a fixed number of PHA channels; here data are binned using a fixed number of counts only for graphical purposes.

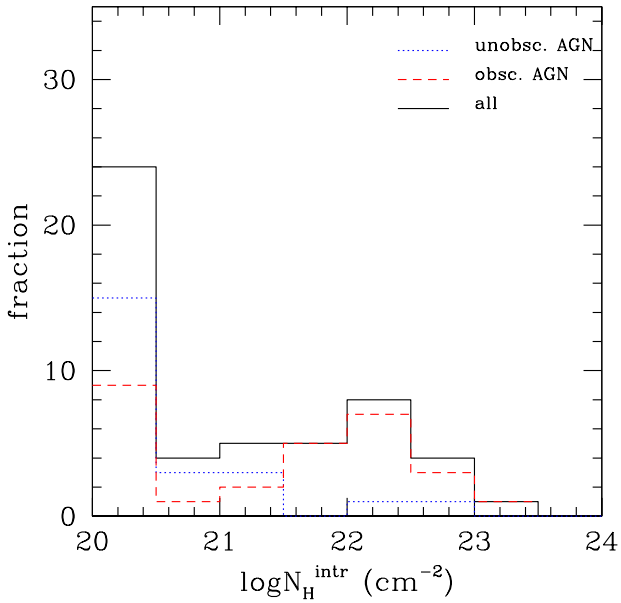

Figure 9.5: Intrinsic column density distribution for X-ray spectra fitted by the simple absorbed power law model, using photometric redshifts (or spectroscopic, for XMDS 521). Solid histogram refers to the whole sample, dotted and dashed histograms refer to optically unobscured and optically obscured AGN, respectively.

unobscured AGN have different distributions, with 64% of obscured AGN (18 out of 28) having $N_H > 10^{21}$ cm^{-2} and $\sim 40\%$ (11 out of 28) with $N_H > 10^{22}$ cm^{-2}. For comparison, only 17% of unobscured AGN (5 out of 23) have $N_H > 10^{21}$ cm^{-2} and 9% (2 out of 23) have $N_H > 10^{22}$ cm^{-2}.

In Fig. 9.6 the intrinsic column density is shown as a function of redshift; this figure is qualitatively consistent with those presented in other surveys (e.g. Eckart et al. 2006) and shows no obvious trend with z, although we also notice the paucity of high redshift sources with well constrained measures of N_H.

9.2 X-ray absorption

For faint sources, where individual spectral analysis is not feasible, hardness ratios can give some spectral information. The X-ray color - color plot for the sources in the present sample is shown in Fig. 9.7. The two hardness ratios HR_{cb} and HR_{dc} defined by equations (4.9) and (4.10) are used. Different symbols indicate the optically obscured/unobscured classification. Also shown are two lines corresponding to a spectral index of 2.0 for $z = 0$ and $z = 1$ for different

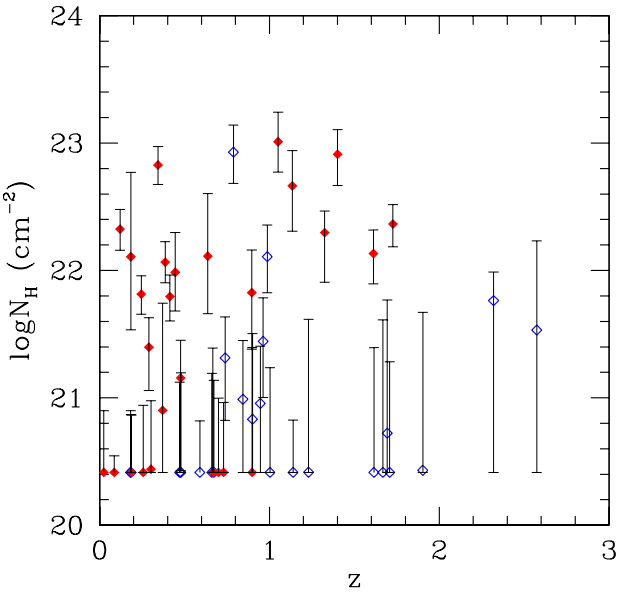

Figure 9.6: Intrinsic column density vs photometric or spectroscopic redshift. Empty diamonds are optically unobscured AGN, filled diamonds are optically obscured AGN.

values of N_H.

Less than 10% of the objects classified as optically unobscured AGN have $HR_{cb} > -0.3$ (corresponding to $N_H \sim 10^{21.5}$), while about 47% of the sources classified as obscured AGN have $HR_{cb} > -0.3$, indicating that X-ray absorption and a type 2 classification are often associated.

For a quantitative estimate of the absorbing column N_H we used the results of the spectral fits described in Section 9.1 with Γ fixed to 2.0 for the 51 brightest sources and computed the column density from the X-ray hardness ratios in the remaining cases in the following way.

We used the standard hardness ratio HR, defined as

$$\mathrm{HR} = \frac{CR_{2-10} - CR_{0.5-2}}{CR_{2-10} + CR_{0.5-2}} \tag{9.1}$$

where CR are the count rates in the $2-10$ and $0.5-2$ keV bands. We made simulations using XSPEC to obtain hardness ratios corresponding to typical values of N_H ranging from 10^{20} to 10^{24} cm^{-2}. A simple power law model with photon index $\Gamma = 2.0$ was assumed, consistently with the model used for the X-ray spectral analysis. In Fig. 9.8 we show the column density obtained from

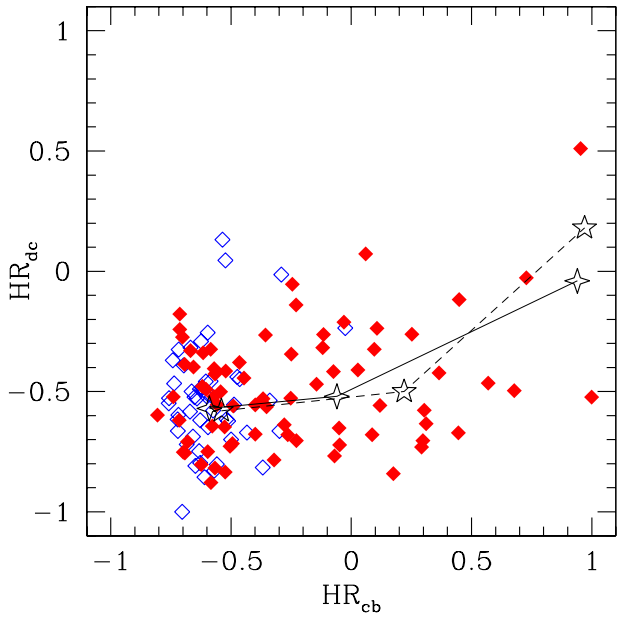

Figure 9.7: X-ray color - color plot for sources in the 3 σ hard sample. Energy bands involved are: $0.5-2$ (b), $2-4.5$ (c) and $4.5-10$ keV (d). Sources are classified as optically unobscured AGN (empty diamonds) or obscured AGN (filled diamonds). We also mark the hardness ratios computed for a simple absorbed power law spectral model, with $\Gamma = 2$ and $\log N_H = 21$, 22, 23 for $z = 0$ (four point stars connected by the solid line, from left to right) and $\log N_H = 22$, 23, 24 for $z = 1$ (five points stars connected by the dashed line, from left to right).

X-ray spectra as a function of the hardness ratio, compared to values computed from simulations (empty squares). The simulations and the objects for which a spectrum could be extracted define a clear relationship between N_H and HR for HR > -0.5, while, below these values, the HR - N_H relation degenerates. We therefore fixed the latter value, corresponding to $N_H \sim 10^{21}$ cm^{-2}, as a threshold below which all column densities are fixed to the galactic value. By interpolation we computed the observed N_H corresponding to the hardness ratio of each source. The intrinsic column density was then obtained from the observed one using the photometric (or spectroscopic, when available) redshift and the expression

$$N_H^{intr} = N_H^{obs}(1+z)^{2.6} \tag{9.2}$$

(Barger et al. 2002). For consistency, we also recomputed the intrinsic N_H for

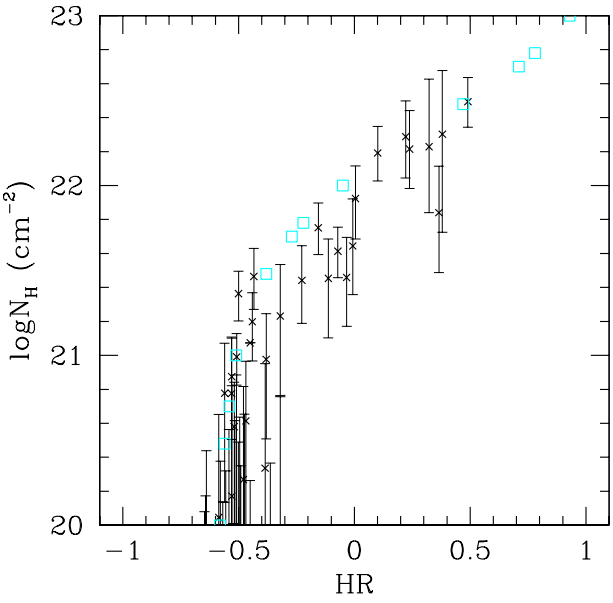

Figure 9.8: Observed column density estimated from the X-ray spectral analysis (with $\Gamma = 2.0$, see Section 9.1) as a function of the hardness ratio between the $2-10$ and $0.5-2$ keV bands, with their errors, compared with HR values obtained from XSPEC simulations for fixed values of N_H (empty squares, see text).

all sources for which a more detailed spectral analysis was possible (i.e. sources in Table B.2), using the observed N_H obtained from the spectrum. Intrinsic N_H reported in Table B.2 can be different from those computed from Eq. (9.2) both because the value given by XSPEC comes from a fit, and because in some cases in the spectral fit the photon index was left free (see Section 9.1). However, for $\sim 80\%$ of sources, the two N_H estimates are in agreement within a factor of ~ 3; the most discrepant casesare those where the photon index was left free in the spectral fitand the best fit value was significantly different from 2.0. N_H^{intr} was not computed when the observed column density was fixed to the galactic value.

The observed and intrinsic column density distributions are reported in Fig. 9.9. Different lines (dotted/dashed) refer to the N_H distribution for optically unobscured and obscured AGN respectively. Our choice of setting a fixed value for low N_H creates an artificial gap in the distribution.

As shown in Fig. 9.7, only 2 of the 49 unobscured AGN (4%) have hardness ratio consistent with significant X-ray absorption ($N_H^{obs} > 10^{22}$ cm^{-2}). On the other hand, when intrinsic column densities are computed, we find that more

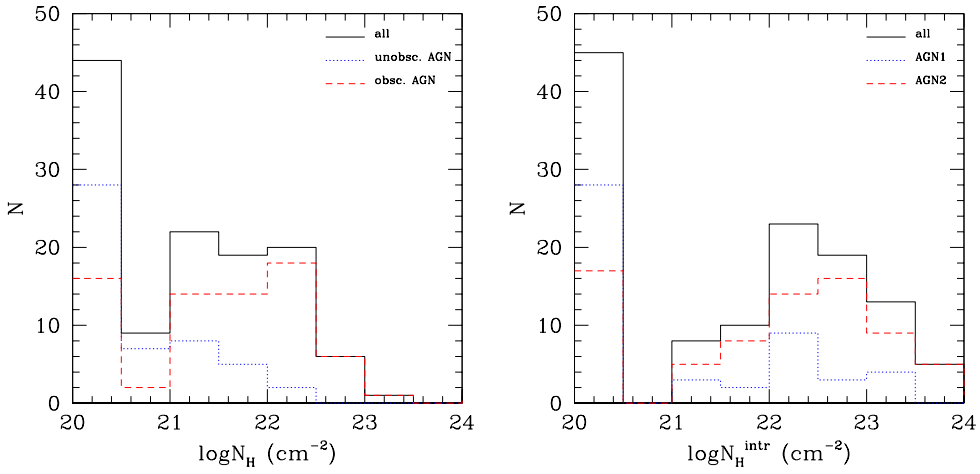

Figure 9.9: Distribution of observed (left panel) and intrinsic (right panel) column density. Solid histogram refers to the whole sample, dotted histogram refers to optically unobscured AGN and dashed histogram refers to optically obscured AGN.

than 30% of the unobscured AGN have $N_H^{intr} > 10^{22}$ cm^{-2}. For comparison, the fraction of unobscured AGN with $N_H^{intr} > 10^{22}$ cm^{-2} found in the X-ray spectral sample is 9% (see Section 9.1). The sources for which a spectral analysis is feasible are those with at least 50 net counts in the $2-10$ keV band: this cut will favor less absorbed sources.

As shown in Fig. 8.5, most of the unobscured objects have a redshift $z > 1$. It is well known that N_H values are less well constrained with increasing redshifts (see e.g. Eckart et al. 2006; Akylas et al. 2006; Tozzi et al. 2006), where the absorption cut - off shifts out of the observed band. This happens for $z \gtrsim 1.5$ (at this redshift, an intrinsic N_H of 10^{22} cm^{-2} corresponds to an observed column density $\lesssim 10^{21}$ cm^{-2}) and the effect is more relevant for unobscured AGN, whose hardness ratios generally cluster around -0.5 (which corresponds to $N_H^{obs} \sim 10^{21}$ cm^{-2}, see above), than for obscured AGN, which have a broader HR distribution. Within this sample, we have partially compensated for this effect with our choice of fixing intrinsic columns to 0 when the observed hardness ratio HR ~ -0.5. Moreover, we have at least 5 examples of optically unobscured AGN (XMDS 12, 258, 280, 406 and 840) in which the *observed* N_H is already larger than $N_H = 5 \times 10^{21}$ cm^{-2}, ensuring that the large columns are not all to be attributed to the redshift effects.

On the other hand, among the objects for which we are not able to estimate the column density (those with N_H fixed to the galactic value), there could be

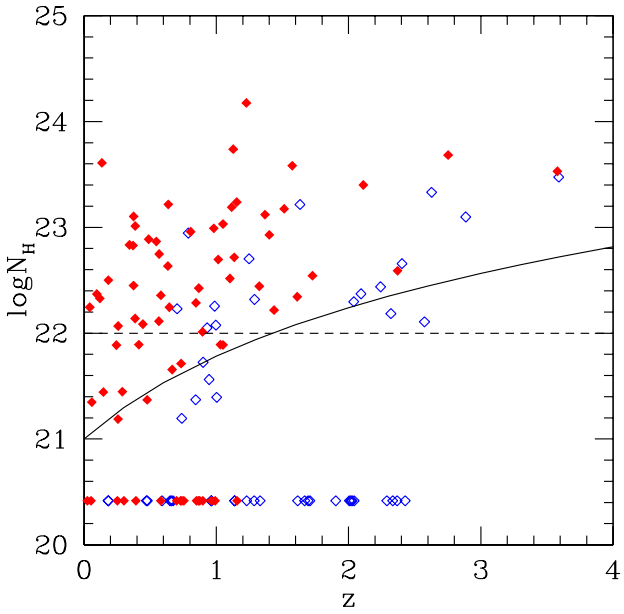

Figure 9.10: Intrinsic column density vs photometric (or spectroscopic, when available) redshift. Empty diamonds are optically unobscured AGN and filled diamonds are optically obscured AGN. The dashed line marks the threshold between X-ray absorbed and unabsorbed sources. The solid line shows the intrinsic column density that would be derived at a given redshift, for a measured column density of 10^{21} cm^{-2} in the observer frame.

some which could be really X-ray absorbed. In Fig. 9.10 we show the intrinsic column density of our objects as a function of redshift. The solid line shows the intrinsic N_H values that would be derived at a given redshift, for an observed column density of 10^{21} cm^{-2}. The few objects with intrinsic column density greater than the galactic value, but below the solid line in Figure, are sources with observed N_H (estimated from the spectral fit) exceeding the galactic value but below 10^{21} cm^{-2}. The objects without a spectrum and HR < -0.5 have been all plotted at $N_H = 2.6 \times 10^{20}$ cm^{-2}. Some of them could have indeed an observed column density greater than the galactic value, but $< 10^{21}$ cm^{-2}. As a consequence, their intrinsic column density should lie below the solid line in Figure. It is therefore possible that we underestimate the number of X-ray absorbed objects only for redshift $z \gtrsim 1.5$ (where the solid and dashed line cross). The column densities are difficult to estimate at high redshift, but this should not affect our results.

9.3 Stacking analysis

Given that less than half of the sources in our sample have a sufficient number of counts to perform a spectral analysis, we used a stacking technique to measure the spectral properties, averaged on the whole redshift range, of sources of different classification and in different flux intervals.

For the stacking analysis we used only pn data, because of the pn larger effective area; we selected only sources which are not in or near a pn CCD gap or bad column. Moreover, since the pn point spread function (PSF) and the vignetting are not well determined for large off-axis angles (Ghizzardi 2002; Kirsh 2006), we only used sources with off-axis angle $\theta < 11'$. This value allows us to obtain a significant number of sources (83), for which calibration should be still reliable. 38 sources are optically unobscured AGN and 45 are optically obscured AGN.

We have restricted the source area to a fixed radius of $15''$, which, on-axis, corresponds to 67% of the encircled energy for a point-like source. Since with this radius we sample the PSF core and not the wings, the encircled energy fraction has a weak dependence on the off-axis angle (at $\theta = 10'$ 67% of the encircled energy is within a $16''$ radius) and the energy dependence can also be neglected. Therefore, we can consider all sources together regardless of their position in the field. A background spectrum was extracted for each source from a nearby circle in a source free region. Ancillary response files were also produced for each source, while, as for single spectra analysis, we used one response matrix for each *XMM – Newton* pointing.

The sample used in the stacking analysis covers a flux range from about 10^{-14} to 1.2×10^{-13} erg cm^{-2} s^{-1}; we divided it in 5 flux bins, in order to have a sufficient number of counts in each bin (see Table 9.1; on average, brighter sources have a greater number of counts, so in the higher flux bins we need a smaller number of sources).

The spectra within the same flux bin were added using the `mathpha` task of `ftools` to produce a single spectral file. The same was done for background files. The auxiliary and response files were combined using the `addarf` and `addrmf` tasks of `ftools`, respectively. The combined spectra were grouped to a minimum of 20 counts per bin and were analyzed using XSPEC.

We fitted the stacked spectra in the $0.3 - 10$ keV range using a single power law model with column density fixed to the galactic value. The fit results are reported in Table 9.1. The Γ values obtained for the whole sample are consistent

Flux bins	N. of sources	Γ
$-14.1 < \log F_X < -13.7$	25	$1.72^{+0.09}_{-0.09}$
$-13.7 < \log F_X < -13.6$	22	$1.81^{+0.09}_{-0.08}$
$-13.6 < \log F_X < -13.5$	15	$1.83^{+0.10}_{-0.09}$
$-13.5 < \log F_X < -13.3$	14	$1.76^{+0.08}_{-0.08}$
$-13.3 < \log F_X < -12.9$	7	$1.75^{+0.12}_{-0.12}$

Table 9.1: Mean spectral properties from the stacking analysis of the 3 σ hard sample. N_H is fixed to the galactic value.

Optically unobscured AGN			Optically obscured AGN		
Flux bins	N. of sources	Γ	Flux bins	N. of sources	Γ
$-14.1 < \log F_X < -13.6$	18	$1.98^{+0.10}_{-0.09}$	$-14.1 < \log F_X < -13.7$	14	$1.58^{+0.13}_{-0.12}$
$-13.6 < \log F_X < -13.5$	9	$2.05^{+0.11}_{-0.11}$	$-13.7 < \log F_X < -13.6$	15	$1.62^{+0.11}_{-0.10}$
$-13.5 < \log F_X < -13.3$	8	$1.90^{+0.13}_{-0.12}$	$-13.6 < \log F_X < -13.4$	10	$1.46^{+0.12}_{-0.12}$
$-13.3 < \log F_X < -12.9$	3	$2.13^{+0.21}_{-0.20}$	$-13.4 < \log F_X < -12.9$	6	$1.45^{+0.12}_{-0.13}$
			SFs		
			$-14.1 < \log F_X < -13.6$	7	$1.25^{+0.19}_{-0.18}$
			$-13.6 < \log F_X < -12.9$	6	$1.26^{+0.12}_{-0.11}$

Table 9.2: Mean spectral properties from the stacking analysis of optically unobscured, optically obscured AGN and of the subclass of SF objects. N_H is fixed to the galactic value.

within errors with $\Gamma = 1.7 - 1.8$ in all the flux bins.

We then considered the optically unobscured and obscured AGN separately. We divided them in 4 bins, using two slightly different binnings for the two subsamples dictated by the available statistics. The results are reported in Table 9.2 and the photon index as a function of flux is shown in Fig. 9.11. The difference between the optically unobscured and obscured AGN populations is evident: for the unobscured AGN the measured photon index is consistent with $\Gamma = 2$ over the whole flux range, while for the optically obscured it is consistent with $\Gamma = 1.5$. Therefore the average spectral slope of unobscured AGN is consistent with that of typical broad line AGN (Turner & Pounds 1989; Nandra & Pounds 1994), while that of optically obscured AGN is consistent with the spectral slope of the cosmic X-ray background ($\Gamma = 1.4$, Gendreau et al. 1995; Chen et al. 1997; Vecchi et al. 1999). This is also in agreement with the results of Georgakakis et al. (2006), who used sources with optical counterparts with red color ($g - r > 0.4$) from the combined *XMM - Newton* and Sloan Digital Sky Survey (York et al. 2000) data.

We also divided our sample in several flux bins in order to explore the

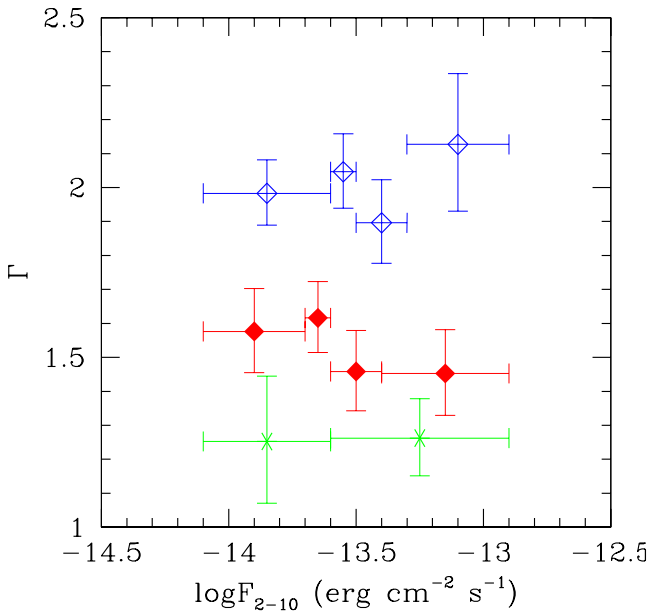

Figure 9.11: Photon index obtained from the fit of stacked spectra as a function of X-ray flux for the optically unobscured AGN (empty diamonds), optically obscured AGN (filled diamonds) and SFs (crosses). Vertical bars are errors on Γ, while horizontal bars show the flux bin width.

dependence of the spectral slope on the X-ray flux. No dependence is found for optically unobscured AGN, while there is some evidence of Γ decreasing with increasing X-ray flux for optically obscured AGN, but a larger and deeper sample is needed to confirm this trend.

According to Worsley et al. (2005), whilst the XRB is $\sim 85\%$ and $\sim 80\%$ resolved in the $0.5-2$ and $2-10$ keV bands respectively, it is only $\sim 60\%$ resolved above ~ 6 keV and $\sim 50\%$ resolved above ~ 8 keV. The missing population should be made of faint, heavily obscured AGN located at redshift of $\sim 0.5-1.5$, and with intrinsic absorption of $\sim 10^{23}-10^{24}$ cm^{-2}.

There are several examples of AGN in the literature whose optical spectra or broad band SEDs resemble those of normal galaxies. X-ray studies revealed a population of XBONGs (see Comastri et al. 2002 and Section 1.2). Similar sources were discovered in IR studies: spectroscopic follow up observations of AGN selected on the basis of their IR colors and radio fluxes revealed sources with blank optical spectra (Martìnez-Sansigre et al. 2006). Sub-mm observations of X-ray detected sources also found these type of objects (Borys et al. 2005; Alexander et al. 2005b,c). These sub-mm galaxies are IR luminous star-

burst galaxies with evidence of heavily absorbed and moderately luminous AGN activity. Their optical and near-IR output is dominated by the host galaxy emission (Borys et al. 2005). Although the taxonomy of these elusive AGN varies according to the wavelength at which they were discovered, similar scenarios are proposed to explain their nature. They are either explained by heavy absorption associated with dust with a large covering factor, or by an inefficiently accreting black hole. All of them can be good candidates to be responsible for the XRB at high energies. The properties of these elusive AGN resemble those of the SF class. In fact, the sources classified as SF do not show any AGN signature in the optical and IR. We also note that the fraction of X-ray absorbed sources in the SF class ($\sim 70\%$, 18 out of 26) is higher than that of X-ray absorbed sources in the type 2 AGN class ($\sim 58\%$, 28 out of 48). We therefore used stacking analysis to study the spectral properties of the SF population in our sample.

There are 13 SFs detected in the pn at off-axis angle $< 11'$, so we grouped them in two flux bins. The spectral fit for the two SF stacked spectra gives $\Gamma \sim 1.25$, with no differences in the two flux bins (Table 9.2 and crosses in Fig. 9.11). Therefore the average spectra of the SFs are harder than those of optically obscured AGN (type 2 + SFs) and even harder than the XRB spectrum in the same band. If the population responsible for the high energy XRB has the same SED properties of the SF objects discussed in this work, they might go unidentified as AGN even in the IR, where they look like star forming galaxies. A more detailed study of the properties of the SF objects is in progress and will be presented in Polletta et al., in prep.

Chapter 10

Properties of the sample: optical obscuration vs X-ray absorption

As discussed in the previous Chapters, we used the X-ray luminosity and the X-ray to optical ratio to establish the presence of AGN in our sample. The photometric method described in Chapter 8 provides a reliable tool to distinguish between obscured and unobscured AGN, where the obscured/unobscured definition refers to the prominence of continuum emission from the active nucleus in the optical-UV band. In obscured objects the optical-UV emission from the AGN may be either dimmed by intervening dust or weaker than that of the host, possibly a starburst galaxy. In this sense, "red quasars" (Wilkes et al. 2002; Gregg et al. 2002; Glikman et al. 2004; Urrutia et al. 2005; Wilkes et al. 2005) would be classified here as obscured objects.

Most of the literature works classify AGN using optical spectroscopy. However, as pointed out by Szokoly et al. (2004), these criteria, based on the presence and width of the emission lines in the spectra, have limitations in classifying AGN (type 1 vs type 2) and even in recognizing, among faint optical objects, which ones are AGN. Using a purely X-ray classification, based on X-ray luminosity and hardness ratio, they show that in their sample the optical spectroscopic classification fails to identify as AGN 61% of the objects with HII region - type spectra and 48% of objects with only absorption lines in the spectra. In essence this means that AGN signatures in optical spectra may be absent in cases of heavy obscuration (e.g. Barger et al. 2001), weak ionizing continuum (Yuan & Narayan 2004), dilution by the host galaxy (Moran et al. 2002), or obscuration by extranuclear dust (Rigby et al. 2006).

Using the photometric method we can obtain a redshift and a classification also for sources fainter that the optical spectroscopic limit. Therefore, if a

wide multiwavelength coverage in the optical and IR and a suitable set of AGN and galaxy templates are available, the photometric classification can be more effective than the spectroscopic one. However the X-ray information remains essential to identify heavily obscured AGN, where the AGN features are hidden both in the optical and IR bands, as in the case of the SF objects.

On the other hand the X-ray spectra and/or hardness ratios allow us to estimate absorption in the X-ray band, independently of the SED classification. In unified models for AGN, obscuration and absorption are thought to be associated and to occur in a dusty torus surrounding the AGN (see Chapter 1).

In the following we compare optically obscured and X-ray absorbed AGN in the 3 σ hard sample, computing the fraction of optically obscured and X-ray absorbed AGN as a function of X-ray flux, redshift and X-ray luminosity (Section 10.1) and comparing our findings with the literature (Section 10.2). We also briefly review some hypothesis to explain opposite optical and X-ray properties observed in a significant fraction of objects (Section 10.3).

10.1 Optical obscuration and X-ray absorption

For the following analysis, we consider a sample of 122 objects, which include the 119 identified AGN and the three optically blank fields. The two sources with X-ray to optical ratios and luminosities typical of normal galaxies are instead excluded. The ambiguous identifications with objects of the same colors (see Chapter 7) are also excluded.

The total number of AGN classified as optically obscured is 72 (59% of the sample), that of AGN classified as optically unobscured is 50 (41%). The X-ray absorbed AGN are 62 (51%). However only 45 of them are associated with obscured AGN, while the remaining 17 are classified as unobscured on the basis of their SEDs. Therefore, 62.5% of the optically obscured and 34% of the optically unobscured AGN are X-ray absorbed.

The numbers of optically unobscured, optically obscured and X-ray absorbed AGN in different flux, redshift and luminosity bins are given in Table 10.1, where we also report separately the number of X-ray absorbed sources within the optically unobscured and obscured AGN respectively.

The fractions of obscured/absorbed AGN in our sample are shown in Fig. 10.1 as a function of observed flux, redshift and absorption corrected hard X-ray luminosity. The left panels refer to optically obscured and unobscured AGN, while the right panels refer to X-ray absorbed and unabsorbed AGN,

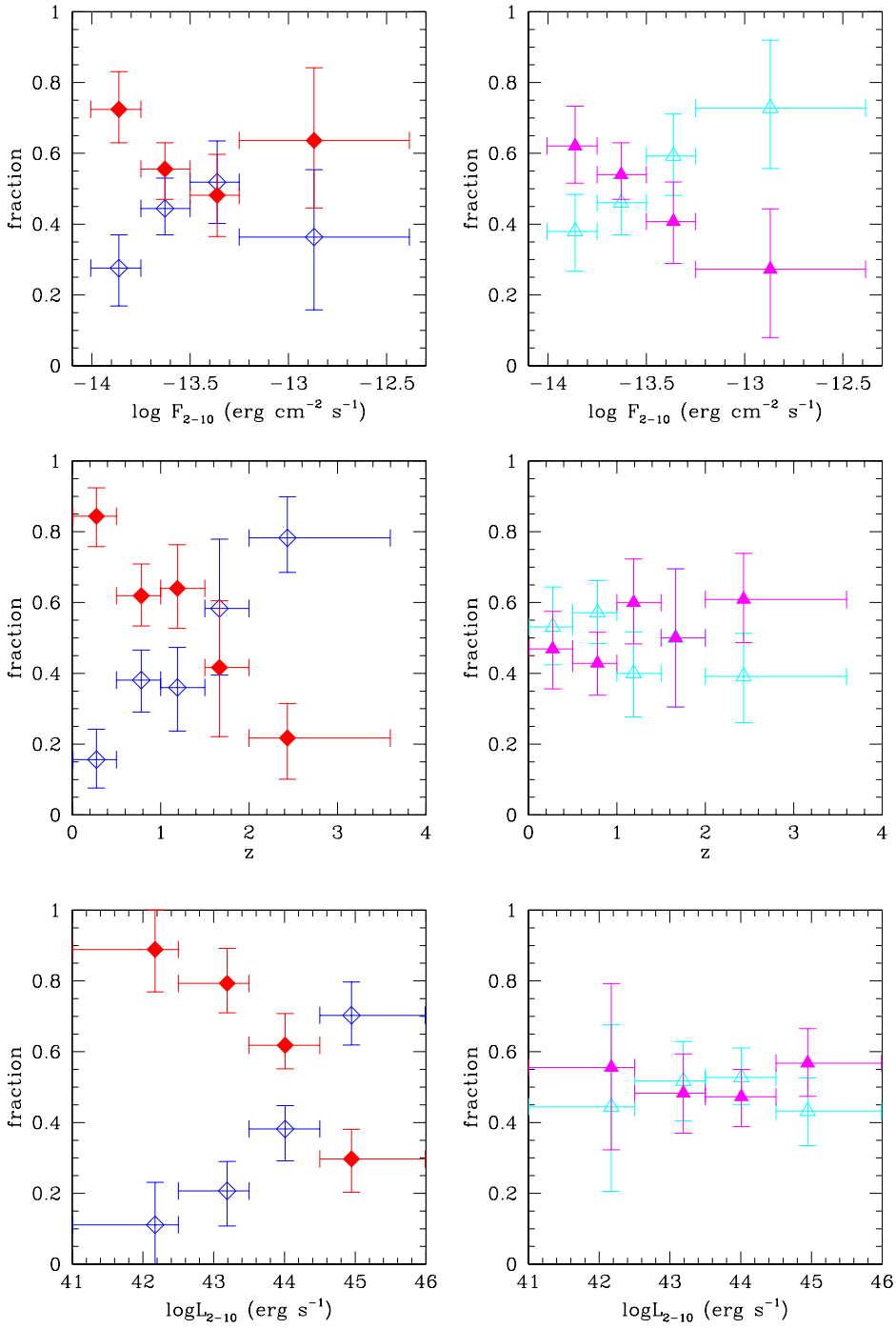

Figure 10.1: Left panels: fraction of optically obscured (filled diamonds) and unobscured (empty diamonds) AGN as a function of X-ray flux (upper panel), redshift (middle panel) and luminosity (lower panel). Right panels: fraction of X-ray absorbed ($N_H > 10^{22}$ cm^{-2} filled triangles) and unabsorbed (empty triangles) AGN as a function of X-ray flux (upper panel), redshift (middle panel) and luminosity (lower panel).

Bins				$N_H > 10^{22}$		
	N_{tot}	Opt. Unobsc.	Opt. Obsc.	N_{abs}	Opt. Unobsc.	Opt. Obsc.
$-14 < \log F < -13.75$	27	7	20	17	4	13
$-13.75 < \log F < -13.5$	61	27	34	33	10	23
$-13.5 < \log F < -13.25$	25	13	12	10	3	7
$-13.25 < \log F < -12.5$	9	3	6	2	–	2
$z < 0.5$	28	4	24	13	–	13
$0.5 < z < 1$	40	15	25	17	5	12
$1 < z < 1.5$	23	8	15	14	2	12
$1.5 < z < 2$	10	6	4	5	1	4
$z > 2$	21	17	4	13	9	4
$\log L < 42.5$	7	–	7	4	–	4
$42.5 < \log L < 43.5$	27	5	22	13	1	12
$43.5 < \log L < 44.5$	53	20	33	25	6	19
$\log L > 44.5$	35	25	10	20	10	10

Table 10.1: Total number of sources, number of optically unobscured and optically obscured AGN, number of X-ray absorbed AGN ($N_H > 10^{22}$ cm^{-2}), and number of optically unobscured and obscured AGN among X-ray absorbed AGN in each X-ray flux, redshift and X-ray luminosity bin (see text and Fig. 10.1).

irrespectively of their SED classification. We used the Bayesian statistics to estimate the "true value" of the fractions and their errors (68% credible interval, see Andreon et al. 2006, and references therein).

In order to establish the statistical significance of a trend, we tested whether existing data support a model in which the fraction 1) is constant or 2) has a linear dependence on redshift, flux or luminosity, by using the Bayesian Information Criterion (BIC, Schwartz 1978; an astronomical introduction to it can be found in Liddle 2004). A difference (ΔBIC) of 6 or more can be used to reject the model with a larger value of BIC, whereas a value between 2 and 6 is only suggestive (Jeffreys 1961). We also compared the trends of optically obscured and X-ray absorbed AGN using the same criterion.

Obscured sources are dominant in the lowest flux bin ($72^{+0.11}_{-0.09}$%, upper left panel), although a systematic trend of optically obscured AGN to increase with X-ray flux is not established (ΔBIC = 0.7). This result is evident also in the logN-logS curves computed for obscured and unobscured AGN, see Chapter 11. The fraction of X-ray absorbed AGN (upper right panel) is also higher at the faintest fluxes. There is a positive indication that the fraction of X-ray absorbed AGN changes systematically with flux (ΔBIC = 4.7). Comparing X-ray and

optical properties, we find a positive indication that the trends of optically obscured and X-ray absorbed AGN with flux differ (ΔBIC = 3.9).

The fraction of optically obscured AGN shows instead a steep decrease as a function of redshift (middle left panel), from $\sim 80\%$ at $z < 0.5$ to $\sim 20\%$ at $z > 2$, and the trend is highly significant (ΔBIC = 22.4). Similarly, the data strongly support a decrease of the fraction of optically obscured AGN with luminosity (lower left panel, ΔBIC = 21.6). The two trends are not independent, since in flux limited surveys a correlation between luminosity and redshift is expected. The incidence of X-ray absorbed sources appears instead to be constant both with redshift and luminosity (middle and lower right panels). Finally, there is very strong evidence that the trends of optically obscured and X-ray absorbed AGN are different both as a function of redshift (ΔBIC = 17.2) and luminosity (ΔBIC = 45.8).

In conclusion, while weakly significant trends are found with the X-ray flux, optically obscured and X-ray absorbed sources have very different dependences on redshift and luminosity.

10.2 Comparison with the literature

Several authors compute the fraction of X-ray absorbed or optically obscured AGN as a function of all or some of the quantities described above, however a detailed comparison between optical obscuration and X-ray absorption seems to be lacking in the literature.

The trends of broad line (type 1) AGN as a function of redshift and X-ray luminosity are explored e.g by Steffen et al. (2003), Barger et al. (2005), Treister & Urry (2005), Tozzi et al. (2006), who use data from the *Chandra* Deep Fields, in some cases complemented by shallower *Chandra* observations. All these samples reach flux levels significantly deeper than ours, thus probing the AGN population in more depth; since they cover smaller areas, their results at fluxes comparable to ours are based on smaller statistics. Given this, and assuming that unobscured AGN correspond to broad line AGN, the trends presented by the above authors are in qualitative agreement with those shown in the middle and lower left panels of Fig. 10.1.

We examined in more detail the data of the HELLAS2XMM 1df (Fiore et al. 2003; Perola et al. 2004) and of the Serendipitous Extragalactic X-ray Source Identification (SEXSI, Eckart et al. 2006), whose flux limits and areas are comparable to those of the XMDS. For the HELLAS2XMM, we computed

the fraction of optically obscured AGN using all the sources for which a spectroscopic classification is available (their samples S1, S2 and S4). Consistently with our classification scheme, we grouped together the objects spectroscopically classified as type 2 AGN, emission line galaxies (ELGs) and early type galaxies (ETGs), considering them as optically obscured AGN. We did the same for the SESXI data, considering as optically obscured AGN all sources spectroscopically classified as narrow line AGN (NLAGN), ELGs and absorption line galaxies (ALGs). Broad line AGN are instead classified as optically unobscured.

We computed the fractions of optically obscured AGN in the HELLAS2XMM and SEXSI using the Bayesian statistics, as done for our sample. We found that the fraction of optically obscured AGN decreases (and conversely the fraction of optically unobscured AGN increases) with redshift and luminosity. We notice that in the HELLAS2XMM survey the fraction of type 1 AGN is larger by a factor of ~ 2 than our fraction of unobscured AGN, for redshifts $z < 1.5$, while it is consistent with ours at higher redshifts. The agreement with the SEXSI survey is instead better. The spectroscopic completeness is however about 90% for the HELLAS2XMM, while it ranges from 40% to 70% for the SEXSI. We do not expect a perfect agreement of our fractions with the HELLAS2XMM and SEXSI ones, given the differences between photometric and spectroscopic classifications discussed in Section 8.2, however the trends observed are the same.

The X-ray properties (fraction of AGN with $N_H > 10^{22}$ cm^{-2}) are explored by a number of authors who use *XMM - Newton* or *Chandra* data of similar depth (flux limit of $\sim 10^{-14}$ erg cm^{-2} s^{-1}, see e.g. Piconcelli et al. 2003; Perola et al. 2004; Eckart et al. 2006; Akylas et al. 2006) and a quantitative comparison with their results is possible. Taking into account the different selection criteria and corrections that the different authors apply to the data, we find agreement within the errors with the results reported here.

Again, we concentrated in particular on the results obtained in the HELLAS2XMM and in the SEXSI surveys. Both Perola et al. (2004) and Eckart et al. (2006) show that the fraction of X-ray absorbed AGN increases with decreasing X-ray flux, even if the trends are significant only when X-ray fluxes as faint as 10^{-15} erg cm^{-2} s^{-1} are considered. In our flux range, we are consistent with the HELLAS2XMM and SEXSI values. Perola et al. (2004) and Eckart et al. (2006) also find that there is no evidence of a dependence of the fraction of X-ray absorbed AGN on luminosity. Again, these results are consistent with ours, with a better quantitative agreement with the SEXSI than with the

HELLAS2XMM survey (for example, the fraction of X-ray absorbed AGN is between ~ 0.4 and ~ 0.6 in our case and in the SEXSI, while it is between ~ 0.2 and ~ 0.4 in the HELLAS2XMM).

In conclusion, the analysis of our, the HELLAS2XMM and the SEXSI data indicates that the percentages of optically obscured and X-ray absorbed AGN within the same sample show different dependences on redshift and X-ray luminosity. Recent models which describe the cosmological evolution of the AGN space density, such as those of Ueda et al. (2003) and La Franca et al. (2005), predict that the fraction of X-ray absorbed AGN decreases with luminosity, and increase with redshift, in the case of the La Franca et al. (2005) model (see Section 1.5). The combination of a decrease in luminosity and an increase with redshift within a single flux limited sample, where the redshift and luminosity dependences tend to compensate each other, may well be the explanation underlying the observed "constancy" with redshift and luminosity of the absorbed AGN fraction in our data. In fact, La Franca et al. (2005) point out that the result of the opposite trends in L_X and z leads to an apparent constancy of the X-ray absorbed fraction of AGN. Only by combining several samples and thus covering wide strips of the $L_X - z$ plane with almost constant redshift or luminosity is it possible to disentangle the true dependences.

On the other hand, in a recent analysis of the *XMM – Newton* observation of the *Chandra* Deep Field South, Dwelly & Page (2006) do not find any dependence of the X-ray absorbed AGN fraction on redshift and luminosity and suggest that the trends observed in other samples e.g. by Ueda et al. (2003) and La Franca et al. (2005) could be the result of using deep X-ray data from *Chandra*, which could be biased against high redshift X-ray absorbed AGN. Therefore the redshift and luminosity dependence of X-ray absorption in the AGN population is still an open issue.

Anyway, the different redshift and luminosity dependences observed for optically obscured and X-ray absorbed AGN imply that in a significant number of objects obscuration and absorption are not strictly related. These objects and some hypothesis to explain different optical and X-ray properties are presented in the next Section.

10.3 Objects with discrepant absorption properties

As already mentioned in Chapter 1, there is a number of examples in the literature of objects that have opposite X-ray and optical properties, such as X-ray

absorbed type 1 AGN (e.g. Comastri et al. 2001; Brusa et al. 2003; Akiyama et al. 2003) or X-ray unabsorbed type 2 AGN (e.g. Panessa & Bassani 2002; Wolter et al. 2005), however it is not clear so far how common these exceptions are. Perola et al. (2004) find that about 10% of broad line AGN are X-ray absorbed, while Tozzi et al. (2006) estimate that the correspondence of unabsorbed (absorbed) X-ray sources to optical type 1 (type 2) AGN is accurate for at least 80% of the sources.

We find 17 X-ray absorbed, optically unobscured AGN, 34% of all unobscured AGN. They show well sampled SEDs, best-fitted with type 1 AGN templates. In 10 cases, the fit requires additional extinction, A_V=0.40–0.55, which corresponds to $N_H \sim 0.75 - 1 \times 10^{21}$ cm^{-2}, according to Eq. 1.1, but always lower than derived from the column density. The discrepancy between optical and X-ray properties can be explained e.g. by a dust-to-gas ratio lower than the Galactic value (Maiolino et al. 2001) or by a different path of the line of sights to the X-ray and the optical sources (e.g. see dual absorber model in Risaliti et al. 2000 or torus clumpy model, Hoenig et al. 2006). Another possibility is that in some objects the absorbing gas is ionized rather than neutral: in that case, dust would likely be evaporated and the intrinsic continuum plus broad emission lines would be observed in the optical spectrum of the AGN. Examples of broad line AGN whose X-ray spectra show absorption and are well fitted by a model with a ionized absorber are reported in Page et al. (2006).

Viceversa 27/72 (37.5%) optically obscured sources (AGN 2 + SF) do not show high X-ray absorption. We should note that some of them could be indeed type 1 AGN, reddened by external dust, e.g. associated to the host galaxy. As an example, an extinction value of A_V=1.35 would imply a column density of 2.88×10^{21} cm^{-2}, assuming a Galactic dust to gas ratio and the SMC extinction law (Prevot et al. 1984; Bouchet et al. 1985; Richards et al. 2003), and the source would not be classified among the X-ray absorbed ones. However, since in the fitting procedure we allowed a maximum extinction of $A_V = 0.55$, a type 1 AGN with higher extiction would be classified as type 2 AGN. This can be possible only for 7 of the 27 objects that we classify as optically obscured, X-ray unabsorbed AGN, while the other sources have SEDs which can not be fitted by a reddened type 1 AGN template. Therefore, if 37.5% is an upper limit to the fraction of optically obscured AGN without X-ray absorption in our sample, we estimate a lower limit of $\sim$ 30% (20 out of 65).

Another plausible explanation for (apparent) obscuration without X-ray absorption is a larger relative luminosity of the host galaxy compared to the AGN

optical light. In this scenario, the AGN optical light might simply be fainter than that of the host galaxy and not extincted. This effect could be important in our classification which is based on SED templates rather than spectroscopy. It would however be difficult to invoke this effect for the 14/27 unabsorbed but obscured objects in the luminosity range $\log L_X > 43.5$, because given the X-ray to optical ratio range typical of AGN, an AGN with such X-ray luminosities would have an optical luminosity $\log L_O > 42.5$ and would emerge from the host galaxy emission.

To summarize, our analysis shows that more than 30% of our sources have opposite optical and X-ray properties (17 X-ray absorbed, optically unobscured AGN and 27 X-ray unabsorbed, optically obscured AGN). Different hypothesis listed above can explain X-ray absorption in optically unobscured AGN or optical obscuration in X-ray unabsorbed AGN, however our data do not allow us to discriminate amongst the different scenarios. Larger samples obtained by combining sub-samples from surveys of various depths and areas, joined with optical spectroscopic data, are necessary to minimize selection effects and investigate the different possibilities.

Chapter 11

Properties of the sample: surface density

Using the logN-logS relationship computed in Chapter 6, we estimated the surface density of optically obscured and unobscured AGN (Section 11.1) and of a subsample of candidate type 2 QSOs (Section 11.2).

11.1 Optically obscured and unobscured AGN

In Chapter 6 we computed the logN-logS distribution for all the sources detected with a probability of false detection $p < 2 \times 10^{-5}$ in the $0.5 - 2$ and $2 - 10$ keV bands; for the $2 - 10$ keV band, this probability threshold is slightly lower than the 3 σ threshold chosen for the hard sample, therefore all the sources of the 3 σ hard sample were included in the logN-logS. We used the differential logN-logS for the $2 - 10$ keV band reported in Chapter 6, computed the fraction of optically unobscured and obscured AGN (see also Chapter 10) in each flux bin and rescaled the relationship accordingly. We made the reasonable assumption that the fraction of optically obscured and unobscured AGN in the area covered by the VVDS should be the same, within errors, as in the whole XMDS area.

The differential logN-logS relationships for optically obscured and unobscured AGN are shown in Fig. 11.1. The errors are the combination of the errors on the original logN-logS with those on the fractions, according to the error propagation formula. The two logN-logS are quite similar, except for the faintest fluxes ($F < 2 \times 10^{-14}$ erg cm^{-2} s^{-1}), where the density of the optically unobscured AGN is significantly lower (by a factor of ~ 2.5) than that of optically obscured AGN. Considering the cumulative logN-logS instead of the differential one, we can give an estimate of the surface density of optically

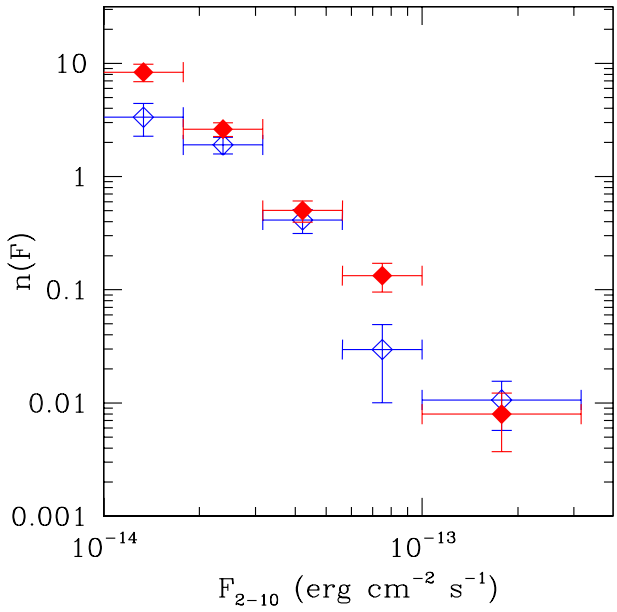

Figure 11.1: Differential logN-logS for unobscured (empty diamonds) and obscured AGN (filled diamonds). The units of $n(F)$ are number per 10^{-15} erg cm^{-2} s^{-1} deg^{-2}. Vertical bars show the error on the number of sources, while the horizontal bars show the flux bin width.

obscured and unobscured AGN. We find ~ 122 and ~ 75 sources deg^{-2}, respectively, at $F > 10^{-14}$ erg cm^{-2} s^{-1}, and the ratio between optically obscured and unobscured AGN is ~ 1.6 for the whole flux range covered. These values are lower by a factor of ~ 2 than those reported at $F_{2-10} > 10^{-14}$ erg cm^{-2} s^{-1} (converted by their $2-8$ keV band) by Bauer et al. (2004) in their study of the surface density of broad line and non broad line AGN in the *Chandra* Deep Fields, while the ratio between the "not type 1" and "type 1" AGN obtained by Bauer et al. (2004) is similar to ours (1.5). We have already noticed (see Section 6.3) that the cumulative logN-logS relationship obtained for the XMDS in the $2-10$ keV band is lower by a factor of ~ 2 than that estimated by Bauer et al. (2004), and that the difference observed can be justified by the large errors affecting the *Chandra* Deep Fields logN-logS at the highest fluxes and could be ascribed to cosmic variance. The agreement between our ratio of optically obscured/unobscured AGN and their ratio of not type 1/type 1 AGN is instead comforting, also in consideration of the differences between photometric and spectroscopic classifications (Section 8.2).

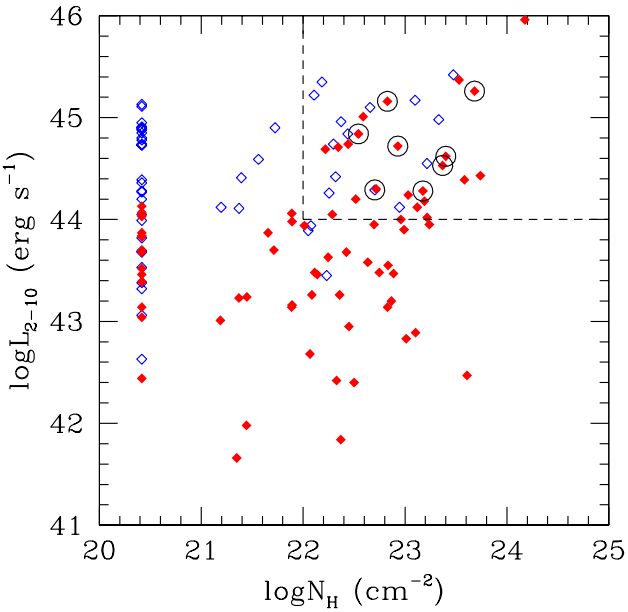

Figure 11.2: X-ray ($2-10$ keV) absorption corrected luminosity vs intrinsic column density. Empty diamonds are optically unobscured AGN and filled diamonds are optically obscured AGN. Encircled points are objects with $F_X/F_R > 40$ (see text). The dashed lines mark the region where type 2 QSOs should be found.

11.2 Type 2 QSO candidates

We searched for type 2 QSO candidates in the 3 σ hard sample. In the X-ray domain the type 2 QSO population is characterized by high intrinsic absorption ($N_H > 10^{22}$ cm^{-2}) and high X-ray luminosity ($L_X > 10^{44}$ erg s^{-1}). As already explained in Chapter 1, a large population of X-ray luminous, optically (and X-ray) obscured AGN is predicted both by AGN unification models and XRB population synthesis models. *Chandra* and *XMM – Newton* observations have shown that this population begins to emerge, and that medium deep X-ray surveys, covering relatively large sky areas at a relatively high flux limit, are more effective than deep surveys to select significant samples of type 2 QSO candidates among objects with high values of the X-ray to optical ratio ($F_X/F_R > 10$, see Fiore et al. 2003). Recent findings also suggest a connection between Extremely Red Objects (EROs, $R-K > 5$ in the Vega system) and type 2 QSOs (see e.g. Brusa et al. 2005; Severgnini et al. 2005, and references therein). Maiolino et al. (2006) suggest that by selecting extreme values of $F_X/F_R(> 40)$ and extreme values of $R-K(> 6)$, the type 2 QSO selection

efficiency may approach 100%.

The absorption corrected X-ray luminosity is shown as a function of the intrinsic column density in Fig. 11.2. There is a significant number of objects (35 out of 124) having $L_X > 10^{44}$ erg s^{-1} and $N_H > 10^{22}$ cm^{-2} in our sample. 14 of them (40%) are classified as unobscured AGN, while the remaining 21 are classified as obscured AGN, based on the SED classification. We verified that these objects generally have high X-ray to optical ratios, in particular 21 of the 25 X-ray sources in the 3 σ sample having $F_X/F_R > 10$ have $N_H > 10^{22}$ cm^{-2} and $L_X > 10^{44}$ erg s^{-1}. On the other hand, while for the optically unobscured AGN the fraction of high luminosity, X-ray absorbed sources having $F_X/F_R > 10$ is only 36% (5 out of 14), this fraction is 76% (16 out of 21) for the obscured ones.

All the 8 objects with $F_X/F_R > 40$ (the threshold used by Maiolino et al. 2006) satisfy the X-ray definition of a type 2 QSO (see encircled objects in Fig. 11.2). Seven of them are optically obscured, while only one is fitted by a reddened type 1 AGN template. These results confirm that type 2 QSO candidates are found between the high X-ray to optical ratio population and that the threshold proposed by Maiolino et al. (2006) is highly efficient in finding type 2 QSOs but it is far for exhaustive (i.e. many type 2 QSOs have $F_X/F_R < 40$).

In Fig. 11.3 the color between VVDS R band and SWIRE 4.5 μm band (in the AB system) is shown as a function of redshift for the type 2 QSO candidates. Objects fitted by a type 1 AGN template have generally blue colors. About 70% of the candidates fitted by a type 2 AGN or a SF template have extremely red infrared/optical flux ratios, as observed in extremely obscured AGN and similar to those observed in spectroscopically confirmed type 2 QSOs at high redshift ($z = 1.5 - 2.5$, see Severgnini et al. 2006; Polletta et al. 2006). We have K magnitudes from the UKIDSS Early Data Release or from the VVDS for 18 objects: 4 of them are EROs, they all have $F_X/F_R > 40$ and all are fitted by a type 2 AGN or a SF template. Given the blue optical/IR colors of the optically unobscured AGN, we exclude them from the type 2 QSO candidates. Therefore the sample of type 2 QSOs reduces to 21 objects. They represent (17 ± 3)% of the sources in the 3 σ hard sample and have X-ray fluxes in the range $1 - 5 \times 10^{-14}$ erg cm^{-2} s^{-1}.

As done in Section 11.1, we rescaled the surface density of X-ray sources at $F_{2-10} > 10^{-14}$ erg cm^{-2} s^{-1} ((197 ± 14) deg^{-2}) to the type 2 QSO fraction to estimate the type 2 QSOs surface density. We found (33 ± 6) deg^{-2}, lower than ~ 48 deg^{-2} found by Perola et al. (2004) in the HELLAS2XMM. We note

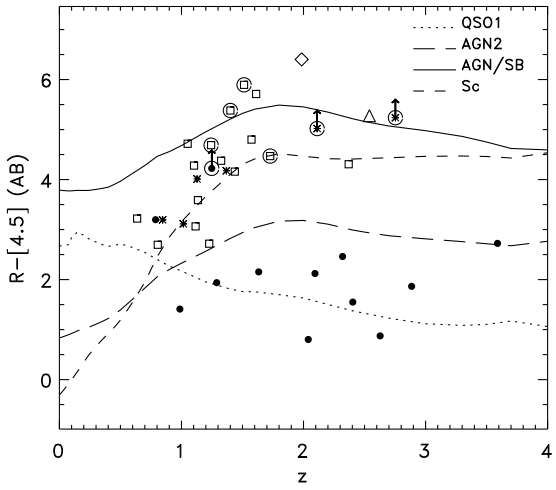

Figure 11.3: Optical-infrared color (in the AB system) as a function of redshift for the type 2 QSO candidates compared with the expected colors for various types of galaxy and AGN templates. Filled circles are sources fitted by a type 1 AGN template, squares are sources fitted by a type 2 AGN template, asterisks are object fitted by a SF template. Encircled points are objects having $F_X/F_R > 40$. Triangle is SWIRE_J104409.95+585224.8 in Polletta et al. (2006), diamond is XBS J0216-0435 in Severgnini et al. (2006).

however that Perola et al. (2004) do not give an error for their estimate.

The type 2 QSO population represents about 33% of all high luminosity sources ($L_X > 10^{44}$ erg s^{-1}) in our sample. For comparison, according to Perola et al. (2004), the fraction of X-ray absorbed sources ($N_H > 10^{22}$ cm^{-2}) in the high luminosity ($L_X > 10^{44}$ erg s^{-1}) AGN population would be between 28% and 40%.

Chapter 12

Conclusions

In this Thesis we presented the XMM Medium Deep Survey (XMDS), a project of teams in three *XMM – Newton* "hardware institutes" which dedicated part of their *XMM – Newton* guaranteed time to observe a contiguous region of sky, in order to study the cluster and AGN evolution. The XMDS consists of 19 X-ray pointings, of nominal exposure 20 ksec each, covering an area of about 2.6 $\deg^2$. X-ray observations are associated with several surveys in the radio (VLA observations at 1.4 GHz, Bondi et al. 2003, and at 325 and 74 MHz, Cohen et al. 2003), near-IR (the UKIRT Infrared Deep Sky Survey, UKIDSS, Dye et al. 2006; Lawrence et al. 2006), mid-IR (the *Spitzer* Wide Area InfraRed Extragalactic legacy survey, SWIRE, Lonsdale et al. 2003) and optical bands (the VIMOS VLT Deep Survey, VVDS, Le Fèvre et al. 2004, and the Canada France Hawaii Telescope Legacy Survey, CFHTLS). This multiwavelength coverage is essential to give a complete picture of the AGN population. The XMDS and associated projects are presented in Chapter 2.

X-ray data reduction was performed using an improved version of the pipeline developed by Baldi et al. (2002) for the HELLAS2XMM survey (see Chapter 4). 1322 X-ray sources with a probability that counts originate from a background fluctuation $p < 2 \times 10^{-4}$ in at least one of the five energy bands $0.3-0.5$, $0.5-2$, $2-4.5$, $4.5-10$ and $2-10$ keV were detected in 18 *XMM – Newton* fields (field G12 was not analyzed because of high background). Source detection was performed in each field independently, despite the fact that the fields of view of adjacent pointings overlap. The number of independent X-ray source is 1147. For each source, our pipeline gives X-ray position and net counts, probability of chance detection, signal to noise ratio, count rate and flux in each of the five energy bands defined above. Two hardness ratios are also provided.

We also developed a semiautomatic procedure to associate to each X-ray

source optical and IR counterparts (see Chapter 5). Our method was tested an a sample of relatively bright sources, detected with a signal to noise ratio larger than 4 in at least one of the five energy bands considered. The resulting catalogue (the 4 σ VVDS Catalogue) was published in Chiappetti et al. (2005). An improved version of this procedure was then applied to the whole XMDS. More than 80% of X-ray sources were unambiguously identified, and for more than 90% of them the angular separation between the position of the identified counterpart and the X-ray source is less than $4''$. Optical and IR identifications were also used to astrometrically correct the X-ray positions.

A first result, independent of optical identifications, is the number counts or logN-logS relationship. We computed the cumulative and differential logN-logS distributions in the $0.5 - 2$ and $2 - 10$ keV bands considering all sources with a probability of chance detection $p < 2 \times 10^{-5}$ in the soft and hard bands (Chapter 6). The resulting surface densities are 543 deg^{-2} at $F > 1.4 \times 10^{-15}$ erg cm^{-2} s^{-1} in the $0.5 - 2$ keV band and 289 deg^{-2} at $F > 7.9 \times 10^{-15}$ erg cm^{-2} s^{-1} in the $2 - 10$ keV band.

The shapes of the cumulative logN-logS are clearly curved in both bands and cannot be represented by a single power law. We computed a best fit using the differential logN-logS. The points in the soft band are best fitted by a double power law with slopes -2.6 for $F \gtrsim 10^{-14}$ erg cm^{-2} s^{-1} and -1.4 for $F \lesssim 10^{-14}$ erg cm^{-2} s^{-1}, while in the hard band the slope is -2.9 for $F \gtrsim 2 \times 10^{-14}$ erg cm^{-2} s^{-1}; at lower fluxes the slope is not well constrained.

A good agreement is found with the logN-logS distributions of various surveys, such as the HELLAS2XMM, the *Chandra* Large Synoptic X-ray Survey (CLASXS, Yang et al. 2004), the Serendipitous Extragalactic X-ray Source Identification program (SEXSI, Harrison et al. 2003) and the two *Chandra* Deep Fields combined (Bauer et al. 2004), even if the surface density obtained from the XMDS is slightly lower than those of the other surveys. On the other hand, in an independent analysis of the XMDS fields, Gandhi et al. (2006) find a perfect agreement with our logN-logS. Therefore, the differences observed can likely be ascribed to cosmic variance.

In order to study the properties of a significant number of X-ray absorbed AGN, we selected all sources detected with a S/N threshold ≥ 3 in the $2 - 10$ keV band. By selecting in the hard band, a significant number of absorbed X-ray sources should be detected. We considered only the area covered by the VVDS photometry, where data from the CFHTLS, UKIDSS and SWIRE surveys are also available. The 3 σ hard sample consists of 136 X-ray sources

detected over an area of about 1 deg^2. More than 90% of the sources in the 3 σ hard sample are identified with an optical and/or IR counterpart and 98% of them have X-ray to optical and X-ray to IR ratios consistent with those typical of AGN (Chapter 7).

We divided the identified sources in two subsamples, based on the observed $B-I$ color distribution: blue objects (43% of the sample) have $B-I<1.0$, while red objects (57%) have $B-I>1.0$. This rather arbitrary classification is justified by the fact that, in a $B-I$ vs I plot, the blue objects are consistent with the evolutionary track of a type 1 AGN, while red objects are consistent with the tracks of normal galaxies or type 2 AGN (Chapter 7). We assumed that in red objects the optical emission is due to the galactic starlight (but the X-ray emission is due to the AGN, since also red objects have X-ray to optical ratios typical of AGN), while blue objects require an important contribution from the AGN emission both in the optical and X-rays.

A more sophisticated analysis can be done taking advantage of the broad band photometry in the optical and IR: we constructed the SEDs of all the identified sources in the 3 σ hard sample and fitted them with a library of galaxy and AGN templates, in order to classify their optical to IR emission and determine photometric redshifts (Chapter 8). Comparing photometric with the spectroscopic redshifts available, we found consistency ($\Delta z<0.2$) in 84% of cases.

According to the template which gives the best fit solution, each source is classified in one of the following broad classes, type 1 AGN, type 2 AGN or star forming like-AGN (SFs). All sources fitted by a SF template which have X-ray to optical ratios typical of AGN (24 of 26) have high hard X-ray luminosities ($\gtrsim 10^{42}$ erg s^{-1}), suggesting that all are indeed AGN with the host galaxy emission dominating in the optical. The remaining two are classified as normal galaxies.

90% of blue objects ($B-I<1$) are fitted by a type 1 AGN template, while 94% of red objects ($B-I>1$) are fitted by a type 2 or a SF template. However, while at redshifts $z<1.6$ the SED and color classifications practically coincide (except for 2 type 2 AGN/SF objects with $B-I\sim 0.9$), at larger redshifts there is a degeneracy among the colors of different templates, so that the optical color alone is not indicative of a spectral type. Thus the simple classification based on the observed color appears in retrospect rather successful when compared with the more accurate, but model dependent, classification based on the whole SED, at least for redshifts $z<1.6$.

Comparison between the photometric and spectroscopic classification, when available, shows that all but one objects fitted by a type 1 AGN template have broad emission lines in the optical spectrum, but the broad lines are also present in the optical spectra of about 20% of objects with optical - IR obscuration in the SED (i.e. photometrically classified as type 2 AGN or SFs). These objects could be similar to the reddened type 1 quasars classified by Lacy et al. (2006), which generally have broad emission lines in the spectrum but a continuum significantly redder than that of a normal quasar. We adopt the photometric classification and AGN fitted by a type 1 template are referred as optically unobscured, while those fitted by a type 2 or a SF template are referred as optically obscured (Chapter 8).

The majority of sources in the 3 σ hard sample (57%) have a redshift less than 1, consistently with the redshift distribution of other X-ray selected samples (e.g. Barger et al. 2003; Hasinger 2003; Barger et al. 2005). However the redshift distribution of obscured and unobscured AGN are clearly different: the distribution of unobscured AGN is broad, with more than 60% of them at $z > 1$, while 70% of obscured AGN are concentrated at $z < 1$ (Chapter 8).

We studied the X-ray spectral properties of the 3 σ hard sample (Chapter 9), performing spectral fitting for individual sources with a sufficient number of counts, and a hardness ratio analysis for faint sources. According to the AGN unified model, optically obscured AGN should be X-ray absorbed ($N_H > 10^{22}$ cm^{-2}) and optically unobscured AGN should be X-ray unabsorbed, however the spectral analysis shows that the correspondence between optical ad X-ray classification is not complete: when the redshift dependence is taken into account, 60% of the optically obscured AGN are X-ray absorbed, but also 30% of the optically unobscured AGN have $N_H^{intr} > 10^{22}$ cm^{-2}.

We constructed stacked X-ray spectra to measure the spectral properties of the sample, averaged on the whole redshift range, and to find differences between optically obscured and unobscured AGN as a function of the X-ray flux. The stacked spectra of optically unobscured AGN have a photon index consistent with $\Gamma = 2$, similar to the average values found for unabsorbed AGN (Turner & Pounds 1989; Nandra & Pounds 1994), with no dependence on the X-ray flux. On the other hand, the slope of the stacked spectra of optically obscured AGN is consistent with $\Gamma = 1.5$, i.e. similar to the XRB spectrum ($\Gamma = 1.4$, Gendreau et al. 1995; Chen et al. 1997; Vecchi et al. 1999). This is consistent with the results obtained by Georgakakis et al. (2006), using a sample of X-ray sources with red ($g - i > 0.4$) optical counterparts. There is

some evidences of Γ decreasing with increasing X-ray flux for optically obscured AGN, but a larger and deeper sample is needed to confirm this trend.

The stacked spectrum of the objects fitted by a SF template is harder than the average spectrum of the optically obscured AGN class, with $\Gamma \sim 1.25$. According to Worsley et al. (2005), the XRB is only $\sim 60\%$ resolved above 6 keV and $\sim 50\%$ resolved above 8 keV. The missing population should be made of faint, heavily obscured AGN located at redshift of $\sim 0.5 - 1.5$ and with intrinsic absorption of $10^{23} - 10^{24}$ cm^{-2}. Since the sources classified as SF do not show any AGN signature in the optical and IR, 70% of them are X-ray absorbed and their stacked spectrum is harder than the XRB one, they are good candidates to be responsible for the XRB at high energies. If the missing population has the same SED properties as the SF objects discussed in this work, they might go unidentified as AGN even in the IR, where they look like star forming galaxies.

We compared the fractions of optically obscured and X-ray absorbed AGN as a function of X-ray flux, redshift and luminosity (Chapter 10). There is no significant trend of optically obscured AGN with X-ray flux, even if at low fluxes the AGN population is dominated by obscured sources ($\sim 72\%$). The fraction of X-ray absorbed AGN is also higher at the faintest fluxes and data suggest that it changes with flux, but the trend has not a high statistical significancy. On the other hand, the percentages of optically obscured and X-ray absorbed AGN show different dependences on redshift and luminosity: while the fraction of optically obscured AGN steeply decreases with redshift and luminosity, that of X-ray absorbed AGN is nearly constant at $\sim 50\%$ as a function of both redshift and luminosity. These trends are confirmed also by the analysis of literature data, such as Perola et al. (2004) and Eckart et al. (2006). The constancy of the population of X-ray absorbed AGN with redshift and luminosity observed in our sample is not in contradiction with the La Franca et al. (2005) predictions that the fraction of X-ray absorbed AGN should decrease with luminosity and increase with redshift, since these two dependences tend to compensate each other in a single, flux limited sample, like in our case.

The different trends of optically obscured and X-ray absorbed AGN as a function of redshift and luminosity imply that there is a significant number of objects which show opposite X-ray and optical properties. We find 17 X-ray absorbed, optically unobscured AGN (34% of all unobscured sources) and 27 X-ray unabsorbed, optically obscured AGN (37% of all obscured AGN). The X-ray absorption in objects fitted by a type 1 AGN template can be explained

by a gas to dust ratio lower than the galactic value, or by a different path of the line of sights to the X-ray and optical sources. Another possibility is that the absorbing material is ionized instead of neutral. Optically obscured, X-ray unabsorbed AGN can be explained by reddening of the AGN optical emission from external dust, or dilution of the AGN optical emission due to the host galaxy. However our data do not allow us to discriminate among the different scenarios.

We also computed the differential logN-logs relationship for the obscured and unobscured AGN, finding that the optically obscured AGN begin to dominate for $F < 2 \times 10^{-14}$ erg cm^{-2} s^{-1}, where the ratio between obscured and unobscured AGN is ~ 2.5 (Chapter 11). In the whole flux range considered, the surface density of the optically obscured AGN is higher than that of the unobscured ones by a factor of ~ 1.6. This ratio is similar to that found by Bauer et al. (2004) for non type1/type 1 AGN; we remind however the differences emerged between photometric and spectroscopic classifications.

The type 2 QSO candidates ($N_H > 10^{22}$ cm^{-2}, $L_X > 10^{44}$ erg s^{-1}) in the 3 σ hard sample are 21, fitted by a type 2 AGN or a SF template. They have on average IR/optical and X-ray to optical flux ratios typical of extremely obscured AGN. 4 of the 18 having a measured K magnitude are EROs. We estimated a surface density of type 2 QSOs at $F_{2-10} > 10^{-14}$ erg cm^{-2} s^{-1} of (33 ± 6) deg^{-2} (Chapter 11).

The 4 σ VVDS Catalogue and the logN-logS relationships for the whole XMDS were published in Paper I, while the work done in the 3 σ hard sample is presented in Tajer et al. submitted. A more detailed SED analysis of sources in the 3 σ hard sample and their dependence on luminosity and absorption is in progress and will be described in Polletta et al. in prep.

We plan to extend our analysis to the whole XMDS, nearly doubling the sample. Outside the VVDS area, optical CFHTLS and IR SWIRE data are available, therefore the SEDs can be constructed, even if with a smaller number of photometric points, and the template fitting procedure used for this sample can be applied also to the remaining XMDS sources. With a larger sample we could not only improve our statistics and confirm the trends presented in this Thesis, but also refine the photometric classification and explore in more detail the nature of objects in the SF class. We also plan to compile and make public the Catalogue of all XMDS sources, with optical and IR identifications.

Bibliography

Akiyama, M., Ohta, K., Yamada, T. et al. 1998, ApJ, 500, 173

Akiyama, M., Ohta, K., Yamada, T. et al. 2000, ApJ, 532, 700

Akiyama, M., Ueda, Y., Ohta, K., Takahashi, T. & Yamada, T. 2003, ApJS, 148, 275

Akylas, A., Georgantopoulos, I., Georgakakis, A., Kitsionas, S. & Hatziminaoglou, E. 2006, A&A accepted, astro-ph/0606438

Alexander, D. M., Brandt, W. N., Hornschemeier, A. E. et al. 2001, AJ, 122, 2156

Alexander, D. M., Aussel, H., Bauer, F. E. et al. 2002, ApJL, 568, L85

Alexander, D. M., Bauer, F. E., Brandt, W. N., et al. 2003, AJ, 126, 539

Alexander, D. M., Chartas, G., Bauer, F. E. et al. 2005a, MNRAS, 357, L16

Alexander, D. M., Bauer, F. E., Chapman, S. C. et al. 2005b, ApJ, 632, 736

Alexander, D. M., Smail, I., Bauer, F. E. et al. 2005c, Natur., 434, 738

Alonso-Herrero, A., Pérez-González, P. G., Rigby, J., et al. 2004, ApJS, 154, 155

Andreon, S., Quintana, H., Tajer, M., Galaz, G. & Surdej, J. 2006, MNRAS, 365, 915

Antonucci, R. 1993, ARA&A, 31, 473

Antonucci, R. R. J. & Miller, J. S. 1985, ApJ, 297, 621

Avni, Y. & Tananbaum, H. 1982, ApJL, 262, L17

Avni, Y. & Tananbaum, H. 1986, ApJ, 305, 83

Babbedge, T. S. R., Rowan-Robinson, M., Gonzalez-Solares, E.M. et al. 2004, MNRAS, 353, 654

Baldi, A., Molendi, S., Comastri, A., et al. 2002, ApJ, 564, 190

Balland, C., Devriendt, J. E. G. & Silk, J. 2003, MNRAS, 343, 107

Barger, A. J., Cowie, L. L., Mushotzky, R. F. & Richards, E. A. 2001, AJ, 121, 662

Barger, A. J., Cowie, L. L., Brandt, W. N. et al. 2002, AJ, 124, 1839

Barger, A. J., Cowie, L. L., Capak, P. et al. 2003, AJ, 126, 632

Barger, A. J., Cowie, L. L., Mushotzky, R. F. et al. 2005, AJ, 129, 578

Bauer, F. E., Alexander, D. M., Brandt, W. N. et al. 2002a, AJ, 123, 1163

Bauer, F. E., Alexander, D. M., Brandt, W. N. et al. 2002b, AJ, 124, 2351

Bauer, F. E., Alexander, D. M., Brandt, W. N., et al. 2004, AJ, 128, 2048

Bechtold, J., Siemiginowska, A., Shields, J. et al. 2003, ApJ, 588, 119

Berta, S. 2005, Ph.D. Thesis, University of Padua, Italy

Berta, S., Fritz, J., Franceschini, A., Bressan, A. & Pernechele, C. 2003, A&A, 403, 119

Bohlin, R. C., Savage, B. D. & Drake, J. F. 1978, ApJ, 224, 132

Bolzonella, M., Miralles, J.-M. & Pelló, R. 2000, A&A, 363, 476

Bondi, M., Ciliegi, P., Zamorani, G., et al. 2003, A&A, 403, 857

Borys, C., Smail, I., Chapman, S. C. et al. 2005, ApJ, 635, 853

Bouchet, P., Lequeux, J., Maurice, E., Prevot, L. & Prevot-Burnichon, M. L. 1985, A&A, 149, 330

Bower, R. G., Hasinger, G., Castander, F. J. et al. 1996, MNRAS, 281, 59

Boyle, B. J., Shanks, T., Croom, S. M. et al. 2000, MNRAS, 317, 1014

Brandt, W. N. & Hasinger, G. 2005, ARA&A, 43, 827

Brandt, W. N., Alexander, D. M., Hornschemeier, A. E., et al. 2001, AJ, 122, 2810

Brandt, W. N., Schneider, D. P., Fan, X. et al. 2002, ApJL, 569, L5

Brandt, W. N., Alexander, D. M., Bauer, F. E. & Vignali, C. 2004, astro-ph/0403646

Brodwin, M., Brown. M. J. I., Ashby, M. L. N. et al. 2006, ApJ, 651, 791

Brusa, M., Comastri, A., Mignoli, M., et al. 2003, A&A, 409, 65

Brusa, M., Comastri, A., Daddi, E. et al. 2005, A&A, 432, 69

Bruzual, G. & Charlot, S. 2003, 344, 1000

Cagnoni, I., Della Ceca, R. & Maccacaro, T. 1998, ApJ, 493, 54

Calzetti, D., Armus, L., Bohlin, R. C. et al. 2000, ApJ, 533, 682

Cash, W., 1979, ApJ, 228, 939

Chen, L.-W., Fabian, A. C. & Gendreau, K. C., 1997, MNRAS, 285, 449

Chiappetti, L., Tajer. M., Trinchieri, G., et al. 2005, A&A, 439, 413 (Paper I)

Chini, R., Kreysa, E. & Biermann, P. L. 1989, A&A, 219, 87

Cohen, A. S., Röttgering, H. J. A., Kassim, N. E., et al. 2003, ApJ, 591, 640

Coleman, G. D., Wu, C.-C. & Weedman, D. W. 1980, ApJS, 43, 393

Comastri, A., Setti, G., Zamorani, G. & Hasinger, G. 1995, A&A, 296, 1

Comastri, A., Fiore, F., Vignali, C. et al. 2001, MNRAS, 327, 781

Comastri, A., Mignoli, M., Ciliegi, P. et al. 2002, ApJ, 571, 771

Cowie, L. L., Garmire, G. P., Bautz, M. W., et al. 2002, ApJ, 566, L5

Cowie, L. L., Barger, A. J., Bautz, M. W. Brandt, W. N. & Garmire, G. P. 2003, ApJL, 584, L57

Crawford, D. F., Jauncey, D. L., & Murdoch, H. S. 1970, ApJ, 162, 405

Croom, S. M., Boyle, B. J., Loaring, N. S. et al. 2002, MNRAS, 335, 459

Czerny, B. & Elvis, M. 1987, ApJ, 321, 305

Della Ceca, R., Maccacaro, T., Rosati, P. & Braito, V., 2000, A&A, 355, 121

Devriendt, J. E. G., Guiderdoni, B. & Sadat, R. 1999, A&A, 350, 381

Dickey, J. M. & Lockman, F. J. 1990, ARA&A, 28, 215

Donley, J. L., Rieke, G. H., Rigby, J. R. & Pérez-González, P. G. 2005, ApJ, 634, 169

Downes, A. J. B., Peacock, J. A., Savage, A. & Carrie, D. R. 1986, MNRAS, 218, 31

Dwelly, T & Page, M. J. 2006, MNRAS accepted, astro-ph/0608479

Dye, S., Warren, S. J., Hambly, N. C., et al., 2006, MNRAS, 372, 1227

Eckart, M. E., Stern, D., Helfand, D. J. et al. 2006, ApJS, 165, 19

Elitzur, M., Nenkova, M. & Ivezić, Z. 2004, *ASP Conf. Ser. 320: The Neutral ISM in Starburst Galaxies*, ed. Aalto, S. Huttemeister, S., Pedlar, A., 242

Elvis, M. 1985, *Galactic and Extra-Galactic Compact X-ray Sources*, ed. Tabaka, Y., Lewin, W. H. G., 291

Elvis, M., Wilkes, B. J. McDowell, J. C. et al. 1994, ApJS, 95, 1

Fabian, A. C. & Iwasawa, K. 1999, MNRAS, 303, L34

Fioc, M. & Rocca-Volmerange, B. 1997, A&A, 326, 950

Fiore, F., Brusa, M., Cocchia, F., et al., 2003, A&A, 409, 79

Franceschini, A., Bassani, L., Cappi, M. et al. 2000, A&A, 353, 910

Franceschini, A., Manners, J., Polletta, M. d. C. et al. 2005, AJ 129, 2074

Galbiati, E., Caccianiga, A., Maccacaro, T. et al. 2005, A&A, 430, 927

Gandhi, P., Garcet, O., Disseau, L. et al. 2006, A&A, 457, 393

Gavignaud, I., Bongiorno, A., Paltani, S. et al., 2006, A&A, 457, 79

Gehrels, N. 1986, ApJ, 303, 336

Gendreau, K. C., Mushotzky, R., Fabian, A. C. et al, 1995, PASJ, 47, L5

Gendreau, K. C., Barcons, X. & Fabian, A. C. 1998, MNRAS, 297, 41

Georgantopoulos, I., Stewart, G. C., Blair, A. J. et al. 1997, MNRAS, 291, 203

Georgakakis, A. E., Georgantopoulos, I. & Akylas, A. 2006, MNRAS, 366, 171

George, I. M., Turner, T. J. & Netzer, H. 1995, ApJL, 438, L67

George, I. M., Turner, T. J., Yaqoob, T. et al. 2000, ApJ, 531, 52

Ghisellini, G., Haardt, F. & Matt, G. 1994, MNRAS, 267, 743

Ghizzardi, S., *In flight calibration of the PSF for the PN camera*, 2002, XMM-SOC-CAL-TN-0029

Giacconi, R., Gursky, H., Paolini, F. R. & Rossi, B. B. 1962, Phys. Rev. Lett., 9, 439

Giacconi, R., Bechtold, J., Branduardi, G. et al. 1979, ApJL, 234, L1

Giacconi, R., Zirm, A., Wang, J., et al. 2002, ApJS, 139, 369

Gilli, R., Risaliti, G. & Salvati, M. 1999, A&A, 347, 424

Gilli, R., Salvati, M. & Hasinger, G. 2001, A&A, 366, 407

Glikman, E., Gregg, M. D., Lacy, M. et al. 2004, ApJ, 607, 60

Green, P. J., Silverman, J. D., Cameron, R. A. et al. 2004, ApJS, 150, 43

Gregg, M. D., Lacy, M., White, R. L. et al. 2002, ApJ, 564, 133

Grogin, N. A., Conselice, C. J., Chatzichristou, E. et al. 2005, ApJL, 627, L97

Guainazzi, M., Matt, G., Brandt, W. N. et al. 2000, A&A, 356, 463

Haas, M. 2004, *Multiwavelength AGN Surveys*, ed. Mujica, R., Maiolino, R., 281

Haas, M., Chini, R., Meisenheimer, K. et al. 1998, ApJL, 503, L109

Haas, M., Klaas, U., Müller, S. A. H. et al. 2003, A&A, 402, 87

Halpern, J. P. 1984, ApJ, 281, 90

Harrison, F. A., Eckart, M. E., Mao, P. H., Helfand, D. J. & Stern, D. 2003, ApJ, 596, 944

Hasinger, G. 1992, in *The X-ray background*, ed. Barcons, X. & Fabian, A. C., 229

Hasinger, G. 2003, in AIP Conf. Proc. 666, *The Emergence of Cosmic Structure*, ed. S. S.Holt & C. S. Reynolds, 227

Hasinger, G. 2004, Nuclear Physics B Proceedings Supplements, 132, 86

Hasinger, G., Burg, R., Giacconi, R. et al. 1993, A&A, 275, 1

Hasinger, G., Burg, R., Giacconi, R. et al. 1998, A&A, 329, 482

Hasinger, G., Altieri, B., Arnaud, M., et al. 2001, A&A, 365, L45

Hatziminaoglou, E., Pérez-Fournon, I., Polletta, M. et al. 2005, AJ, 129, 1198

Hewett, P. C., Warren, S. J., Leggett, S. K. & Hodgkin, S. T., 2006, MNRAS, 367, 454S

Higdon, J. L., Higdon, S. J. U., Weedman, D. W. et al. 2005, ApJ, 626, 58

Ho, L. C., Filippenko, A. V. & Sargent, W. L. W. 1997a, ApJS, 112, 315

Ho, L. C., Filippenko, A. V., Sargent, W. L. W. & Peng, C. Y. 1997b, ApJS, 112, 391

Hoekstra, H., Mellier, Y., van Waerbeke, L. et al. 2006, ApJ, 647, 116

Hönig, S. F., Beckert, T., Ohnaka, K. & Weigelt, G. 2006, A&A, 452, 459

Hornschemeier, A. E., Brandt, W. N., Garmire, G. P., et al. 2001, ApJ, 554, 742

Hornschemeier, A. E., Bauer, F. E., Alexander, D. M. et al. 2003, AJ, 126, 575

Ilbert, O., Arnouts, S., McCracken, H. J. et al. 2006, A&A, 457, 841

Iovino, A., McCracken, H. J., Garilli, B., et al. 2005, A&A, 442, 423

Ishisaki, Y., Ueda, Y., Yamashita, A. et al. 2001, PASJ, 53, 445

Jarrett, T. H., Polletta, M., Fournon, I. P. et al. 2006, AJ, 131, 261

Jeffreys H. 1961, *Theory of Probability*, 3rd edn. Oxford Univ. Press, Oxford

Kauffmann, G. & Haehnelt, M. 2000, MNRAS, 311, 576

Kent, S. M., Dame, T. M. & Fazio, G. 1991, ApJ, 378, 131

Kirsch, M. G. F., Altieri, B., Chen, B., et al. 2004, SPIE Proc., 5488

Kirsh, M., *EPIC status of calibration and data analysis*, 2006, XMM-SOC-CAL-TN-0018

Kitsionas, S., Hatziminaoglou, E., Georgakakis, A. & Georgantopoulos, I. 2005, A&A, 434, 475

La Franca, F., Fiore, F., Comastri, A. et al. 2005, ApJ, 635, 864

Lacy, M., Storrie-Lombardi, L. J., Sajina, A., et al. 2004, ApJS, 154, 166

Lacy, M., Petric, A., Sajina, A. et al. 2006, AJ accepted, astro-ph/0609594

Laor, A., Fiore, F., Elvis, M., Wilkes, B. J. & McDowell, J. C. 1997, ApJ, 477, 93

Lawrence, A., Warren, S. J., Almaini, O. et al., 2006, MNRAS submitted, astro-ph/0604426

Le Fèvre, O., Mellier, Y., McCracken, H. J., et al. 2004, A&A, 417, 839

Le Fèvre, O., Vettolani, G., Garilli, B., et al. 2005, A&A, 439, 845

Lehmann, I., Hasinger, G., Schmidt, M., et al. 2001, A&A, 371, 833

Levenson, N. A., Weaver, K. A., Heckman, T. M., Awaki, H. & Terashima, Y. 2004, ApJ, 602, 135

Liddle, A. R. 2004, MNRAS, 351, L49

Lonsdale, C. J., Smith, H. E., Rowan-Robinson, M. et al. 2003, PASP, 115, 897

Lonsdale, C., Polletta, M. d. C., Surace, J. et al. 2004, ApJS, 154, 54

Madau, P. 1995, ApJ, 441, 18

Madau, P., Ghisellini, G. & Fabian, A. C. 1994, MNRAS, 270, L17

Mainieri, V., Rosati, P., Tozzi, P. et al. 2005, A&A, 437, 805

Maiolino, R. & Rieke, G. H. 1995, ApJ, 454, 95

Maiolino, R., Marconi, A., Salvati, M. et al. 2001, A&A, 365, 28

Maiolino, R., Mignoli, M., Pozzetti, L. et al. 2006, A&A, 445, 457

Malkan, M. A. & Sargent, W. L. W. 1982, ApJ, 254, 22

Marshall, F. E., Boldt, E. A., Holt, S. S. et al. 1980, ApJ, 235, 4

Martínez-Sansigre, A., Rawlings, S., Lacy, M. et al. 2006, MNRAS, 370, 1479

Mateos, S., Barcons, X., Carrera, F. J. et al. 2005a, A&A, 433, 855

Mateos, S., Barcons, X., Carrera, F. J. et al. 2005b, A&A, 444, 79

Mather, J. C., Cheng, E. S., Eplee, R. E. et al. 1990, ApJL, 354, L37

Mather, J. C., Cheng, E. S., Cottingham, D. A. et al. 1994, ApJ, 420, 439

Mathur, S., Wilkes, B. J. & Ghosh, H. 2002, ApJL, 570, L5

Matt, G. 2002, *Royal Society of London Philosophical Transactions Series A*, 360, 2045

Matt, G., Guainazzi, M., Frontera, F. et al. 1997, A&A, 325, L13

McCracken, H. J., Radovich, M., Bertin, E., et al. 2003, A&A, 410, 17

McHardy, I. M., Jones, L. R., Merrifield, M. R. et al. 1998, MNRAS, 295, 641

McLeod, K. K. & Rieke, G. H. 1995, ApJ, 441, 96

Mineo, T., Fiore, F., Laor, A. et al. 2000, A&A, 359, 471

Miyaji, T., Hasinger, G. & Schmidt, M. 2000, A&A, 353, 25

Moran, E. C., Filippenko, A. V. & Chornock, R. 2002, ApJL, 579, L71

Moretti, A., Campana, S., Lazzati, D. & Tagliaferri, G. 2003, ApJ, 588, 696

Murdoch, H. S., Crawford, D. F., & Jauncey, D. L. 1973, ApJ, 183, 1

Nandra, K. & Pounds, K. A., 1994, MNRAS, 268, 405

Nandra, K., George, I. M., Mushotzky, R. F., Turner, T. J. & Yaqoob, T. 1997, ApJ, 476, 70

Oke, J. B. 1974, ApJS, 27, 21

Pacaud, F., Pierre, M., Refregier, A. et al. 2006, MNRAS, 372, 578

Page, M. J., Loaring, N. S., Dwelly, T. et al. 2006, MNRAS, 369, 156

Panessa, F. & Bassani, L. 2002, A&A, 394, 435

Perola, G. C., Puccetti, S., Fiore, F. et al. 2004, A&A, 421, 491

Piccinotti, G., Mushotzky, R. F., Boldt, E. A., et al. 1982, ApJ, 253, 485

Piconcelli, E., Cappi, M., Bassani, L., Di Cocco, G. & Dadina, M. 2003, A&A, 412, 689

Pierre, M., Valtchanov, I., Altieri, B., et al. 2004, J. Cosmology Astropart. Phys., 9, 11

Pierre, M., Pacaud, F., Duc, P. A. et al. 2006, MNRAS, 372, 591

Polletta, M., Courvoisier, T. J.-L., Hooper, E. J. & Wilkes, B. J. 2000, A&A, 362, 75

Polletta, M., Wilkes, B., Siana, B., et al. 2006, ApJ, 642, 673

Polletta, M., Tajer, M., Maraschi, L. et al. 2007, in prep.

Pompilio, F., La Franca, F. & Matt, G. 2000, A&A, 353, 440

Prevot, M. L., Lequeux, J., Prevot, L., Maurice, E. & Rocca-Volmerange, B. 1984, A&A, 132, 389

Radovich, M., Arnaboldi, M., Ripepi, V., et al. 2004, A&A, 417, 51

Ranalli, P., Comastri, A. & Setti, G., 2003, A&A, 399, 39

Rees, M. J. 1984, ARA&A, 22, 471

Richards, G. T., Hall, P. B., Vanden Berk, D. E. et al. 2003, AJ, 126, 1131

Rigby, J. R., Rieke, G. H., Pérez-González, P. G. et al. 2005, ApJ, 627, 134

Rigby, J. R., Rieke, G. H., Donley, J. L., Alonso-Herrero, A. & Pérez-González, P. G. 2006, ApJ, 645, 115

Risaliti, G. 2002, A&A, 386, 379

Risaliti, G. & Elvis, M. 2004, *ASSL Vol. 308: Supermassive Black Holes in the Distant Universe*, 187

Risaliti, G., Maiolino, R. & Salvati, M. 1999, ApJ, 522, 157

Risaliti, G., Maiolino, R. & Bassani, L. 2000, A&A, 356, 33

Rosati, P., Borgani, S. & Norman, C. 2002, 40, 539

Rothschild, R. E., Baity, W. A., Gruber, D. E. et al. 1983, ApJ, 269, 423

Rowan-Robinson, M., Babbedge, T., Surace, J. et al. 2005, AJ, 129, 1183

Sanders, D. B. & Mirabel, I. F. 1996, ARA&A, 34, 749

Sanders, D. B., Phinney, E. S., Neugebauer, G., Soifer, B. T. & Matthews, K. 1989, ApJ, 347, 29

Schmidt, M. & Green, R. F. 1983, ApJ, 269, 352

Schmidt, M., Hasinger, G., Gunn, J. et al. 1998, A&A, 329, 495

Schultz, G. V. & Wiemer, W. 1975, A&A, 43, 133

Schwartz, G. 1978, Ann. Statistics, 5, 461

Semboloni, E., Mellier, Y., van Waerbeke, L. et al. 2005, A&A, 452, 51

Setti, G. & Woltjer, L. 1989, A&A, 224, L21

Severgnini, P., Caccianiga, A., Braito, V. et al. 2003, A&A, 406, 483

Severgnini, P., Della Ceca, R., Braito, V. et al 2005, A&A, 431, 87

Severgnini, P., Caccianiga, A., Braito, V. et al 2006, A&A, 451, 859

Shields, G. A. 1978, Natur., 272, 706

Silva, L., Granato, G. L., Bressan, A. & Danese, L. 1998, ApJ, 509, 103

Silverman, J. D., Green, P. J., Kim, D.-W. et al. 2002, ApJL, 569, L1

Silverman, J. D., Green, P. J., Barkhouse, W. A., et al. 2005, ApJ, 618, 123

Steffen, A. T., Barger, A. J., Cowie, L. L., Mushotzky, R. F. & Yang, Y. 2003, ApJL, 596, L23

Steffen, A. T., Barger, A. J., Capak, P. et al. 2004, AJ, 128, 1483

Surace, J. A., Shupe, D. L., Fang, F. et al., 2005, AAS, 207, 6301

Szokoly, G. P., Bergeron, J., Hasinger, G., et al. 2004, ApJS, 155, 271

Tajer, M., Polletta, M., Chiappetti, L. et al. 2007, A&A submitted

Tanaka, Y. & Bleeker, J. A. M. 1977, Space Science Reviews, 20, 815

Telfer, R. C., Zheng, W., Kriss, G. A. & Davidsen, A. F. 2002, ApJ, 565, 773

Tozzi, P., Gilli,, R. Mainieri, V. et al. 2006, A&A, 451, 457

Treister, E. & Urry, C. M. 2005, ApJ, 630, 115

Treister, E., Urry, C. M., Chatzichristou, E. et al. 2004, ApJ, 616, 123

Treister, E., Castander, F. J., Maccarone, T. J., et al. 2005, ApJ, 621, 104

Turner, T. J. & Pounds, K. A., 1989, MNRAS, 240, 833

Turner, T. J., George, I. M., Nandra, K. & Mushotzky, R. F. 1997, ApJS, 113, 23

Ueda, Y., Takahashi, T., Inoue, H. et al. 1998, Natur., 391, 866

Ueda, Y., Akiyama, M., Ohta, K. & Miyaji, T. 2003, ApJ, 598, 886

Urrutia, T., Lacy, M., Gregg, M. D. & Becker, R. H. 2005, ApJ, 627, 75

Vanden Berk, D. E., Richards, G. T., Bauer, A. et al. 2001, AJ, 122, 549

Vecchi, A., Molendi, S., Guainazzi, M., Fiore, F. & Parmar, A. N., 1999, A&A, 349, L73

Vignali, C., Brandt, W. N., Schneider, D. P., Garmire, G. P. & Kaspi, S. 2003a, AJ, 125, 418

Vignali, C., Brandt, W. N. & Schneider, D. P. et al. 2003b, AJ, 125, 433

Wang, Q. D. & McCray, R. 1993, ApJL, 409, L37

Waskett, T. J., Eales, S. A., Gear, W. K., et al. 2004, MNRAS, 350, 785

Weedman, D. W., Le Floc'h, E., Higdon, S. J. U., Higdon, J. L. & Houck, J. R. 2006, ApJ, 638, 613

Wilkes, B. 2004, *ASP Conf. Ser. 311: AGN Physics with the Sloan Digital Sky Survey*, 37, ed. Richards, G. T., Hall, P. B.

Wilkes, B. J., Schmidt, G. D., Cutri, R. M. et al. 2002, ApJL, 564, L65

Wilkes, B. J., Pounds, K. A., Schmidt, G. D. et al. 2005, ApJ, 634, 183

Wills, B. J., Netzer, H. & Wills, D. 1985, ApJ, 288, 94

Wilman, R. J. & Fabian, A. C. 1999, 309, 862

Wilms, J., Allen, A., & McCray, R., 2000, ApJ, 542, 914

Wolter, A., Gioia, I. M., Henry, J. P. & Mullis, C. R. 2005, A&A, 444, 165

Worsley, M. A., Fabian, A. C., Bauer, F. E., et al. 2005, MNRAS, 357, 1281

Wright, E. L., Mather, J. C., Fixsen, D. J. et al. 1994, ApJ, 420, 450

Yang, Y., Mushotzky, R. F., Steffen, A. T., Barger, A. J., & Cowie, L. L. 2004, AJ, 128, 1501

York, D. G., Adelman, J., Anderson, J. E. et al. 2000, AJ, 120, 1579

Yuan, F. & Narayan, R. 2004, ApJ, 612, 724

Zamorani, G., Henry, J. P., Maccacaro, T. et al. 1981, ApJ, 245, 357

Zamorani, G., Mignoli, M., Hasinger, G. et al. 1999, A&A, 346, 731

Zheng, W., Mikles, V. J., Mainieri, V. et al. 2004, ApJS, 155, 73

Appendix A

Properties of the 3 σ hard sample

We report in Table A.1 the X-ray, optical and infrared properties of the 3 σ hard sample. Column 1 list the XMDS identifier, column 2 the XMDS name, columns 3 and 4 the X-ray coordinates (astrometrically corrected), column 5 the $2-10$ keV flux, column 6 the hardness ratio between the $2-10$ and $0.5-2$ keV bands, column 7 the distance between the X-ray and the optical VVDS position, column 8 the VVDS B magnitude, column 9 the VVDS I magnitude, column 10 the color classification (B for blue, i.e. $B-I \leq 1$ and R for red, i.e. $B-I > 1$), column 11 the CFHTLS i' magnitude, column 12 the SWIRE 3.6 μm flux, column 13 the SWIRE 24 μm flux, column 14 the spectroscopic redshift, column 15 the photometric redshift, column 16 the photometric classification based on SEDs and column 17 the absorption corrected $2-10$ keV luminosity.

A "-1" means no data available (i.e. source outside the field of view or not measured flux because of instrumental problems). For sources undetected at 24 μm, a 5 σ upper limit (241 μJy) was used. For sources with ambiguous optical - IR identification, two or more rows are associated to the X-ray source, one for each candidate counterpart, with the one having the best probability (see Section 7.1) listed as first. In these cases, X-ray data are reported only in the first row. All magnitudes are in the AB system. The systematic error on SWIRE fluxes is 5%.

Table A.1: The 3 σ hard sample: XMDS identifier and name, X-ray coordinates, X-ray flux ($2-10$ keV), hardness ratio between the $2-10$ and $0.5-2$ keV bands, distance between the X-ray and optical VVDS positions, VVDS B and I magnitudes, color classification, CFHTLS i' magnitude, SWIRE 3.6 and 24 μm fluxes, spectroscopic and photometric redshifts and SED classification (see text). All magnitudes are in the AB system.

ID	XMDS Name	RA	Dec.	F_{2-10} (10^{-14} cgs)	HR	X − 0 ($''$)	mag. B	mag. I	color	mag. i'	$F_{3.6}$ (μJy)	F_{24} (μJy)	z_{sp}	z_{ph}	SED class.	$\log L^{corr}_{2-10}$ (erg s^{-1})
4	XMDS J022521.0−043949	02:25:21.079	−4:39:48.476	7.45	−0.07	0.8	21.08	18.39	R	18.56	259	410	0.265	0.245	SF	43.14
12	XMDS J022544.9−043735	02:25:44.988	−4:37:35.230	2.13	−0.23	1.0	24.66	22.14	R	21.96	32	< 241	3.5892	3.597	AGN1	45.42
13	XMDS J022504.5−043707	02:25:04.546	−4:37:07.416	2.30	−0.28	0.4	24.04	22.69	R	22.91	59	470	−1	1.103	AGN2	44.20
16	XMDS J022506.4−043621	02:25:06.484	−4:36:20.932	1.36	−0.65	0.6	22.37	20.77	R	20.87	109	362	−1	0.850	AGN2	43.68
18	XMDS J022510.6−043549	02:25:10.665	−4:35:49.283	2.97	−0.44	0.3	25.65	24.86	B	25.31	27	300	−1	1.612	AGN2	44.71
29	XMDS J022521.0−043228	02:25:21.067	−4:32:27.837	1.25	−0.25	1.3	24.51	21.59	R	21.93	52	< 241	−1	0.868	SF	43.68
36	XMDS J022449.8−043026	02:24:49.888	−4:30:26.192	3.54	−0.22	0.6	20.42	19.94	B	20.10	110	895	−1	0.987	AGN1	44.26
40	XMDS J022510.6−042928	02:25:10.689	−4:29:28.264	2.65	0.23	1.9	24.55	23.25	R	23.71	40	776	−1	1.051	AGN2	44.24
55	XMDS J022522.8−042648	02:25:22.870	−4:26:47.807	2.65	0.36	0.2	23.37	20.68	R	20.53	176	1065	1.029	1.135	AGN2	44.30
58	XMDS J022436.2−042511	02:24:36.239	−4:25:10.816	2.31	−0.27	0.4	25.35	23.31	R	23.06	33	357	−1	0.645	AGN2	43.63
60	XMDS J022439.6−042401	02:24:39.729	−4:24:01.115	4.71	−0.49	0.2	20.94	19.27	R	19.36	238	1477	0.478	0.302	AGN2	43.14
67	XMDS J022537.0−042132	02:25:37.108	−4:21:32.123	2.35	−0.69	0.8	19.39	19.11	B	19.42	170	1114	−1	0.961	AGN1	44.05
71	XMDS J022511.9−041911	02:25:11.970	−4:19:10.526	4.12	0.00	1.4	24.83	23.59	R	23.59	68	805	−1	1.401	AGN2	44.72
91	XMDS J022710.0−041649	02:27:10.185	−4:16:49.536	2.22	−0.45	0.9	23.35	21.76	R	22.24	57	705	−1	1.015	AGN2	44.08
						2.0	21.80	19.87	R	20.02	60	< 241	−1	0.396	SF	43.09
94	XMDS J022643.8−041626	02:26:43.962	−4:16:26.397	5.37	−0.15	0.3	20.96	18.34	R	18.52	405	1109	−1	0.386	SF	43.46
101	XMDS J022809.4−041524	02:28:09.546	−4:15:24.972	2.85	−0.53	0.9	24.60	21.74	R	−1	−1	−1	−1	0.874	SF	44.03
106	XMDS J022719.5−041407	02:27:19.650	−4:14:07.764	1.01	0.64	−1	−1	−1	−1	−1	53	1909	−1	0.387	AGN2	42.83
111	XMDS J022735.6−041317	02:27:35.721	−4:13:17.043	3.30	−0.03	0.4	25.43	24.46	B	−1	−1	−1	−1	2.360	SF	45.16
						0.8	25.27	24.47	B	−1	−1	−1	−1	2.514	SF	45.23
112	XMDS J022809.0−041232	02:28:09.129	−4:12:32.857	19.44	−0.52	1.8	19.83	19.04	B	−1	−1	0.878	−1	0.900	AGN1	44.90
114	XMDS J022649.7−041240	02:26:49.855	−4:12:40.512	2.03	−0.55	0.4	21.70	18.93	R	19.14	161	640	−1	0.392	SF	43.04
118	XMDS J022649.3−041154	02:26:49.466	−4:11:54.248	1.49	−0.69	1.2	22.93	21.73	R	21.85	78	361	1.1572	1.122	AGN2	44.05
120	XMDS J022735.7−041122	02:27:35.841	−4:11:22.637	9.05	−0.50	0.6	25.31	23.26	R	−1	−1	−1	−1	1.043	AGN2	44.72
						1.6	22.54	21.32	R	−1	−1	−1	−1	1.082	AGN2	44.76
124	XMDS J022659.7−041108	02:26:59.823	−4:11:08.500	2.46	0.46	0.2	22.28	20.32	R	20.45	100	912	−1	0.371	AGN2	43.14
133	XMDS J022713.1−040912	02:27:13.216	−4:09:12.800	2.28	−0.43	0.7	25.03	22.34	R	22.49	15	< 241	−1	0.414	AGN2	43.16
134	XMDS J022701.3−040912	02:27:01.488	−4:09:12.270	1.26	−0.54	0.4	21.39	20.18	R	20.24	117	566	−1	0.755	AGN2	43.52
138	XMDS J022656.0−040821	02:26:56.201	−4:08:21.483	1.15	0.35	4.6	22.47	20.30	R	20.45	119	523	−1	0.546	AGN2	43.20
139	XMDS J022727.7−040806	02:27:27.835	−4:08:06.268	2.29	−0.63	0.6	21.03	19.96	R	−1	−1	−1	−1	0.700	AGN2	43.70
140	XMDS J022701.3−040751	02:27:01.437	−4:07:51.221	5.05	−0.38	0.4	20.20	18.04	R	18.20	270	633	0.220	0.257	SF	43.01
142	XMDS J022644.1−040720	02:26:44.262	−4:07:20.192	2.53	−0.64	0.4	19.87	19.47	B	19.84	168	1412	−1	0.661	AGN1	43.68
143	XMDS J022655.4−040650	02:26:55.586	−4:06:50.880	1.71	0.04	0.7	22.35	20.54	R	20.87	87	1112	−1	0.374	AGN2	42.95
144	XMDS J022652.0−040556	02:26:52.138	−4:05:56.361	3.33	−0.49	0.1	20.62	20.61	B	20.37	100	388	−1	0.963	AGN1	44.20
149	XMDS J022707.2−040438	02:27:07.359	−4:04:38.575	1.96	−0.53	1.2	21.54	19.69	R	19.90	180	851	−1	0.477	AGN2	43.23
161	XMDS J022700.7−042020	02:27:00.832	−4:20:20.357	41.26	−0.76	0.6	17.71	16.34	R	16.42	1803	27141	0.053	0.086	AGN2	42.44
178	XMDS J022544.6−041936	02:25:44.673	−4:19:35.499	5.40	−0.43	1.7	19.64	17.49	R	17.79	285	< 241	−1	0.059	SF	41.66
179	XMDS J022607.7−041843	02:26:07.740	−4:18:42.879	12.07	−0.56	0.4	19.41	18.95	B	19.26	347	1577	0.495	0.183	AGN1	43.06
191	XMDS J022626.5−041214	02:26:26.535	−4:12:13.575	4.38	0.65	1.5	23.34	20.42	R	20.66	188	2267	−1	0.763	AGN2	44.18
						4.2	24.16	20.60	R	20.82	64	< 241	−1			
197	XMDS J022539.0−040823	02:25:39.020	−4:08:22.499	2.87	0.26	1.6	22.08	20.25	R	20.65	186	1035	−1	0.806	AGN2	44.00

Table A.1 continued

ID	XMDS Name	RA	Dec.	F_{2-10} (10^{-14} cgs)	HR	X − 0 ($''$)	mag. B	mag. I	color	mag. i'	$F_{3.6}$ (μJy)	F_{24} (μJy)	z_{sp}	z_{ph}	SED class.	$\log L^{corr}_{2-10}$ (erg s^{-1})
199	XMDS J022614.5−040738	02:26:14.540	−4:07:37.479	2.61	0.15	−1	−1	−1	−1	−1	26	< 241	−1	2.753	SF	45.26
227	XMDS J022511.4−041916	02:25:11.497	−4:19:17.389	3.51	0.00	2.8	27.41	24.82	R	24.62	22	< 241	−1	1.446	SF	44.69
						3.7	24.12	23.85	B	23.56	10	< 241	−1	1.683	AGN1	44.85
229	XMDS J022406.4−041830	02:24:06.475	−4:18:31.927	2.57	0.85	1.6	25.90	22.75	R	23.45	33	< 241	−1	1.128	SF	44.43
232	XMDS J022449.2−041800	02:24:49.235	−4:18:01.477	2.11	−0.65	0.4	21.72	20.39	R	20.52	66	365	−1	0.581	AGN2	43.46
233	XMDS J022456.0−041725	02:24:56.112	−4:17:26.698	1.80	−0.48	−1	−1	−1	−1	−1	20	< 241	−1	2.242	AGN1	44.84
242	XMDS J022437.8−041520	02:24:37.842	−4:15:21.854	1.56	−0.12	3.4	24.10	22.31	R	22.56	37	< 241	−1	1.015	SF	43.95
246	XMDS J022415.6−041416	02:24:15.678	−4:14:17.652	2.80	−0.48	1.7	21.53	20.65	B	21.14	59	533	−1	2.094	AGN1	44.96
253	XMDS J022451.9−041209	02:24:52.013	−4:12:10.157	1.85	−0.54	0.5	19.77	18.91	B	19.38	154	2366	−1	2.367	AGN1	44.91
255	XMDS J022408.4−041149	02:24:08.469	−4:11:50.595	1.66	0.24	2.1	24.61	23.91	B	23.96	45	< 241	−1	2.063	SF	44.77
						4.9	22.04	20.02	R	20.17	73	< 241	−1	0.340	SF	42.86
258	XMDS J022447.4−041049	02:24:47.510	−4:10:50.701	1.63	−0.14	0.2	21.41	21.16	B	21.17	20	< 241	−1	2.628	AGN1	44.98
270	XMDS J022449.2−040841	02:24:49.300	−4:08:42.809	1.25	−0.30	0.4	22.18	21.17	R	21.71	43	341	−1	0.703	AGN1	43.45
271	XMDS J022509.5−040836	02:25:09.623	−4:08:37.874	1.79	−0.57	1.3	20.38	19.87	B	19.79	95	786	−1	2.042	AGN1	44.74
272	XMDS J022501.6−040752	02:25:01.725	−4:07:53.534	2.57	−0.53	0.8	19.88	19.49	B	19.42	173	1099	−1	1.139	AGN1	44.27
279	XMDS J022421.3−040607	02:24:21.350	−4:06:08.861	2.24	−0.19	1.1	21.26	19.39	R	19.60	301	2330	−1	0.258	AGN2	42.68
280	XMDS J022417.9−040606	02:24:18.033	−4:06:07.171	1.86	0.08	0.7	23.84	23.01	B	−1	6	< 241	−1	1.633	AGN1	44.55
281	XMDS J022503.2−040538	02:25:03.251	−4:05:39.467	5.28	−0.58	0.7	21.22	20.62	B	20.88	92	669	−1	0.739	AGN1	44.12
282	XMDS J022452.1−040518	02:24:52.146	−4:05:20.053	4.53	−0.66	0.9	20.23	19.60	B	19.52	260	2366	−1	0.183	AGN1	42.63
288	XMDS J022421.2−040351	02:24:21.265	−4:03:52.487	2.26	−0.31	5.2	24.50	21.34	R	21.57	81	< 241	−1	0.566	SF	43.48
291	XMDS J022452.0−040258	02:24:52.111	−4:02:59.465	2.30	0.98	1.8	20.91	18.82	R	19.01	220	1052	−1	0.135	AGN2	42.47
330	XMDS J022333.0−041525	02:23:33.118	−4:15:25.133	1.24	0.50	1.4	25.72	23.50	R	23.39	56	369	−1	1.574	AGN2	44.39
351	XMDS J022356.5−041105	02:23:56.652	−4:11:05.848	1.66	−0.48	0.5	22.31	21.53	B	22.31	47	< 241	−1	1.031	AGN2	43.98
359	XMDS J022325.3−040922	02:23:25.479	−4:09:22.450	1.03	0.35	2.0	22.55	21.50	R	22.13	45	< 241	−1	1.154	SF	43.95
403	XMDS J022742.1−043607	02:27:42.144	−4:36:07.737	1.92	−0.19	−1	−1	−1	−1	29.88	13	< 241	−1	3.579	SF	45.37
406	XMDS J022732.7−043544	02:27:32.736	−4:35:44.652	4.03	0.22	1.5	22.74	21.90	B	22.02	66	895	−1	0.788	AGN1	44.12
414	XMDS J022726.3−043327	02:27:26.389	−4:33:27.610	1.62	−0.43	0.9	21.39	19.03	R	19.18	113	489	−1	0.146	SF	41.98
416	XMDS J022812.2−043230	02:28:12.290	−4:32:30.771	2.91	−0.50	3.2	21.17	20.48	B	−1	−1	− 1	−1	1.668	AGN1	44.73
420	XMDS J022729.2−043225	02:27:29.235	−4:32:25.984	1.91	−0.57	1.5	19.33	19.04	B	19.26	104	1427	2.2899	2.350	AGN1	44.89
427	XMDS J022758.6−043112	02:27:58.647	−4:31:12.027	1.33	−0.55	0.2	25.67	23.29	R	−1	−1	−1	−1	0.991	AGN2	43.84
430	XMDS J022737.1−043031	02:27:37.109	−4:30:31.532	2.04	−0.48	1.1	23.79	22.10	R	22.03	38	< 241	−1	0.734	AGN2	43.70
438	XMDS J022756.3−042905	02:27:56.391	−4:29:05.354	1.18	0.74	0.4	23.36	20.85	R	−1	−1	−1	−1	0.375	SF	42.89
439	XMDS J022746.0−042853	02:27:46.020	−4:28:53.194	1.06	0.10	1.4	23.79	23.19	B	23.28	54	< 241	1.3679	1.988	SF	44.12
440	XMDS J022748.8−042820	02:27:48.829	−4:28:20.933	3.12	−0.47	0.5	19.59	19.09	B	−1	−1	−1	−1	2.574	AGN1	45.22
449	XMDS J022815.2−042617	02:28:15.285	−4:26:17.032	1.68	−0.10	1.8	25.29	23.94	R	−1	−1	−1	−1	2.504	SF	44.95
						3.6	23.89	23.58	B	−1	−1	−1	−1	2.172	AGN2	44.80
453	XMDS J022802.3−042546	02:28:02.357	−4:25:46.815	2.06	0.32	1.6	23.27	20.71	R	−1	−1	−1	−1	0.568	AGN2	43.48
470	XMDS J022804.5−041818	02:28:04.571	−4:18:18.119	2.48	−0.51	0.1	26.05	25.00	R	−1	−1	−1	−1	1.886	AGN2	44.79
						1.3	25.53	24.53	R	−1	−1	−1	−1	0.418	SF	43.19
						3.6	24.38	22.95	R	−1	−1	−1	−1	1.082	AGN2	44.20
487	XMDS J022643.6−043317	02:26:43.649	−4:33:18.291	2.74	0.42	0.4	19.70	17.80	R	17.98	495	1401	0.308	0.489	SF	43.47
498	XMDS J022629.2−043057	02:26:29.282	−4:30:57.554	5.29	−0.47	0.7	20.10	19.75	B	19.59	75	941	2.031	1.903	AGN1	45.13
503	XMDS J022649.3−042920	02:26:49.366	−4:29:21.129	2.05	0.03	0.5	23.25	20.20	R	20.42	121	295	0.6335	0.737	AGN2	43.58
505	XMDS J022649.0−042745	02:26:49.004	−4:27:46.432	2.03	−0.53	0.3	20.04	18.92	R	19.11	203	1834	0.327	2.018	AGN1	44.78
521	XMDS J022658.8−042321	02:26:58.864	−4:23:21.563	5.19	−0.11	1.2	24.73	21.93	R	22.32	127	566	1.3253	1.305	AGN2	44.74
523	XMDS J022622.1−042221	02:26:22.126	−4:22:21.538	4.41	−0.63	0.6	19.28	18.50	B	18.77	155	1326	2.0060	1.678	AGN1	45.11
551	XMDS J022342.0−043533	02:23:42.086	−4:35:33.683	2.64	−0.40	1.2	21.41	20.70	B	20.84	82	721	−1	1.289	AGN1	44.42
561	XMDS J022424.1−043228	02:24:24.168	−4:32:28.884	2.81	−0.69	0.8	18.97	18.65	B	18.81	146	1087	−1	1.694	AGN1	44.73
564	XMDS J022350.7−043157	02:23:50.768	−4:31:57.899	2.17	−0.50	0.2	19.99	19.23	B	19.17	179	503	−1	1.230	AGN1	44.28

Table A.1 continued

ID	XMDS Name	RA	Dec.	F_{2-10} (10^{-14} cgs)	HR	X − 0 ($''$)	mag. B	mag. I	color	mag. i'	$F_{3.6}$ (μJy)	F_{24} (μJy)	z_{sp}	z_{ph}	SED class.	$\log L_{2-10}^{corr}$ (erg s^{-1})
565	XMDS J022356.8−043115	02:23:56.802	−4:31:15.137	1.92	−0.48	1.5	24.50	22.79	R	23.33	24	< 241	−1	1.051	SF	44.06
567	XMDS J022432.4−043036	02:24:32.468	−4:30:36.864	2.71	−0.62	0.1	20.80	19.91	B	20.49	66	433	−1	0.650	AGN1	43.69
571	XMDS J022330.2−043004	02:23:30.265	−4:30:04.246	2.76	−0.43	1.7	20.63	19.94	B	20.18	89	1402	2.666	2.404	AGN1	45.10
577	XMDS J022438.9−042705	02:24:38.940	−4:27:05.814	12.66	−0.67	0.9	18.87	17.40	R	17.54	637	6630	0.252	0.188	AGN2	43.39
578	XMDS J022350.7−042703	02:23:50.729	−4:27:03.790	1.34	−0.70	0.3	21.74	21.40	B	21.59	42	< 241	−1	1.139	AGN1	43.99
602	XMDS J022351.2−042054	02:23:51.280	−4:20:54.416	2.57	0.23	1.2	20.35	19.11	R	19.21	73	3752	0.181	0.097	SF	41.84
626	XMDS J022326.0−043534	02:23:25.969	−4:35:35.294	3.78	−0.45	1.0	25.00	22.33	R	22.30	64	409	−1	1.437	AGN2	44.69
708	XMDS J022605.3−045803	02:26:05.398	−4:58:03.890	2.30	−0.58	0.5	21.33	21.20	B	21.36	69	< 241	−1	1.332	AGN1	44.39
709	XMDS J022606.7−045722	02:26:06.723	−4:57:23.365	2.11	−0.67	0.3	20.93	20.14	B	20.32	109	626	−1	2.334	AGN1	44.95
710	XMDS J022627.4−045710	02:26:27.430	−4:57:11.053	5.40	−0.46	0.0	21.85	21.14	B	21.51	45	1559	−1	2.320	AGN1	45.35
718	XMDS J022615.1−045355	02:26:15.130	−4:53:55.676	2.14	−0.31	0.2	23.06	21.13	R	21.48	63	< 241	−1	0.896	SF	43.94
720	XMDS J022628.9−045252	02:26:28.949	−4:52:53.487	2.52	−0.58	2.5	21.86	19.82	R	20.99	−1	−1	−1	2.027	AGN1	44.88
731	XMDS J022554.1−044921	02:25:54.200	−4:49:21.907	1.25	−0.17	0.7	23.80	21.73	R	22.05	48	< 241	−1	0.581	AGN2	43.26
738	XMDS J022556.1−044724	02:25:56.111	−4:47:24.727	3.33	−0.56	0.2	20.92	20.16	B	20.75	107	589	1.010	0.898	AGN2	44.13
739	XMDS J022617.1−044724	02:26:17.199	−4:47:24.925	2.33	0.38	0.9	18.90	17.38	R	17.52	432	3233	0.140	0.184	SF	42.40
742	XMDS J022514.3−044659	02:25:14.304	−4:47:00.049	4.13	−0.57	1.0	18.63	18.17	B	18.12	243	2697	1.924	1.615	AGN1	44.85
743	XMDS J022625.2−044647	02:26:25.287	−4:46:47.949	2.28	−0.43	0.0	24.51	24.40	B	24.01	25	247	−1	2.370	AGN2	45.01
746	XMDS J022512.6−044633	02:25:12.644	−4:46:33.803	7.48	0.49	1.0	22.20	19.41	R	19.59	107	< 241	−1	0.344	SF	43.55
747	XMDS J022640.4−044606	02:26:40.488	−4:46:07.281	3.15	0.44	1.0	24.76	24.07	B	24.51	31	460	−1	1.243	AGN2	44.53
						2.0	25.24	24.08	R	24.53	−1	−1		1.221	AGN2	44.51
748	XMDS J022610.9−044550	02:26:10.984	−4:45:51.052	2.05	−0.33	0.7	23.13	22.15	B	22.75	20	< 241	−1	2.886	AGN1	45.17
755	XMDS J022600.1−044412	02:26:00.170	−4:44:13.349	2.80	−0.55	2.6	24.76	22.03	R	22.41	46	576	−1	0.730	AGN2	43.83
760	XMDS J022531.4−044210	02:25:31.431	−4:42:10.616	2.71	1.00	2.7	23.86	22.06	R	22.28	34	< 241	1.2274	0.833	AGN2	45.96
779	XMDS J022321.8−045740	02:23:22.045	−4:57:38.385	4.72	0.66	0.9	22.04	19.46	R	19.64	340	5583	−1	0.637	AGN2	44.02
780	XMDS J022332.0−045740	02:23:32.191	−4:57:38.712	2.45	−0.56	0.6	20.32	19.62	B	19.66	262	1250	−1	0.963	AGN2	44.07
782	XMDS J022326.3−045708	02:23:26.549	−4:57:05.982	2.91	−0.31	1.5	20.98	20.48	B	20.32	132	579	0.826	0.471	AGN1	43.38
787	XMDS J022317.9−045527	02:23:18.081	−4:55:25.250	1.42	0.18	0.5	24.22	22.65	R	23.23	14	< 241	−1	0.981	AGN2	43.90
788	XMDS J022353.7−045510	02:23:53.880	−4:55:08.174	4.86	−0.52	0.4	22.29	21.43	B	21.52	51	< 241	−1	1.003	AGN1	44.41
789	XMDS J022329.1−045452	02:23:29.341	−4:54:50.778	2.40	−0.64	1.2	20.44	19.92	B	20.01	140	< 241	0.604	0.479	AGN1	43.32
800	XMDS J022403.8−045120	02:24:04.068	−4:51:18.278	2.03	−0.58	0.2	22.70	20.95	R	21.07	130	874	−1	0.863	AGN2	43.87
801	XMDS J022344.4−045120	02:23:44.634	−4:51:18.223	1.74	−0.42	1.0	22.36	21.50	B	21.65	29	< 241	−1	0.930	AGN1	43.89
807	XMDS J022333.0−044924	02:23:33.185	−4:49:22.513	1.78	−0.49	0.9	20.66	20.26	B	20.22	37	290	2.302	2.039	AGN1	44.74
817	XMDS J022354.5−044815	02:23:54.772	−4:48:13.852	1.69	−0.66	1.2	18.25	18.01	B	18.15	251	3418	2.458	2.428	AGN1	44.90
820	XMDS J022319.4−044732	02:23:19.582	−4:47:30.407	3.87	−0.38	0.7	21.18	18.48	R	18.68	531	3756	0.293	0.666	AGN2	43.87
825	XMDS J022330.6−044633	02:23:30.803	−4:46:31.754	3.35	−0.50	0.7	24.57	23.37	R	−1	18	< 241	−1	1.727	AGN2	44.84
828	XMDS J022318.8−044616	02:23:19.040	−4:46:13.919	1.73	−0.51	0.1	21.23	20.76	B	21.15	45	356	−1	0.673	AGN1	43.53
840	XMDS J022330.9−044235	02:23:31.149	−4:42:33.036	2.07	−0.21	−1	−1	−1	−1	−1	9	< 241	−1	1.248	AGN1	44.29
842	XMDS J022402.4−044140	02:24:02.650	−4:41:38.339	3.63	0.16	3.8	14.87	13.54	R	−1	13528	40594	0.043	0.010	SF	41.24
844	XMDS J022343.2−044105	02:23:43.453	−4:41:03.352	1.95	0.75	2.8	26.04	24.47	R	24.18	26	363	−1	1.493	AGN2	44.57
						4.5	23.70	23.24	B	23.25	−1	−1	−1	1.970	AGN2	44.87
846	XMDS J022317.2−044035	02:23:17.415	−4:40:33.523	3.72	−0.38	1.1	18.81	18.23	B	18.74	580	4587	0.842	0.844	AGN1	44.11
1197	XMDS J022720.2−045738	02:27:20.271	−4:57:38.992	1.90	0.32	1.5	23.05	21.70	R	22.48	39	306	−1	1.116	AGN2	44.18
1199	XMDS J022651.6−045714	02:26:51.736	−4:57:14.797	6.39	−0.44	0.8	21.93	19.78	R	20.11	104	830	0.331	0.290	AGN2	43.24
1201	XMDS J022723.4−045608	02:27:23.526	−4:56:08.628	1.65	−0.43	1.5	22.18	21.34	B	21.48	54	313	−1	0.997	AGN1	43.94
1219	XMDS J022701.6−045158	02:27:01.690	−4:51:58.996	1.15	0.07	−1	−1	−1	−1	−1	23	< 241	−1	2.112	SF	44.62
1226	XMDS J022711.7−045038	02:27:11.761	−4:50:38.630	8.55	−0.51	1.1	21.17	20.42	B	21.10	97	734	−1	0.946	AGN1	44.59
1227	XMDS J022736.8−045033	02:27:36.895	−4:50:34.200	2.41	0.00	0.9	21.86	19.44	R	19.60	169	864	−1	0.445	AGN2	43.26
1231	XMDS J022731.9−044957	02:27:31.946	−4:49:57.627	0.98	−0.54	0.8	22.63	20.95	R	21.22	73	416	−1	0.739	AGN2	43.39
1236	XMDS J022729.0−044857	02:27:29.058	−4:48:57.908	1.18	0.09	2.5	27.35	24.03	R	24.71	30	621	−1	1.513	AGN2	44.28

Table A.1 continued

ID	XMDS Name	RA	Dec.	F_{2-10} (10^{-14} cgs)	HR	X − 0 ($''$)	mag. B	mag. I	color	mag. i'	$F_{3.6}$ (μJy)	F_{24} (μJy)	z_{sp}	z_{ph}	SED class.	$\log L^{corr}_{2-10}$ (erg s^{-1})
1246	XMDS J022712.8−044636	02:27:12.916	−4:46:37.102	2.34	−0.59	1.5	18.03	17.69	B	17.75	451	2830	3.550	1.286	AGN1	44.36
1247	XMDS J022633.1−044637	02:26:33.213	−4:46:38.477	3.17	−0.32	2.0	25.01	21.29	R	21.66	72	< 241	−1	0.846	SF	44.05
1248	XMDS J022725.4−044619	02:27:25.522	−4:46:19.686	4.62	−0.54	0.1	17.02	15.29	R	15.36	655	1974	−1	0.025	SF	40.82
1252	XMDS J022716.0−044539	02:27:16.045	−4:45:39.562	4.62	−0.60	1.6	20.42	20.02	B	20.12	143	1125	−1	0.590	AGN1	43.82
1264	XMDS J022751.3−044251	02:27:51.403	−4:42:51.783	3.19	−0.36	1.7	20.19	19.82	B	19.77	63	1035	−1	1.708	AGN1	44.80
1265	XMDS J022712.6−044221	02:27:12.698	−4:42:21.727	6.28	0.10	1.8	19.79	17.90	R	18.03	435	4214	0.205	0.120	AGN2	42.42

Appendix B

Results of spectral fits

We report here the spectral fit results from spectra of individual sources (see Section 9.1). In Table B.1 we list the column density, photon index, reduced χ^2 and number of degrees of fredom obtained from analysis of all sources for which we could leave free both Γ and N_H, together with the hardness ratio values. In Table B.2 we report spectral fit results obtained by fixing the photon index to $\Gamma = 2.0$ (columns 2 and 3) and $\Gamma = 1.7$ (columns 4 and 5), or inserting photometric (or spectroscopic, when available) redshift in the model (columns from 6 to 9). In column 10 we report the EPIC cameras used to extract the spectrum.

XMDS ID	$\log N_H$ (cm^{-2})	Γ	χ^2_ν (d.o.f.)	HR_{cb}	HR_{dc}
112	$20.44^{+0.51}_{-0.03}$	$1.65^{+0.32}_{-0.16}$	0.90 (19)	-0.60	-0.65
120	$21.08^{+0.18}_{-0.28}$	$1.98^{+0.22}_{-0.19}$	1.02 (32)	-0.61	-0.48
140	$20.41^{+0.39}_{-0.00}$	$1.60^{+0.20}_{-0.16}$	0.84 (10)	-0.72	-0.33
142	$20.41^{+0.50}_{-0.00}$	$2.28^{+0.42}_{-0.24}$	1.15 (10)	-0.74	-0.37
144	$20.98^{+0.30}_{-0.30}$	$2.63^{+0.56}_{-0.26}$	1.00 (12)	-0.60	-0.51
161	$20.41^{+0.12}_{-0.00}$	$2.77^{+0.08}_{-0.05}$	1.40 (74)	-0.81	-0.60
179	$20.41^{+0.40}_{-0.00}$	$2.34^{+0.35}_{-0.25}$	1.30 (11)	-0.65	-0.52
281	$20.97^{+0.29}_{-0.35}$	$2.37^{+0.25}_{-0.47}$	0.69 (12)	-0.72	-0.33
282	$20.41^{+0.35}_{-0.00}$	$2.45^{+0.25}_{-0.16}$	1.07 (19)	-0.72	-0.62
416	$20.41^{+0.48}_{-0.00}$	$2.03^{+0.36}_{-0.23}$	1.24 (13)	-0.60	-0.52
440	$20.68^{+0.45}_{-0.26}$	$2.02^{+0.50}_{-0.29}$	0.34 (10)	-0.58	-0.52
561	$20.42^{+0.57}_{-0.00}$	$2.46^{+0.51}_{-0.21}$	0.74 (13)	-0.76	-0.55
577	$20.41^{+0.38}_{-0.00}$	$2.35^{+0.19}_{-0.13}$	0.60 (25)	-0.74	-0.52
738	$20.41^{+0.58}_{-0.00}$	$2.36^{+0.28}_{-0.26}$	0.43 (8)	-0.69	-0.39
742	$20.41^{+0.38}_{-0.00}$	$2.13^{+0.38}_{-0.32}$	1.26 (7)	-0.66	-0.50
788	$20.41^{+0.44}_{-0.00}$	$1.81^{+0.27}_{-0.20}$	0.62 (11)	-0.56	-0.81
789	$20.42^{+0.54}_{-0.00}$	$2.32^{+0.49}_{-0.22}$	0.58 (11)	-0.74	-0.47
820	$20.41^{+0.61}_{-0.00}$	$1.48^{+0.51}_{-0.22}$	1.21 (8)	-0.52	-0.42
1199	$21.22^{+0.23}_{-0.30}$	$2.13^{+0.32}_{-0.32}$	1.06 (9)	-0.58	-0.32
1226	$20.54^{+0.36}_{-0.13}$	$1.83^{+0.21}_{-0.15}$	0.80 (22)	-0.62	-0.49
1248	$20.41^{+0.47}_{-0.00}$	$1.98^{+0.23}_{-0.15}$	1.01 (20)	-0.67	-0.33
1252	$20.41^{+0.21}_{-0.00}$	$2.20^{+0.20}_{-0.19}$	1.24 (15)	-0.66	-0.69

Table B.1: Spectral parameters obtained using simple power law model with both Γ and N_H free parameters for sources for which χ^2 statistics can be used. The quoted errors correspond to the 90 per cent confidence level for one interesting parameter. The formal 0.00 errors on $\log N_H$ are the result of having fixed a minimum column density (the galactic value).

Table B.2: Spectral parameters obtained using a simple power law model with $z = 0$ and $\Gamma = 2.0$ in columns 2 and 3, $\Gamma = 1.7$ in columns 4 and 5 and using photometric (or spectroscopic when available) redshift in colums 6, 7 and 8. In this case, the photon index is a free parameter when χ^2 statistics was used, otherwise it is fixed to 2.0. The quoted errors correspond to the 90 per cent confidence level for one interesting parameter. The formal 0.00 errors on $\log N_H$ are the result of having fixed a minimum column density (the galactic value).

XMDS ID	Results if $z = 0$				Results if $z = z_{ph}$				EPIC
	$\Gamma = 2.0$		$\Gamma = 1.7$						camera
	$\log N_H$ (cm^{-2})	χ^2_ν (d.o.f.)	$\log N_H$ (cm^{-2})	χ^2_ν (d.o.f.)	$\log N_H$ (cm^{-2})	Γ	χ^2_ν (d.o.f.)	z_{ph}	
4	$21.64^{+0.13}_{-0.14}$	–	$21.52^{+0.15}_{-0.17}$	–	$21.80^{+0.15}_{-0.17}$	2.0	–	0.245	pn
18	$21.26^{+0.15}_{-0.19}$	–	$21.07^{+0.20}_{-0.30}$	–	$22.12^{+0.19}_{-0.24}$	2.0	–	1.612	pn
36	$21.48^{+0.19}_{-0.22}$	–	$21.31^{+0.23}_{-0.32}$	–	$22.10^{+0.25}_{-0.29}$	2.0	–	0.987	M1 M2
40	$22.22^{+0.22}_{-0.23}$	–	$22.14^{+0.24}_{-0.25}$	–	$23.01^{+0.23}_{-0.24}$	2.0	–	1.051	pn
55	$21.86^{+0.27}_{-0.33}$	–	$21.73^{+0.29}_{-0.38}$	–	$22.66^{+0.28}_{-0.36}$	2.0	–	1.135	pn
60	$20.42^{+0.42}_{-0.01}$	–	$20.41^{+0.21}_{-0.00}$	–	$20.41^{+0.43}_{-0.00}$	2.0	–	0.302	pn
71	$21.94^{+0.19}_{-0.23}$	–	$21.81^{+0.22}_{-0.27}$	–	$22.91^{+0.19}_{-0.25}$	2.0	–	1.401	M1 M2
91	$20.41^{+0.23}_{-0.00}$	–	$20.41^{+0.16}_{-0.00}$	–					pn
94	$21.77^{+0.14}_{-0.15}$	–	$21.67^{+0.15}_{-0.17}$	–	$22.06^{+0.16}_{-0.17}$	2.0	–	0.386	pn
111	$21.50^{+0.22}_{-0.25}$	–	$21.35^{+0.25}_{-0.33}$	–					pn
112	$21.00^{+0.18}_{-0.24}$	1.01 (20)	$20.58^{+0.33}_{-0.17}$	0.86 (20)	$20.62^{+0.85}_{-0.21}$	$1.68^{+0.28}_{-0.19}$	0.89 (19)	0.900	M1
120	$21.09^{+0.11}_{-0.13}$	0.99 (33)	$20.75^{+0.18}_{-0.25}$	1.16 (33)					M1 M2
124			$20.90^{+0.77}_{-0.48}$	–	$20.73^{+0.99}_{-0.32}$	1.7	–	0.371	pn
133	$21.50^{+0.15}_{-0.17}$	–	$21.37^{+0.18}_{-0.23}$	–	$21.78^{+0.17}_{-0.20}$	2.0	–	0.414	pn
139	$20.42^{+0.31}_{-0.00}$	–	$20.41^{+0.15}_{-0.00}$	–	$20.41^{+0.46}_{-0.00}$	2.0	–	0.700	m1 M2
140	$20.93^{+0.22}_{-0.34}$	1.45 (11)	$20.48^{+0.39}_{-0.07}$	0.85 (11)	$20.41^{+0.38}_{-0.00}$	$1.60^{+0.21}_{-0.16}$	0.84 (10)	0.257	pn
142	$20.41^{+0.20}_{-0.00}$	1.38 (11)	$20.42^{+0.00}_{-0.00}$	2.75 (11)	$20.41^{+0.70}_{-0.00}$	$2.28^{+0.37}_{-0.24}$	1.15 (10)	0.661	pn
144	$20.42^{+0.27}_{-0.00}$	1.25 (13)	$20.41^{+0.00}_{-0.00}$	2.26 (13)	$21.40^{+0.37}_{-0.53}$	$2.60^{+0.48}_{-0.26}$	0.99 (12)	0.963	pn
149	$20.93^{+0.26}_{-0.47}$	–	$20.51^{+0.46}_{-0.10}$	–	$21.07^{+0.34}_{-0.66}$	2.0	–	0.477	pn
161	$20.42^{+0.00}_{-0.00}$	13.24 (75)	$20.41^{+0.00}_{-0.00}$	22.11 (75)	$20.41^{+0.00}_{-0.00}$	$2.77^{+0.07}_{-0.05}$	1.40 (74)	0.086	pn
179	$20.41^{+0.14}_{-0.00}$	1.63 (12)	$20.42^{+0.00}_{-0.00}$	2.96 (12)	$20.41^{+0.27}_{-0.00}$	$2.34^{+0.32}_{-0.25}$	1.30 (11)	0.183	pn
272	$20.41^{+0.13}_{-0.00}$	–	$20.41^{+0.09}_{-0.00}$	–	$20.41^{+0.20}_{-0.00}$	2.0	–	1.139	pn

Table B.2 continued

XMDS ID	Results if $z = 0$				Results if $z = z_{ph}$				EPIC
	$\Gamma = 2.0$		$\Gamma = 1.7$						camera
	$\log N_H$ (cm^{-2})	χ^2_ν (d.o.f.)	$\log N_H$ (cm^{-2})	χ^2_ν (d.o.f.)	$\log N_H$ (cm^{-2})	Γ	χ^2_ν (d.o.f.)	z_{ph}	
281	$20.57^{+0.28}_{-0.15}$	0.75 (13)	$20.41^{+0.18}_{-0.00}$	1.34 (13)	$21.26^{+0.35}_{-0.65}$	$2.32^{+0.38}_{-0.22}$	0.67 (12)	0.739	pn
282	$20.41^{+0.00}_{-0.00}$	2.18 (20)	$20.42^{+0.00}_{-0.00}$	4.71 (20)	$20.41^{+0.32}_{-0.00}$	$2.45^{+0.26}_{-0.16}$	1.07 (19)	0.183	pn
406	$22.29^{+0.21}_{-0.24}$	–	$22.20^{+0.22}_{-0.25}$	–	$22.93^{+0.21}_{-0.25}$	2.0	–	0.788	pn
416	$20.42^{+0.34}_{-0.00}$	1.16 (14)	$20.41^{+0.19}_{-0.00}$	1.55 (14)	$20.41^{+1.17}_{-0.00}$	$2.03^{+0.33}_{-0.23}$	1.24 (13)	1.668	pn
440	$20.65^{+0.31}_{-0.23}$	0.31 (11)	$20.42^{+0.25}_{-0.00}$	0.62 (11)	$21.50^{+0.73}_{-1.09}$	$2.00^{+0.36}_{-0.27}$	0.34 910)	2.574	pn
453	$22.24^{+0.39}_{-0.38}$	–	$22.10^{+0.41}_{-0.66}$	–					M2 pn
498	$20.42^{+0.44}_{-0.00}$	–	$20.41^{+0.23}_{-0.00}$	–	$20.41^{+1.24}_{-0.00}$	2.0	–	1.903	pn
521	$21.49^{+0.22}_{-0.30}$	–	$21.35^{+0.26}_{-0.46}$	–	$22.29^{+0.17}_{-0.40}$	2.0	–	1.325[a]	M1 M2
561	$20.41^{+0.12}_{-0.00}$	1.61 (14)	$20.41^{+0.00}_{-0.00}$	3.26 (14)	$20.43^{+1.32}_{-0.02}$	$2.48^{+0.48}_{-0.23}$	0.74 (13)	1.694	pn
564	$20.42^{+0.59}_{-0.01}$	–	$20.41^{+0.41}_{-0.00}$	–	$20.41^{+1.18}_{-0.00}$	2.0	–	1.230	M1 M2
577	$20.41^{+0.09}_{-0.00}$	1.31 (26)	$20.41^{+0.00}_{-0.00}$	3.08 (26)	$20.41^{+0.26}_{-0.00}$	$2.35^{+0.18}_{-0.13}$	0.60 (25)	0.188	M1 M2
710	$20.83^{+0.25}_{-0.41}$	–	$20.42^{+0.26}_{-0.00}$	–	$21.74^{+0.24}_{-1.33}$	2.0	–	2.320	pn
718	$21.29^{+0.27}_{-0.37}$	–	$21.09^{+0.34}_{-0.66}$	–	$21.81^{+0.34}_{-0.48}$	2.0	–	0.896	pn
738	$20.42^{+0.18}_{-0.00}$	0.97 (9)	$20.41^{+0.00}_{-0.00}$	2.40 (9)	$20.41^{+0.94}_{-0.00}$	$2.36^{+0.44}_{-0.26}$	0.43 (8)	0.898	pn
739	$22.31^{+0.37}_{-0.56}$	–	$21.94^{+0.64}_{-0.52}$	–	$22.10^{+0.67}_{-0.6}$	1.7	–	0.184	pn
742	$20.41^{+0.28}_{-0.00}$	1.16 (8)	$20.41^{+0.21}_{-0.00}$	1.75 (8)	$20.41^{+0.94}_{-0.00}$	$2.13^{+0.38}_{-0.32}$	1.26 (7)	1.615	pn
746	$22.50^{+0.14}_{-0.15}$	–	$22.41^{+0.15}_{-0.16}$	–	$22.83^{+0.14}_{-0.16}$	2.0	–	0.344	M1 M2
755	$20.41^{+0.26}_{-0.00}$	–	$20.41^{+0.15}_{-0.00}$	–	$20.41^{+0.41}_{-0.00}$	2.0	–	0.730	pn
779			$21.58^{+0.39}_{-0.30}$	–	$22.10^{+0.50}_{-0.46}$	1.7	–	0.637	pn
782	$20.42^{+0.50}_{-0.01}$	–	$20.42^{+0.32}_{-0.00}$	–	$20.41^{+0.62}_{-0.00}$	2.0	–	0.471	pn
788	$20.61^{+0.35}_{-0.20}$	0.71 (12)	$20.41^{+0.27}_{-0.00}$	0.63 (12)	$20.41^{+0.76}_{-0.00}$	$1.81^{+0.24}_{-0.20}$	0.62 (11)	1.003	pn
789	$20.41^{+0.16}_{-0.00}$	1.00 (12)	$20.42^{+0.00}_{-0.00}$	2.45 (12)	$20.41^{+0.71}_{-0.00}$	$2.33^{+0.41}_{-0.23}$	0.58 (11)	0.479	pn
820	$21.08^{+0.22}_{-0.32}$	1.41 (9)	$20.79^{+0.32}_{-0.37}$	1.14 (9)	$20.41^{+0.93}_{-0.00}$	$1.49^{+0.44}_{-0.22}$	1.21 (8)	0.666	pn
825	$21.41^{+0.12}_{-0.14}$	–	$21.22^{+0.16}_{-0.21}$	–	$22.36^{+0.15}_{-0.18}$	2.0	–	1.727	M1 M2
828	$20.42^{+0.41}_{-0.00}$	–	$20.41^{+0.26}_{-0.00}$	–	$20.41^{+0.64}_{-0.00}$	2.0	–	0.673	pn
846	$20.68^{+0.38}_{-0.26}$	–	$20.41^{+0.36}_{-0.00}$	–	$20.85^{+0.56}_{-0.44}$	2.0	–	0.844	pn
1199	$21.16^{+0.18}_{-0.25}$	2.02 (10)	$20.95^{+0.25}_{-0.40}$	1.35 (10)	$21.35^{+0.25}_{-0.40}$	$2.11^{+0.52}_{-0.34}$	1.07 (9)	0.290	pn
1226	$20.81^{+0.17}_{-0.25}$	0.86 (23)	$20.42^{+0.19}_{-0.00}$	0.83 (23)	$20.81^{+0.55}_{-0.040}$	$1.86^{+0.19}_{-0.20}$	0.78 (22)	0.946	pn
1227	$21.67^{+0.27}_{-0.26}$	–	$21.55^{+0.28}_{-0.31}$	–	$21.97^{+0.32}_{-0.31}$	2.0	–	0.445	pn

Table B.2 continued

XMDS ID	Results if $z = 0$				Results if $z = z_{ph}$				EPIC
	$\Gamma = 2.0$		$\Gamma = 1.7$						camera
	$\log N_H$ (cm^{-2})	χ^2_ν (d.o.f.)	$\log N_H$ (cm^{-2})	χ^2_ν (d.o.f.)	$\log N_H$ (cm^{-2})	Γ	χ^2_ν (d.o.f.)	z_{ph}	
1248	$20.42^{+0.38}_{-0.00}$	0.97 (21)	$20.42^{+0.16}_{-0.00}$	1.40 (21)	$20.41^{+0.32}_{-0.00}$	$1.98^{+0.23}_{-0.15}$	1.01 (20)	0.025	M1 M2
1252	$20.41^{+0.12}_{-0.00}$	1.34 (16)	$20.41^{+0.00}_{-0.00}$	2.39 (16)	$20.41^{+0.19}_{-0.00}$	$2.20^{+0.20}_{-0.19}$	1.24 (16)	0.590	pn
1264	$20.42^{+0.28}_{-0.00}$	–	$20.42^{+0.20}_{-0.00}$	–	$20.41^{+0.81}_{-0.00}$	2.0	–	1.708	pn
1265	$22.20^{+0.15}_{-0.16}$	–	$22.11^{+0.16}_{-0.18}$	–	$22.32^{+0.16}_{-0.17}$	2.0	–	0.120	pn

[a]: spectroscopic redshift

Acknowledgments

At the end of this long Thesis, I wish to thank all people that helped me in my work and in my life in the last years. Sorry in advance if I'm forgetting someone.

First of all, I would like to thank my supervisor, Dr. Ginevra Trinchieri, for her constant help in reducing data and in writing papers and Thesis. My deep thanks go also to Prof. Laura Maraschi, who gave a huge contribution to my work with her deep knowledge of the AGN world.

I also thank Lucio Chiappetti for his precious assistance in reducing *XMM – Newton* data and for answering all my naive questions about FORTRAN, IDL, databases and so on.

Lots of thanks to Mari Polletta, not only for her careful work in fitting SEDs, but also for her constant support and useful advices.

I would like to thank all people in the XMM-LSS, VVDS, CFHTLS and SWIRE collaborations for the work done, in particular Dario Maccagni for involving me in the XMDS project, and Micol Bolzonella for her suggestions in computing photometric redshifts and her comments to my paper.

My warm thank to all people at the Brera observatory for useful discussions, and in particular to:

– my room mates Olga and Lea, with whom I shared long and hot days of work;

– Elisabetta Memola, who supported me when I was feeling down – thank you also for the Cenacolo!

– Stefano Andreon, who taught me a lot of things about statistics and the "right" way to do research, and, above all, greatly helped me in these last, difficult months;

– Cristina Bernasconi, always ready to assist me with computer and software;

– Paola Severgnini, Paolo Saracco, Stefano Sandrelli, Filomena Cocchia and our geologist, Gianluca Lentini, for the sometimes serious, sometimes funny discussions held at lunchtime.

I also thank Valentina Braito and Lucia Ballo who always helped me when they were in Brera.

Again, many many many thanks to Boris and Fulvia. A lot of things have been changed since Fall 1995, when we began to talk about Asimov's stories, but they are still my dearest friends.

And finally, I have to thank my parents for their love and for always supporting me in all my choices, and Rocco, who within few months will be my husband. I know it's not easy living with me, so thank you for being here everyday!